DISCONTINUOUS YIELDING AND FRACTURE INITIATION NEAR A NOTCH IN MILD STEEL

Thesis by

Daniel Julius Krause

In Partial Fulfillment of the Requirements
For the Degree of
Doctor of Philosophy

California Institute of Technology
Pasadena, California
1968
(Submitted April 01, 1968)

ACKNOWLEDGMENTS

The author wishes to express his appreciation to Professor David S. Wood for his continuous interest and instruction during the changing course of the investigation, to Professor Donald S. Clark for his suggestions on experimental techniques and general encouragement, and to Professor Richard T. Shield for discussions of plastic stress analysis techniques.

Appreciation is expressed to the National Science Foundation, the Shell Companies Foundation, the Gillette-Paper Mate Corporation, and the R. C. Baker Foundation for fellowships granted during the investigation and to the National Defense Student Loan Program and Mr. Daniel E. Krause, the author's father, for loans which enabled the author to complete the investigation. Funds from the U. S. Army Research Office (Durham) supported the early phases of the experimental work.

The author wishes to thank Mr. Donald B. Forrest, Mr. Steven C. Crow, and Mr. Robert H. Hearn for their assistance with the experimental work. The author is also grateful to Dr. Kenneth R. King, Mrs. Phyllis P. Henderson, Mrs. Roberta I. Duffy, Mr. Jeffrey A. Gorman, Dr. William D. Harrison, Mr. Kenneth M. Jassby, Dr. Frank T. Snively, and Mr. Arthur P. L. Turner for their timely assistance in the preparation of this thesis.

ABSTRACT

This thesis presents the results of an experimental investigation of the initiation of brittle fracture and the nature of discontinuous yielding in small plastic enclaves in an annealed mild steel. Upper and lower yield stress data have been obtained from unnotched specimens and nominal fracture stress data have been obtained from specimens of two scale factors and two grain sizes over a range of nominal stress rates from 10^2 to 10^7 lb/in.^{2}sec at -111°F and -200°F. The size and shape of plastic enclaves near the notches were revealed by an etch technique.

A stress analysis utilizing slip-line field theory in the plastic region has been developed for the notched specimen geometry employed in this investigation. The yield stress of the material in the plastic enclaves near the notch root has been correlated with the lower yield stress measured on unnotched specimens through a consideration of the plastic boundary velocity under dynamic loading. A maximum tensile stress of about 122, 000 lb/in.^{2} at the instant of fracture initiation was calculated with the aid of the stress analysis for the large scale specimens of ASTM grain size 8 1/4.

The plastic strain state adjacent to a plastic-elastic interface has been shown to cause the maximum shear stress to have a larger value on the elastic than the plastic side of the interface. This characteristic of discontinuous yielding is instrumental in causing the plastic boundaries to be nearly parallel to the slip-line field where the plastic strain is of the order of the Lüder's strain.

TABLE OF CONTENTS

TABLE OF CONTENTS - Continued

TABLE OF CONTENTS - Continued

LIST OF TABLES

LIST OF FIGURES

LIST OF FIGURES - Continued

LIST OF FIGURES - Continued

LIST OF FIGURES - Continued

NOTATION

a	Radius to root of notch in notched specimens (axial symmetry) or distance from plane of symmetry to notch root (plane strain).
b	Radius to innermost tip of plastic enclave.
ρ	Root radius of hyperbola-shaped notch.
x, y, z	Cartesian coordinates employed for plane strain (y-z plane).
r, θ, z	Cylindrical coordinates employed for axial symmetry.
z	Direction of applied tensile load.
σ_{yd}	Yield stress or flow stress.
σ_{uY}	Upper yield stress measured on unnotched specimens.
σ_{LY}	Lower yield stress measured on unnotched specimens.
σ_{nom}	Average stress on minimum cross sectional area of specimen. Equal to tensile load divided by minimum cross sectional area.
σ_{max}	Calculated maximum value of the tensile stress in a notched specimen.
σ_{maxf}	Value of σ_{max} at the instant of fracture initiation.
$\dot{\sigma}$	Stress rate.

I. INTRODUCTION

1.1 The Problem

The brittle fracture behavior of mild steel is known to design engineers through the catastrophic failure of structures by fracture with little or no plastic deformation. The occurrence of brittle fractures in ships during and after World War II is well known. Landlocked steel structures, both welded and riveted, such as storage tanks, bridges and gas transmission lines, have been no less susceptible to catastrophic failure by fracture (1).*

To say that those structures which failed had not been designed and/or fabricated properly with respect to brittle fracture is a self-truth. To realize that an adequate set of design criteria to preclude brittle fracture is not known even at present (with the benefit of a lot of hindsight) is to appreciate the problem which brittle fracture poses.

In a simple tensile test an unnotched steel specimen may support an engineering stress more than one and a half times greater than its lower yield stress and neck down to 60 percent reduction in area prior to final fracture. This ductility of steel is an important property that is often exploited in engineering practice. Ductility is the property which enables a steel structure to plastically deform in regions of high shear stress where there are stress concentrations. Such deformation permits a more even distribution of the stress at a lower value so that the structure will support the load imposed on it. A structure that ultimately fails with a brittle fracture might have

---

*Numbers appearing in parentheses indicate references listed at the end of the thesis.

failed sooner, but for the redistribution of stresses through the ductile behavior of the material.

The problem of designing a steel structure to prevent failure by brittle fracture, then, is one of determining when total reliance for safe behavior (including safe failure) of a structure cannot be placed upon the ductility of the material. What are the relevant mechanics criteria and material properties which would enable an engineer to design against failure by brittle fracture? This question is not yet answered. However, much progress has been made in identifying environmental, design and material property factors that are conducive to brittle fracture.

Brittle fracture has been described above in terms of the behavior of structures. Certainly the engineer is interested in the extent of plastic deformation that may be anticipated before failure by fracture. But it must be understood explicitly that such behavior is determined partly by the material properties, partly by the mechanics of the region where brittle fracture is initiated and partly by the configuration of the remainder of the structure. The plastic strains associated with fracture initiation may or may not result in deformations large compared with the elastic deformations at the fracture load. The macro-behavior of the structure will not be of concern here. Attention will be focused upon the mechanics and the material behavior in the immediate vicinity of the initiation of brittle fracture in this investigation.

1.2 Factors Affecting Brittle Fracture Initiation

Low temperatures, high stress rates and triaxial tensile stress states are all known to be conducive to brittle fracture behavior in mild steel. The embrittling effect of these three factors is utilized in notch-bar impact tests that are commonly used as a guide to the brittleness of a steel.

The results of laboratory tests for brittle fracture are often reported in terms of a "transition temperature", above which a measured characteristic reflects ductile behavior and below which brittle behavior is observed. The characteristic may be energy absorption or fracture appearance. Low energy absorption corresponds to brittle fracture behavior. Crystalline cleavage facets on the fracture surface are associated with brittleness while fibrous tears are a result of ductile fracture.

Transition temperatures determined by different types of tests on the same steel will be different. Generally, though, a steel that exhibits a lower transition temperature in one test will also exhibit a lower transition temperature in another test. Thus these tests may be used to rank steels relative to each other in terms of brittleness (2, 3). An adequate understanding of brittle fracture for the design engineer will have been achieved when the details of brittle fracture are sufficiently well understood that all of the transition temperatures of the various types of tests can be predicted from the known behavior of the steel in just a few of the tests. An actual service condition could be viewed simply as a more complicated laboratory test (4).

A large specimen size is also conducive to brittle fracture. In many of the failures of large structures by brittle fracture there has been little evidence of high strain rates (1), a factor which is very important on a laboratory scale. The specimen scale size effect is observable in the small specimens normally tested in a laboratory (5, 6).

A small ferritic grain size is a metallurgical factor which inhibits brittle fracture. The effect of grain size must be isolated from the other metallurgical factors involved in brittle fracture in that, being a "size effect", it may interact with the specimen size effect.

Other metallurgical variables which may affect the brittle fracture behavior of a mild steel are the sub-grain size, heat treatment, carbide distribution (7), chemical composition and prior cold work. These latter effects will not be considered explicitly here. The view will be taken that the effects of these variables will be manifested in the results of appropriate mechanical tests wherein the temperature, stress rate, stress state, specimen geometry scale and grain size are known, and that no further knowledge of the metallurgical variables would be necessary for the design engineer.

An expanded discussion of the role of these five factors in brittle fracture must be preceded by an acquaintance with proposed fracture criteria. In the following section, fracture criteria which may be applicable to the present investigation will be discussed.

1.3 Brittle Fracture Initiation Criteria

A fracture criterion based upon the elastic strain energy release rate was proposed by Griffith (8) for brittle materials that contain microcracks. His criterion is that the amount of elastic strain energy made available as a crack increases in size must be at least as great as the increase in surface energy of the expanded crack. The Griffith criterion for fracture of a linearly elastic material may be expressed mathematically as

$$\sigma_c \approx \sqrt{E\alpha/d} \qquad [1.1]$$

where σ_c is the critical value of the nominally uniform tensile stress acting perpendicular to the crack to cause the crack to propagate, E is Young's modulus, α is the surface energy of the material, and d is the diameter of the crack. When the applied stress reaches the value of σ_c, the (pre-existing) crack is able to grow catastrophically to failure. This criterion has been shown by Orowan (9) to be a necessary and sufficient condition for fracture propagation in a completely brittle material.

The Griffith criterion strictly applies to a brittle material, one in which there is no plastic deformation prior to or during fracture propagation. Orowan (9) and Irwin (10) have modified the Griffith criterion to include the effect of a small amount of plastic deformation, such as accompanies a propagating crack to a depth of about ten mils below the free crack surfaces (11). In this case the criterion for fracture becomes $\sigma_c \propto \sqrt{E\rho/d}$, where ρ is the work per unit area required to produce the plastic deformation at the crack surface.

Two comments must be made concerning "ρ". First, this work of plastic deformation must be a direct consequence of the increasing size of the crack. Second, this plastic work will depend upon the yield strength of the material and, in steel, upon the rate of stress application and fracture propagation (9, 11). In the limiting case of low stress rates and high temperatures the plastic deformation may become so extensive that this criterion is not applicable. The Orowan-Irwin criterion is a necessary condition for brittle fracture propagation in the presence of limited plastic deformation, but it is not necessarily a sufficient one. It is necessary in that the only energy that can be expected to feed brittle fractures propagating at speeds of several thousand feet per second must be energy which is capable of release at similar or faster rates - comparable to the speed of sound in the metal, as has been noted by Pellini (12). It is not sufficient, or, rather, is inadequate as a criterion, because of the ambiguity of the value of "ρ" to be used in the equation.

Arising directly from the Orowan-Irwin fracture criterion is the maximum tensile stress criterion for fracture. The maximum tensile stress criterion predicts that brittle fracture will be initiated at that point in a steel specimen where the maximum tensile stress attains a critical value for that steel. One condition, that plastic deformation has been initiated in the region of the maximum tensile stress, is placed upon this criterion (13, 14, 15).

The maximum tensile stress and the Griffith criteria are shown to be equivalent for brittle materials when the maximum tensile stress is calculated at the atomic-scale tip of the crack itself (8, 9). The maximum tensile stress criterion and the Orowan-Irwin criterion, which must replace the Griffith criterion when restricted plastic deformation is present, are not equivalent. The non-equivalence of these two criteria results from the fact that the maximum tensile stress referred to in this criterion is calculated in the absence of a crack and would not directly reflect the atomic level stresses (forces on the bonds between atoms) at the tip of a crack if it were present. Extension of these criteria in plastically deformable materials to the physically significant level of atomic bond breakage is a matter for dislocation theory.

The similarity between the maximum tensile stress and the Orowan-Irwin criteria is illustrated further in the conjecture by Felbeck and Orowan (11) that the region of highest tensile stress may need to reach a certain critical size. The important difference between them is that the maximum tensile stress criterion is an expression of hope that a material would generate its own pre-Griffith (or Orowan-Irwin) micro-cracks if it were to plastically deform in a high tensile stress field.

The numerical value of the maximum tensile stress required for fracture initiation will depend upon the metallurgical structure of the steel - such as grain size, second phase distribution and disposition of interstitial atoms (16, 17).

Brittle fracture may be initiated in two modes: a nil-ductility mode and a ductile mode. In the nil-ductility mode, the local plastic strain preceding fracture has a value between the order of magnitude of elastic strains (12, 18) and the Lüder's strain (several percent) (15, 18). In the ductile mode fibrous tearing occurs for a distance of several grain diameters with subsequent conversion to brittle cleavage fracture propagation (11, 12, 18, 19).

Ductile initiation of fracture near a notch depends upon the occurrence of large plastic strains. These plastically strained regions may be so extensive as to cause general yielding of the specimen, with consequently high energy absorption, or they may be localized in thin plastic zones or "hinges" of the type observed by Green and Hundy (20). In the early stages of development, these thin plastic zones may extend far into the specimen along planes of maximum shear stress but still terminate in an elastic region. This situation is very favorable for conversion of an initial fibrous microcrack to brittle cleavage propagation.

A quasi-dislocation theory has been utilized to formulate a critical plastic "displacement" or strain criterion for the ductile mode of initiation of brittle fracture (15, 16). Stresses become involved only in that the necessary plastic strain state will be obtained through application of the appropriate stress magnitudes. Clausing (23) has reported that the value of the plastic strain is indeed of prime importance in the ductile mode of fracture initiation while both the stress level and the plastic strain state play important roles in the cleavage mode of initiation.

Thus brittle fracture criteria for steel are centered on three considerations: the elastic strain energy recoverable during (pre-existing) crack extension, the maximum tensile stress, and the magnitude of the plastic strain. There is at least an element of half-truth in each, which accounts for their partial success. But, no one of these fracture criteria as presently employed appears to be adequate for predicting the initiation of catastrophic brittle fracture, as will be seen in the following discussion of particular experimental results.

1.4 Results of Some Previous Fracture Investigations

The effects of the five factors of interest in this investigation - temperature, stress rate, triaxial stress state, specimen size, and grain size - upon brittle fracture criteria for steel may be observed in the results of many previous investigations. In most cases either the maximum or the nominal tensile stress within the material just prior to fracture is reported. Although there appears to be a general tendency to want to believe that a maximum tensile stress criterion for brittle fracture initiation can be correctly formulated (perhaps because of its relative simplicity), the data abound in illustrations of the variations of the calculated values of the maximum stresses at fracture with changes in the values of the five parameters listed above.

A variation of the numerical value of the maximum tensile stress criterion with grain size is expected since the grain size affects other material properties. A dependency upon the temperature and stress rate would not be surprising either since the upper and lower yield stresses of steel are a function of these two variables. But if the value of the maximum tensile stress at fracture were also a function of the other two parameters - triaxial tensile stress state and specimen size - it would not be useful as a fracture criterion.

Some of the apparent failures of the maximum tensile stress criterion may be associated with the integrity of the stress analyses employed in calculating the maximum stresses at fracture. This will be discussed later.

Another consideration is that several steps may be involved in gross fracture initiation, each of which may be dependent upon a different stress (and/or strain) criterion. Cottrell (16) and Petch (17) have suggested that the formation of microcracks of grain-diameter dimensions is a shear-stress-dependent dislocation process and that the subsequent Orowan-Irwin propagation of the microcrack through the grain boundary (which really constitutes initiation of brittle fracture of a structure) is tensile-stress dependent. Microcrack nucleation must precede propagation, according to this argument. Furthermore, the conditions for microcrack propagation may have to be present at the instant the initiating microcrack completes its original grain-size-related growth. Otherwise, additional plastic deformation in the adjacent grains may reduce the magnitude of the stress intensification associated with the microcrack. McMahon and Cohen (7) have observed that carbide cracking in steel precedes and nucleates the microcracks of grain-diameter dimensions.

The results of other investigations that will be discussed in this thesis utilized unnotched or notched specimens. Unnotched specimens have the advantage of being uniformly stressed at easily calculable values before necking occurs. They are rather insensitive to geometry-size effects, but are the first specimens in which a quantitative description of the effect of grain size upon brittle fracture initiation was attempted (14, 24). On the other hand, notched specimens, in which triaxial tensile stress states are induced, tend to exhibit geometry-size effects, but stress and strain analyses are difficult to perform after small amounts of plastic deformation have occurred.

Notched specimens - the information they provide and the problems of interpretation - are the focal point of the work reported in this thesis.

A. Temperature and Stress Rate - Eldin and Collins (25), Gensamer (26), Hahn, Averbach, Owen and Cohen (15), and Knott and Cottrell (19), among others, have observed the change in the fracture stress and the upper and lower yield stresses of unnotched steel specimens as the testing temperature is changed, for a fixed strain rate. Their data all show an increasing yield stress with decreasing temperature and a fracture stress well above the yield stress at higher temperatures, but decreasing rapidly in a narrow temperature range and becoming about equal to first the lower, then the upper yield stress at lower temperatures.

Selected data from Hahn, et al., whose data and interpretation are the most complete of the above examples, are shown in Fig. 1. The phenomena distinctive of the lettered temperature ranges in Fig. 1 are listed below the graph.

Several features of Fig. 1 are of interest in the present investigation. The first feature is the very large reduction in area sustained by those specimens tested in the high temperature range where the fracture stress is substantially higher than the yield stress. This implies that the material itself has changed prior to the time of fracture due to the large plastic strains. The use of notched specimens in which the plastically deformed region is localized in the region of the notch root may permit large tensile stresses to be developed in regions which have had little or no plastic deformation. This is an important reason for the use of notched specimens in the present

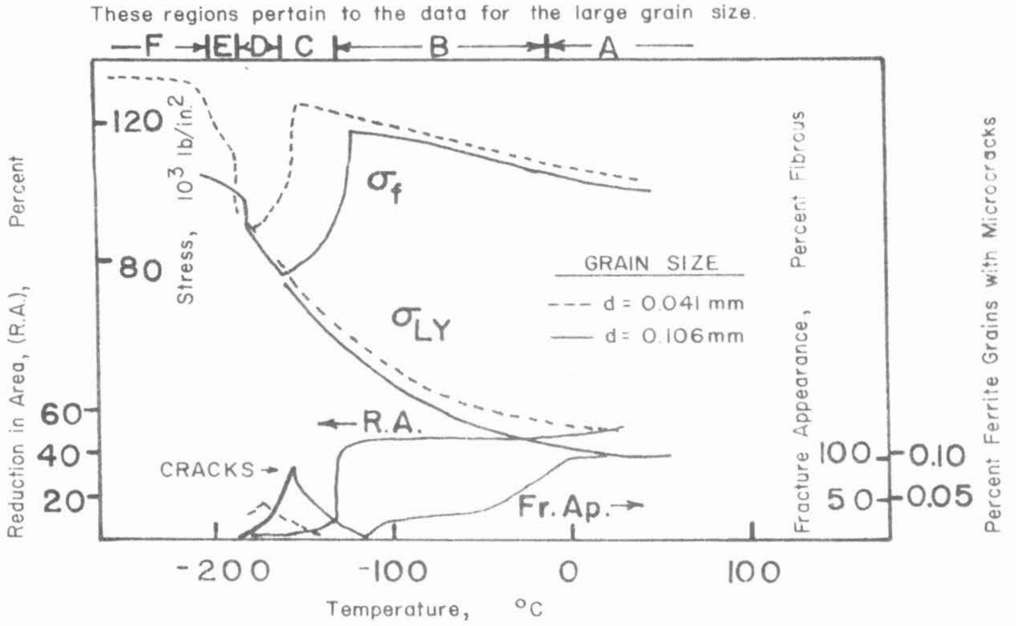

Region or Boundary	Distinctive Characteristic
A	100 percent fibrous fracture.
B/C	Fracture stress and reduction in area fall sharply with decreasing temperature.
D	Fracture and lower yield stresses almost identical, but yielding always observed prior to fracture.
D/E	"Microcrack transition temperature" - temperature at (and below) which crack propagation to failure occurs at onset of gross yielding.
E	No drop in load from upper to lower yield prior to fracture. Fracture stress values scatter about extrapolated upper yield stress curve. Microcracks not found.
F	Fracture stress is below extrapolated upper yield stress, but at stress level for onset of mechanical twinning.

Fig. 1. Selected fracture and yield data for unnotched tensile specimens as functions of temperature. (Ref. 15)

investigation.

The second feature is that the variation of the percentage of grains cracked with temperature clearly indicates at least a two-stage crack process -- 1) microcrack nucleation and 2) subsequent growth through the grain boundaries, as had been suggested by Cottrell (16) and Petch (17). The change in microcrack density with yield stress values suggests that microcrack production is fairly easy in region D. However, the probability that a microcrack which has been nucleated also meets the requirements for propagation decreases with decreasing yield stress (or decreasing tensile stress). The microcrack nucleation rate in region C also decreases sharply with decreasing yield stress, thus greatly inhibiting fracture.

The above discussion of the data reported by Hahn, et al. (15) has been based on the yield stress, rather than the temperature, as the important variable. Hahn, et al., varied both the strain rate and the temperature in a special set of experiments and found that the microcrack rate varied with these two variables as a direct function of the lower yield stress, which is also a function of the strain rate and the temperature. Hendrickson, Wood and Clark (27) have also shown that the nominal fracture load for notched steel specimens depends upon the yield stress and is not otherwise dependent upon the temperature and stress rate.

The third feature of Fig. 1 to be noted is that the fracture stress is not a constant as the yield stress changes. Thus a maximum tensile stress criterion for brittle fracture initiation is manifestly unsuitable for conditions of uniaxial tension, where the maximum tensile stress is equal to the yield stress. The superposition of a hydrostatic tensile stress state upon a uniaxial stress state, as is more nearly the case for notched specimens, may be expected to affect the fracture characteristics of the steel. In a notched specimen the relative magnitudes of the shear stress and the tensile stress may be varied, with the possible consequence that a different stage of the fracture initiation process becomes the critical one at a given yield strength.

B. Triaxial Stress State - Notches, cracks, or other reentrant geometrical features in a material create local triaxial stress states in otherwise uniformly stressed objects. Notches or cracks which penetrate in a direction transverse to the nominal tensile stress are of prime interest in fracture investigations. Elastic stress calculations predict intensification (concentration) of the nominal longitudinal tensile stress near a notch and also the existence of a transverse tensile stress perpendicular to the root of the notch. This transverse tensile stress is zero at the notch root (free surface) and attains a maximum value in the order of a notch root radius below the root.

Large intensifications of the longitudinal tensile stress may be obtained in elastic media, as has been shown to be the case at the atomic scale tip of a Griffith crack (8, 9). A large shear stress, equal to one-half the longitudinal stress at the notch root, causes plastic deformation in ductile materials (metals) and limits the longitudinal tensile stress at the notch root to the value of the tensile yield stress (assuming the Tresca yield criterion). Thus the effect of a notch on the longitudinal tensile stress at the surface (notch root) of an object is merely to cause the yield stress of the material to be attained locally at low nominal applied stress levels. However, the transverse tensile component of stress allows a hydrostatic tensile component of stress to be superimposed on the yield-stress-controlled shear stress state below the root of the notch. Tensile stresses greater than the uniaxial tensile yield stress can thus be attained in this triaxial stress state region and provide a means for obtaining different maximum tensile stress vs. total plastic shear strain states.

Brittle fracture in mild steel may be expected to be initiated at some small distance below the notch root - near enough to the root to benefit from the stress intensification there, but far enough under the root to benefit from the build-up of the transverse tensile stress and consequent triaxial stress state. Crussard et al. (18) have observed a transition of initiation of brittle fracture in a mild steel. A ductile mode of fracture initiation occurs at the notch root (large plastic strains) or a brittle mode of initiation occurs some distance below the notch (plastic strains $\approx$ Lüder's strain, high tensile stresses).

Calculation of stresses and strains in and near plastically deformed regions near the root of a notch in steel specimens is extremely difficult. Orowan (9) and Felbeck and Orowan (11) used approximations developed by Neuber (28) to calculate tensile stresses near a crack tip after plastic deformation had occurred. They also recognized that slip line theory (see Hill (29) for a discussion) predicted a maximum possible tensile stress ahead of the crack of about 2.6 times the uniaxial tensile yield stress. Felbeck and Orowan observed recurrence of extensive plastic deformation at the crack tip each time it was re-started after having been arrested because of relaxation of the load. They suggested that either the region of highest tensile stress must reach a critical size or that strain hardening was necessary to raise the tensile stress to re-initiate fracture. The crack may start in a ductile fashion and quickly convert to brittle propagation when the strain-rate-sensitive yield stress of the steel has increased sufficiently for the tensile stress to fulfill the Orowan-Irwin fracture criterion.

The work of Crussard, Borione, Plateau, Morillon and Maratray (18) also predates serious attempts at elastic-plastic stress analyses, but is monumental with respect to the selection of observations made on their notched and unnotched specimens. As with Felbeck and Orowan (11) and, later, Knott and Cottrell (19), they concluded that essentially brittle fracture (propagation) could be nucleated by the ductile fracture of a few grains. Crussard et al. also proposed that fracture could be nucleated in a brittle manner after some small plastic straining, in the order of Lüder's strain or slightly more. They deduced that fracture of notched specimens at low temperatures sometimes occurred at the onset of yielding. This would correspond to the fracture characteristics of unnotched specimens observed by Hahn et al. (15) as shown in region E of Fig. 1.

Crussard et al. suggest that at higher temperatures (and higher values of the lower yield stress) fracture is initiated in the region where the product of local (macroscopic) tensile stress times the "rheotropic embrittlement" reaches a critical value. "Rheotropic embrittlement" is exhibited by unnotched tensile specimens in region D of Fig. 1 wherein fracture can occur at lower tensile stress values after small additional amounts of plastic strain beyond the Lüder's strain. Crussard et al. considered the point of maximum normal (tensile) stress to be an inadequate criterion for the site of origin of fracture.

Wedge-shaped zones of plastic deformation below the notch root and, in some cases, plastic hinges were revealed by Fry's reagent. (Plastic "wedges" and "hinges" are discussed by Wilshaw and Pratt (30) and Green and Hundy (20), respectively.) Crussard et al. calculated that plastic strains of the order of 3 to 12 percent were present in the wedge-shaped plastic enclaves. A bimodal fracture behavior (high vs. low nominal stress at fracture) was observed but could not be correlated with the occurrence of plastic arcs ("hinges") emanating from the plastic wedges.

c. Triaxial Stress State - Stress Analyses - A numerical elastic-plastic analysis of the state of stress occurring near the root of a notch after limited amounts of plastic deformation has been performed by Hendrickson, Wood and Clark (27). The numerical relaxation technique which they employed in their calculations has been described by Allen and Southwell (31). The assumptions and the results of the analyses performed by Hendrickson et al. are reviewed in Section 8.2. Upper yield point data from unnotched steel specimens and nominal fracture stress data from notched tensile specimens were analyzed by means of the results of the elastic-plastic stress analysis. The value of the calculated maximum tensile stress within the notched specimens just prior to fracture was found to be about 210, 000 lb/in.^{2} for a wide range of stress rates and testing temperatures. They thus reported evidence for a maximum tensile stress criterion for brittle fracture initiation when plastic strains are small.

Barton and Hall (32) have developed a more easily obtainable approximate elastic-plastic solution for notched specimens which has some of the character of the solution obtained by Hendrickson et al., but is less rigorous. Certain assumptions have been made concerning the character of the stress solutions, which removes these results one step further from a likelihood of accurately portraying the elastic-plastic stress distribution under a notch.

Slip-line theory (see Hill (29)) has been used by Wilshaw and Pratt (30) to determine the stresses in the plastic region under the root of a notch in a specimen loaded in bending. Slip-line theory applies rigorously only to a plastic-rigid material and can predict the shape and extent of plastic slip-line fields in such materials only. The small wedge-shaped plastic enclaves formed during initial yielding at a notch root in a mild steel (see Fig. 24, for example) are shaped in a manner suggestive of the slip-line field which would have been calculated for that region if extensive plastic deformation had occurred. However, slip-line theory predicts an absence of plastic enclaves until general yield of the specimen is attained. The existence of wedge-shaped plastic enclaves at earlier stages of loading is rationalized by recalling that steel is not rigid and that the stresses and strains will take on the necessary, albeit unknown, values at the tip of the plastic wedges to enable these wedges to terminate in an elastic region.

Slip-line theory cannot predict the size and shape of small plastic enclaves under the common assumption that the enclave is embedded in a rigid matrix. The elastic-plastic stress analysis performed by Hendrickson et al. (27) does predict the location of the elastic-plastic boundary as part of its solution. However, the predicted shape does not compare very favorably with the observed enclaves near notch roots, (27) vs. (18, 30).

Verifying the results of a stress analysis is extremely difficult. Some researchers have assumed a maximum tensile stress criterion for brittle fracture initiation and have used this to modify, support, or in other ways interact with their stress analysis approximations (30, 33). Subtleties of brittle fracture behavior, such as "rheotropic embrittlement" discussed by Crussard et al. (18) or "size effects" may be difficult to analyze by means of prejudiced stress analyses.

D. Specimen Size - Elastic and plastic theories predict that the stress-strain state of an object is dependent only upon the applied stresses, the geometric shape of the object, and the mechanical properties of the material, and is independent of the geometrical scale factor. Thus a simple maximum tensile stress criterion for fracture initiation predicts an absence of a specimen size effect. However, small scale specimens are observed to break at higher nominal stress values (6, 34, 35) or after absorption of a greater amount of energy per unit volume (5) than large scale specimens. Extensive plastic deformation precedes fracture in many of the reported investigations of scale size effects because brittle fracture initiation is suppressed by the use of the small scale specimens employed in the investigations.

A statistical approach to the geometrical scale effect on fracture strength is reported (34, 35, 36) to have been investigated quantitatively by W. Weibull. The theory is based on the assumption that defects, real or potential, of varying severity are present within the material and that the strength of an object is determined by the worst combination of stress level and defect severity. A size effect results because larger specimens have a higher probability of containing the relatively more scarce, very severe defects in a highly stressed region. Fisher and Hollomon (37) have shown how fracture stress (and fracture stress frequency distribution) may be expected to vary with defect frequency for an assumed defect severity distribution. Irwin (36) has analyzed the size effect data of Davidenkov, Shevandin and Wittmann (34) and Brown, Lubahn and Ebert (35) statistically and has found good agreement between the experimental data and the statistical theory. Davidenkov et al. have suggested that a large number of fracture specimens with many circumferential notches may aid in experimentally determining a limiting fracture brittleness for large size specimens. Lubahn and Yukawa (6), on the other hand, found that the fracture strength of very small scale notch-bend specimens approached the strength of unnotched specimens as the size of the notch-bend specimens was decreased.

Bilby, Cottrell and Swinden (21) have chosen a quasi-dislocation model to relate "displacements" at a notch root to the geometrical scale and the applied stress. The model is equivalent to discontinuous plastic strain over narrow bands of appropriate (experimentally observed) orientation with respect to the notch together with the statement that a region of a certain size (at the notch tip) must be strained a certain amount to initiate fracture. This view is not an explanation, rather it is a restatement of the size effect. Felbeck and Orowan (11) used essentially the same concept earlier to explain nominal agreement (actually, disagreement) of their fracture stress vs. crack depth data with the Orowan-Irwin fracture criterion. They pointed out that if the mean tensile stress needed to produce a plastic enclave of radius r at the tip of a crack of length c when the yield stress is σ_m is given approximately by

$$\sigma \approx \sigma_m \left(\frac{1}{2}\right)\sqrt{\frac{r}{c}}, \qquad [1.2]$$

as has been proposed by Neuber (28, 9), then, "if . . . the size of the plastically deformed region required for starting cleavage is fairly independent of the crack length, the fracture stress should be inversely proportional to $\sqrt{c}$." The observations of Bilby et al. (21) and Felbeck and Orowan (11) would seem to apply to the ductile mode of initiation of brittle fracture.

The size of the "plastically deformed region" near the notch (crack) root, as mentioned above, is of the order of 0.015 in. in steel (11, 28). Parker (38) notes that geometric similarity of scaled specimens is destroyed when the first microcrack of grain diameter dimensions forms. Morrison (39) and Knott and Cottrell (19) have reported that initiation of yielding is delayed until the elastically calculated shear stress at a point one or several grain diameters below the surface has reached the yield value. (But Griffiths and Cottrell (40) found no such "elastic superstressing" on notched silicon iron specimens when an etch pit technique was used to increase the sensitivity of observation of first plastic strains. However, it is not clear what dislocation-observable feature distinguishes microslip from slip-band-type of plastic deformation.) Thus there is evidence of structure size vs. specimen size interaction in yielding and fracture, but the exact nature of the interaction is not clear.

E. Grain Size - Both Petch (24) and Low (14) have fractured unnotched specimens of different grain sizes at liquid nitrogen temperature. Fracture in the small grain size specimens was preceded by larger amounts of plastic strain than occurred in the specimens with the larger grain sizes. Petch modified his fracture data in an attempt to compensate for the variation in plastic strain at fracture. This modified fracture stress is remarkably close to the lower yield stress. Low did not modify his fracture stress values to compensate for the plastic strain but inferred 1) that fracture occurs at the lower yield stress for large grain sizes and 2) that the product of the fracture stress and the square root of the average grain diameter is a constant for small grain sizes, as shown by the straight solid lines in Fig. 2.

Gensamer (26) and Hahn et al. (15) have varied the testing temperature in fracture tests on unnotched specimens with several different grain sizes. Reference to the dashed and solid fracture curves in Fig. 1 shows that the relative fracture behavior of steels of two different grain sizes is quite sensitive to the test temperature in the regions lettered C, D and E.

The fracture behaviors represented in Figs. 1 and 2 show remarkably similar features; fracture in the left-hand portion of both

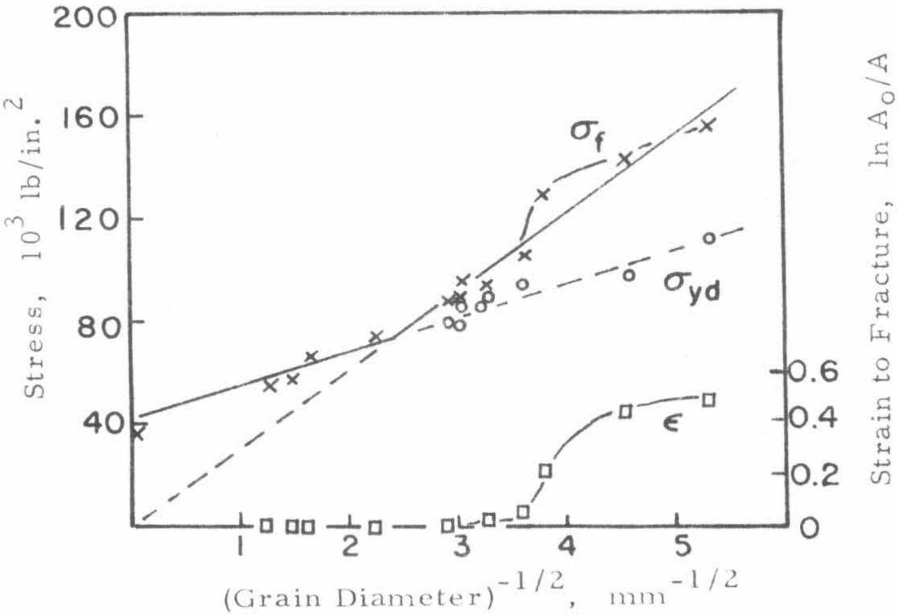

Fig. 2. Fracture and yield data for unnotched tensile specimens as functions of grain size. (Ref. 14.) Curved line for fracture stress is author's interpretation of fracture data trend.

figures occurs at the yield stress while fracture in the right-hand portion is preceded by large plastic strains and strain hardening. A better view of the fracture stresses could be obtained from a three dimensional representation of fracture stress as a function of temperature (or lower yield stress) and grain size. Fig. 1 would represent two sections at constant grain size and Fig. 2 would represent a section at constant temperature (or lower yield stress) of the hypothetical three dimensional figure. A trough of minimum fracture stress values, representing the boundary between regions C and D in Fig. 1, would angle down through this three dimensional figure. The section represented by the data reported by Low (see Fig. 2) includes fractures on both the ductile and brittle sides of the trough and cannot be considered simply as a portrayal of "fracture stress as a function of grain size." The fracture data of Fig. 2 may be better represented by the solid curved line where large plastic strains precede fracture, in accord with the fracture curves of Fig. 1.

1.5 Summary of Assumed State of Knowledge of Brittle Fracture

The foregoing discussion of investigations of brittle fracture in mild steel is by no means all-inclusive with respect to the observations which have been made or the conclusions that have been reached. Some studies have been made on the correlation of fracture data for nominally similar structures and others on the relative effects of plane-stress vs. plane-strain stress state conditions. Attention has been directed here to those investigations which appeared to lend themselves to generalizations, rather than restrictions, of fracture concepts.

Plane strain was of particular interest because of its similarity to the axial symmetry employed in the present investigations performed in connection with this thesis.

The present state of knowledge concerning the initiation of brittle fracture can be summarized in the following brief statements:

- There is evidence both for and against a maximum tensile stress criterion for the initiation of brittle fracture.
- Plastic straining must precede fracture initiation.
- There may be a rheotropic embrittlement effect associated with the amount of (small) pre-fracture plastic strain.
- Brittle fracture may be initiated by a brittle mode at some point below a notch root or by a ductile mode at the notch root after intense local plastic straining.
- The fracture initiation behavior of steel is dependent primarily upon its yield stress at different combinations of temperature and strain rate.
- Both grain size and specimen size effects are observed in fracture, smaller sizes tending to inhibit fracture.
- The geometry size effect may be rationalized in some cases by statistical theory.
- The Griffith or Orowan-Irwin energy condition for fracture initiation from microcracks is a necessary condition but an inadequate criterion because of ambiguity in the value of the plastic work term.
- The stress-strain requirements for nucleating a microcrack are different from those for subsequent propagation (fracture

initiation).

- Elastic-plastic stress-strain analyses of triaxial stress states near notches in steels which exhibit upper and lower yield stress phenomena are difficult to perform and cannot seem to be made to include an appropriate (yet unknown) characterization of the yield instability behavior.

In spite of the large number of observations made in brittle fracture investigations, there is a notable lack of coordination or reconciliation of the results. Furthermore, no general fracture criterion has been formulated which can be used to predict fracture behavior in a mild steel object of random shape and loading. While the present work will not disclose the desired general fracture criterion, it may aid in the qualitative understanding of yield and fracture behavior of mild steel.

1.6 Purpose and Method of the Present Investigation

Apparent success of the elastic-plastic stress analysis calculated by Hendrickson, Wood and Clark (27) in predicting the state of stress after local yielding had occurred and experimental support of a maximum tensile stress criterion for brittle fracture led to the question - what is the influence of grain size upon the value of the maximum tensile stress at the instant of fracture initiation in a region with a triaxial tensile stress state? The answer to this question was the original objective of this investigation. However, the results of experiments performed in the early phases of this investigation led to doubt concerning the correctness of the elastic-plastic stress analysis developed by Hendrickson et al.

The investigation described in this thesis has two main objectives: 1) to determine the mechanical properties of a mild steel in and adjacent to small plastic enclaves (at notches) and to investigate the appropriateness of elastic-plastic stress analysis techniques in predicting the stress state of such regions and 2) to determine the stress-strain state conducive to fracture initiation in regions with a high hydrostatic tensile stress component through the application of a suitable stress analysis to notched specimens loaded in tension.

Deductions concerning the properties of annealed mild steel in and near small plastic enclaves have been derived from observations of plastic strain patterns revealed in notched specimens by a macroscopic etch technique. A stress analysis based on slip line theory in the plastic enclaves has been developed and has been checked against the quasi-statically loaded notched specimens.

Yield stress data from unnotched tensile specimens and nominal fracture stress data from axiallysymmetric notched tensile specimens have been obtained over a wide range of stress rates at several temperatures. The test temperature and nominal stress rate were varied to obtain a range of stress states below the root of the notched specimens as a result of the variation of the yield stress with these parameters. A means for correlating the lower yield stress values obtained from unnotched specimens with the yield stress of the material in the plastic enclave at the root of the notched specimens is described. This enables the stress analysis to be applied to the notched specimens in an attempt to deduce the stress state at the instant of fracture.

A metallographic search for microcracks and the use of different specimen sizes and grain sizes are techniques which were employed in an attempt to elucidate the fracture behavior of the notched steel specimens.

The work described in this thesis is intended to serve as a guide to the problems which will have to be solved before the true stress-strain state in the region of fracture initiation can be calculated.

II. MATERIAL AND TEST SPECIMENS

2.1 Material

The material used in this study was the same mild steel that was used by Hendrickson, Wood, and Clark (27) and by Clausing (23) in earlier fracture studies. The steel was obtained from the United States Steel Corporation, Torrance, California works, in the form of 5/8 in. diameter hot-rolled bars from one billet of heat No. 32882. The chemical analysis is: 0.19% C, 0.41% Mn, 0.06% Si, and 0.002% Aℓ. The steel is designated as silicon semi-killed by the supplier.

The two grain sizes used in this investigation were produced by annealing treatments in the austenite temperature range after all machining operations had been performed on the test specimens. The small grain size, ASTM grain size No. 8 1/4, was produced by a one-hour anneal at 1700°F. The large grain size, ASTM grain size No. 5 1/2, was produced by a four-hour anneal at 2125°F. All specimens were cooled slowly (less than 10°F per minute) in the furnace.

Yield and fracture behavior of the specimens of grain size No. 8 1/4 were uniform among the several batches which were produced. The yield and fracture characteristics of two batches of specimens of grain size 5 1/2 were slightly different, however. Note will be made of these differences at the appropriate times later in this report.

Decarburization of the specimens during heat treatment was averted by placing the specimens in a flowing inert atmosphere of helium which was passed first through a Drierite ($CaSO_4$) tower and then activated charcoal immersed in a liquid nitrogen bath. Surface coloration of the specimens indicated that some oxygen was present in the specimen chamber during annealing. However, microscopic examination of sections of the specimens revealed normal pearlite distribution up to the surface of the specimens. This was interpreted as meaning that decarburization was insignificant. A few specimens for special studies were annealed in a vacuum furnace. These specimens were not decarburized, either.

The ASTM grain size numbers for these steels were determined by counting the number of grains which appeared in random areas of a photomicrograph of the transverse section of the steel. The actual area was multiplied by 0.79 for purposes of calculating the ferrite grain size since approximately 21 percent of the area is pearlite. Thus, the ASTM grain size was taken as N in the equation

$$2^{N-1} = \left(\frac{\text{actual mag.}}{100\times}\right)^2 \left(\frac{\text{no. of grains within area} + \frac{1}{2}\,\text{no. of grains on boundary of area}}{0.79}\right).$$

Six groups of about 180 grains each were counted from small grain size specimens. The calculated ASTM numbers ranged from 8.0 to 8.45. This average grain size is taken as 8 1/4 in this work. Nine groups of about 100 grains each were counted from three large grain size specimens. The calculated ASTM numbers ranged from 5.20 to 5.70. The average was taken to be 5 1/2.

Most of the large grain diameters in the photomicrographs of the steel with the large grain size were about 0.005 in. with an occasional 0.006 to 0.007 in. diameter. The range of large grain diameters for the small grain size specimens was mostly 0.0015 to 0.002 in.

with an occasional maximum of 0.0025 in.

2.2 Test Specimens

Axially symmetric, notched and unnotched, tensile specimens of two geometric scales were prepared from the bar stock. The linear scale ratio of the two sizes is about 2.6, which is also the ratio of the average ferrite grain diameters studied in this investigation.

Drawings of the large scale notched (series A) and unnotched (series B) specimens are shown in Fig. 3. The hyperboloid generating process described by Hendrickson (41) was employed to form the notch contour. The finite thickness of the edge and the flexibility of the cut-off wheel prevented the formation of an exact hyperboloid of revolution and also allowed the notch contour to vary from specimen to specimen.

The radius of the root of the notch was calculated from measurements taken with a Kodak contour projector. The method of calculation is discussed by Hendrickson (41). The values of the root radius, ρ, varied from 0.0065 to 0.0119 in. The theoretical root radius of a hyperboloid of revolution with a 29° asymptotic included angle and a minimum section diameter of 0.300 in. is 0.010 in. The diameters of the minimum sections of the specimens varied, so the measure of the fidelity of the notch contour was taken to be $\rho \div \left(0.010 \times \frac{d}{0.300}\right)$, where d is the minimum section diameter. The fidelity of most of these notches ranged from 0.83 to 1.02.

The small scale specimens, series D - notched, and series E - unnotched (see Fig. 4), were made with tapered seating surfaces at each end to ensure alignment in mating tapered surfaces in the grips.

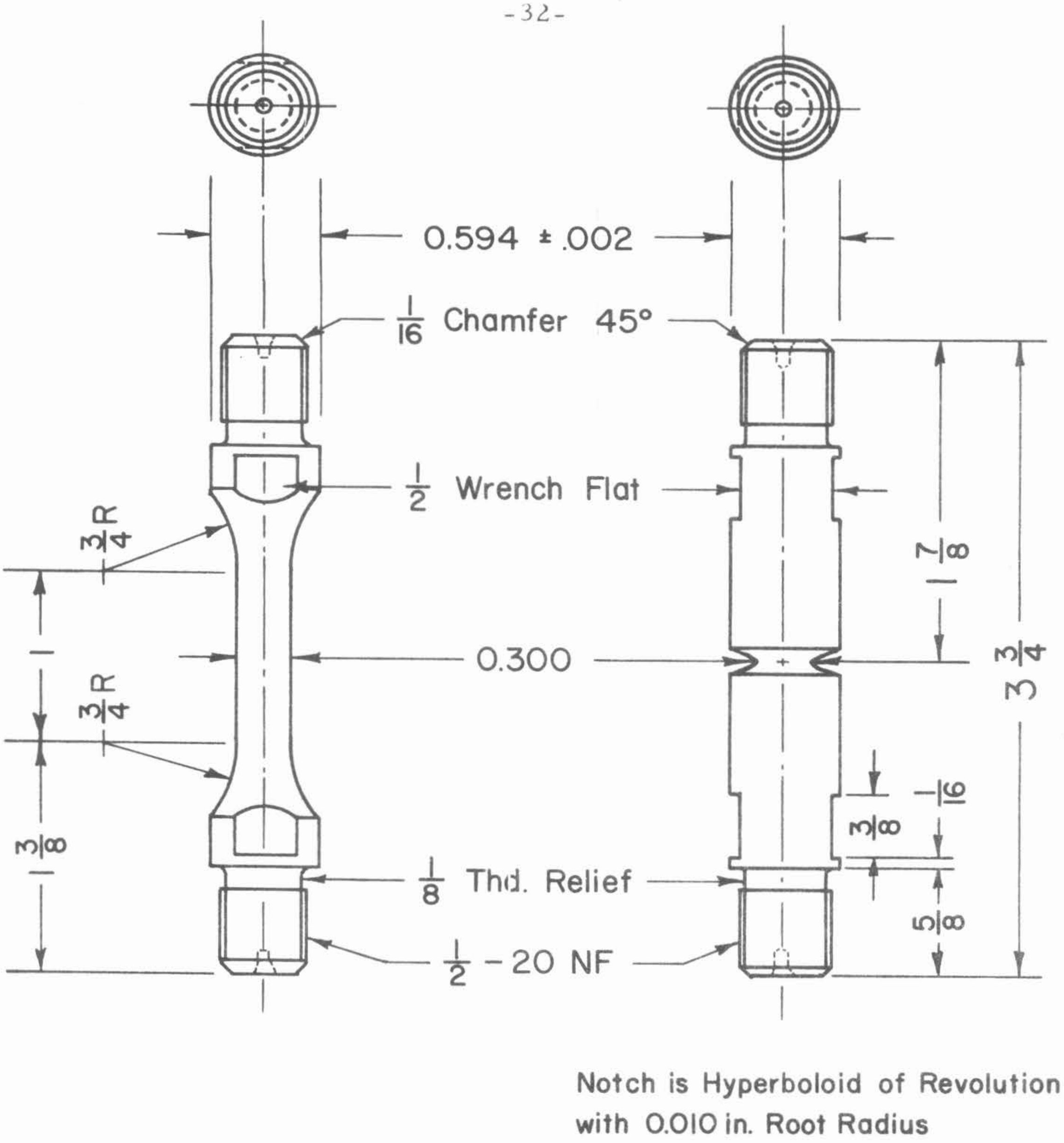

a. Unnotched specimen

b. Notched specimen

Fig. 3. Large scale tensile specimens.

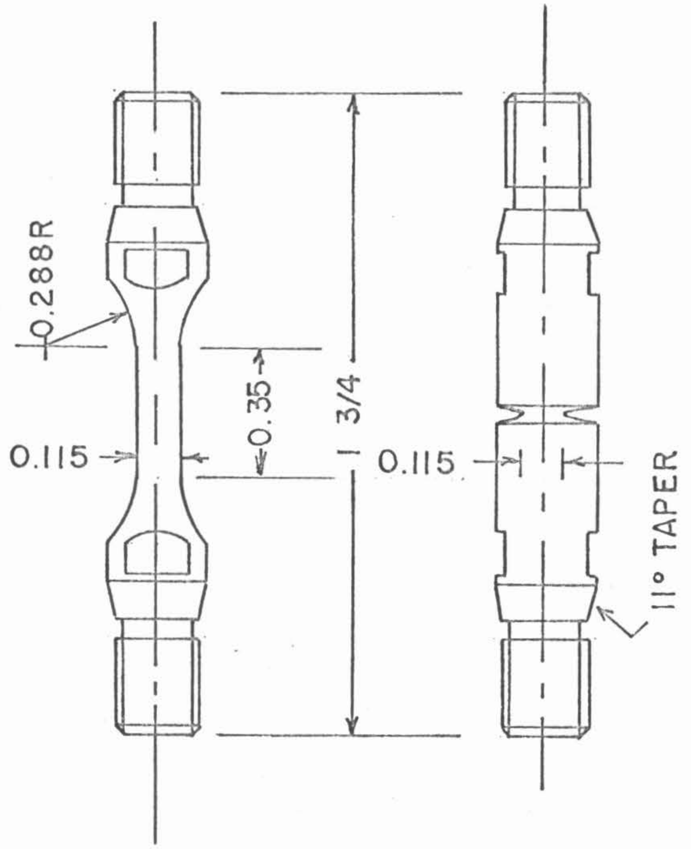

Fig. 4. Small scale tensile specimens.

The grips incorporate thin flexture elements designed to minimize bending loads. These extra precautions to minimize bending in the small scale specimens are necessary to achieve results comparable to the larger specimens.

The gage sections of the unnotched specimens, series E, were ground to the final shape while the specimens were on centers in a lathe. The tapered seating surfaces were also formed while the specimens were on centers.

The notch contours in the small scale, series D, specimens were generated in a manner similar to that used on the large-scale notched specimens. However, the rubber-bonded corundum wheel was replaced by a slitting saw which had been ground to an (infinitely) sharp "V" cutting edge having an included angle of 18°. The rigidity of this cutter and the very small "radius" of the cutting edge were important factors in the successful production of the small scale notches.

The values of the root radii of the D-series notches, calculated from measurements taken on a Kodak contour projector, varied from 0.00360 to 0.00395 in. The theoretical value for the root radius of a 29° included angle hyperboloid with a minimum section diameter of 0.115 in. is 0.00383 in. The diameter of the minimum section of these specimens varied from 0.111 to 0.115 in. The fidelity of these notch roots ranged from 0.935 to 1.05.

III. EQUIPMENT AND TEST PROCEDURE

3.1 Equipment for Tensile Tests

A mechanically-controlled hydraulic tensile testing machine of 10,000 lb. capacity was employed to apply tensile loads to the test specimens. The machine was specially designed by Clark and Wood (42) to provide variable constant rates of tensile load application up to about 10^6 lb/sec. The highest rate of loading is still slow enough that stress wave propagation need not be considered. The basic element of the machine is a large (50 in.^{2}) loading piston which faces a high pressure (up to 250 lb./in.^{2}) air chamber on one side and an oil filled chamber on the other side. The oil is used to control the displacement of the loading piston. At high rates of loading, corresponding to 7×10^5 to 2×10^7 lb./in.^{2}sec., the movement of the large loading piston is hydraulically controlled by a small (5 in.^{2}) piston which follows a mechanically driven cam. Stress rates in the range of 3×10^1 to 3×10^3 lb./in.^{2}sec. were obtained by leaking the hydraulic control oil through a needle valve with a constant pressure drop maintained across the valve. The intermediate stress rates between 3×10^3 and 7×10^5 lb./in.^{2}sec. were obtained by the needle valve leak technique without a constant pressure drop. The rates of loading in this last range were calculated from the average rate of increase of load during the top 10 percent of load before yield or fracture.

A specimen grip system to transmit tensile loads from the machine to the specimen, a dynamometer system for detecting the magnitude of the load applied to a specimen, and a cold bath system to cool the specimen to the desired test temperature were attached to the rapid loading machine. The dynamometer system is specially designed and, together with the specimen grip system, forms an integral part of the load transfer system. Different sets of load transfer systems were employed for the two different scale size specimens because of the different load capacity and load axiality requirements.

The specimen grip system for the large scale specimens, series A and B, consisted of stainless steel rods screwed into spherical seat plugs, as shown in Fig. 5. The spherical surfaces of the plugs and the mating seats in the machine were lubricated with Molykote, Type G, a molybdenum disulfide base lubricant, to minimize bending stresses in the specimens. When the spherical seats were carefully seated under a small preload, the bending stress in a series B unnotched specimen was less than 3 percent of the nominal axial stress.

The specimen grip system for the small scale specimens, series D and E, incorporated two sets of thin flexure sections to minimize bending. This system is shown in Fig. 6. The flexure grips were made from 17-4 PH stainless steel and were hardened by a precipitation heat treatment after machining. The flexure grips were slightly bent, but the bending moment necessary to elastically straighten the worst section would give rise to a maximum bending stress of only 600 lb./in.^{2} in the unnotched, series E specimens. The upper end of this specimen grip system is held in alignment with the lower end by means of a sleeve, which is part of the dynamometer system. The dynamometer was accurately aligned in the testing machine and

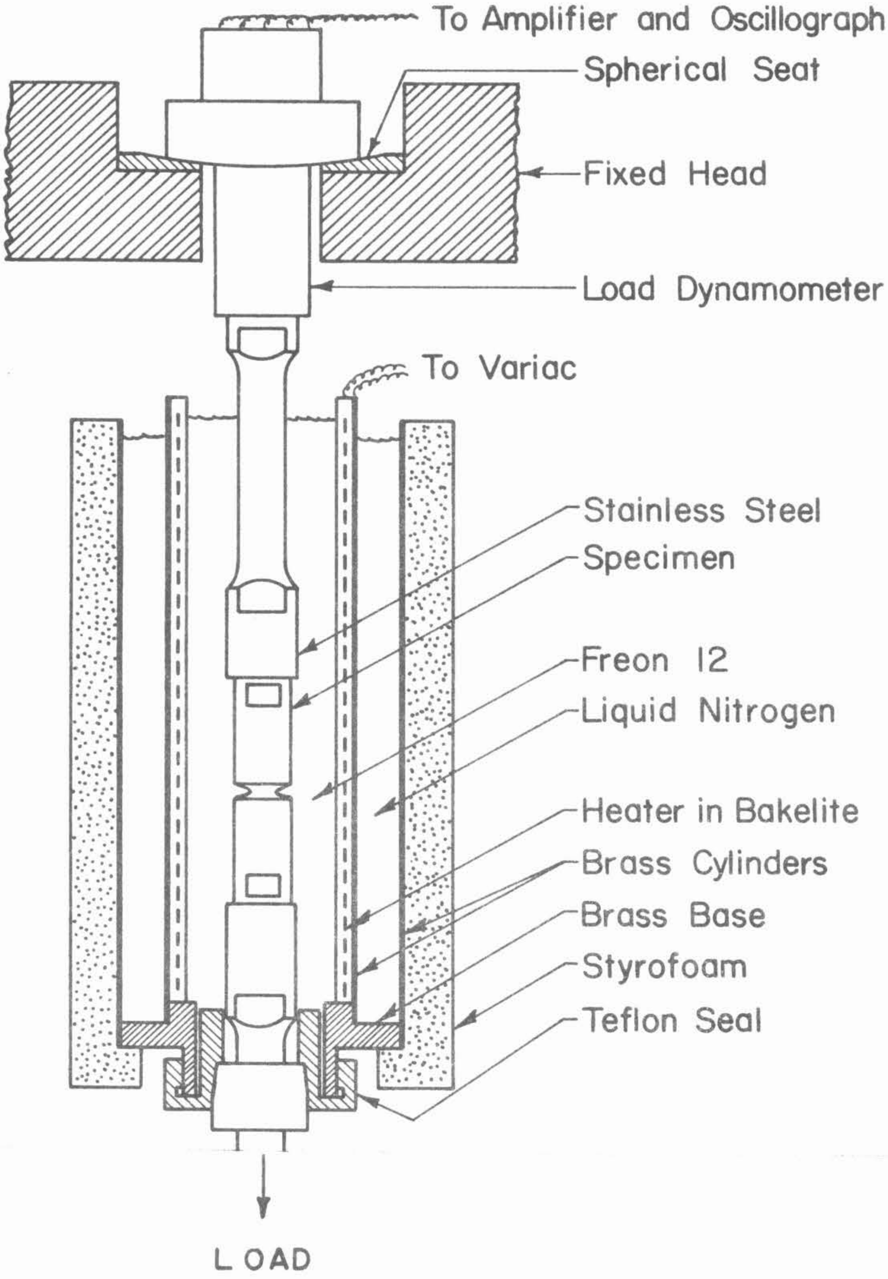

Fig. 5. Suspension assembly and cold bath for large scale specimens.

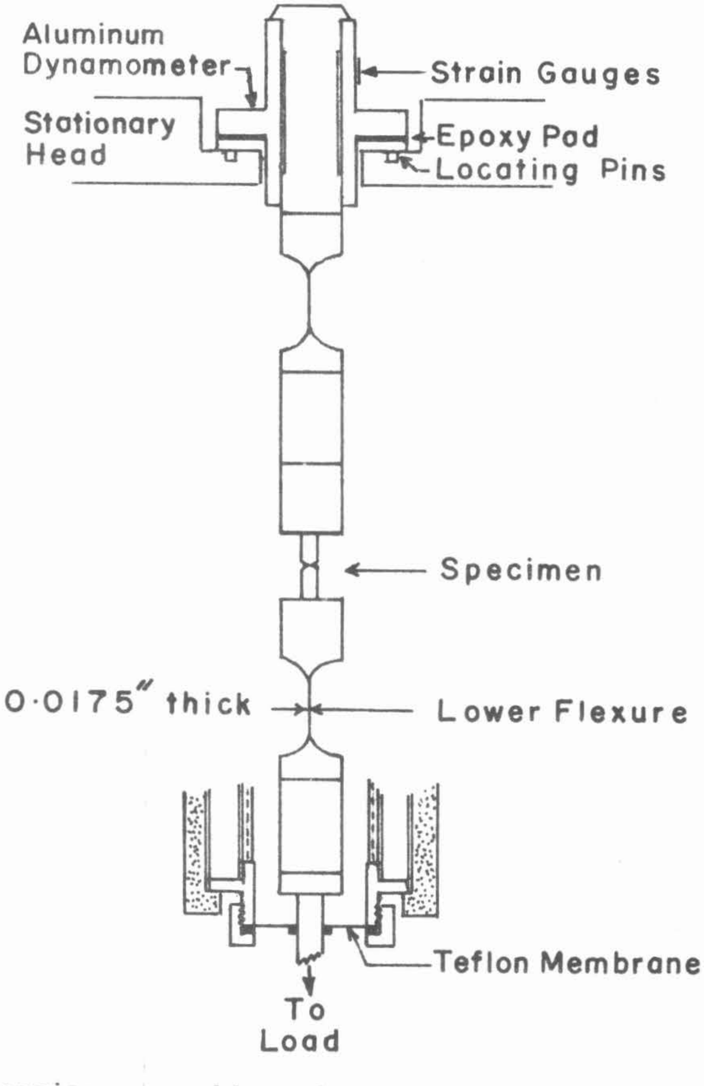

Fig. 6. Suspension assembly and cold bath for small scale specimens.

cemented with an epoxy cement to an aluminum pad which was positioned in the machine by locating pins.

The stiffness of the specimen grip system and rapid loading machine and the dimensions of the test specimens are such that a loading-piston velocity of 0.35 in./sec produces a nominal pre-yield elastic stress rate of 10^6 lb / in.^{2}sec in the large scale specimens and a nominal stress rate of 2×10^6 lb/ in.^{2}sec in the small scale specimens.

The load dynamometer for each load transfer system incorporates four SR-4 resistance-sensitive strain gages cemented to a thin cylindrical section. The 10,000 lb. capacity dynamometer for the large specimens is made of hardened steel and serves as the upper spherical seat plug. This dynamometer was calibrated in a beam-balance, static testing machine whose accuracy was ± 1 percent. The 1700 lb. capacity dynamometer for the small scale specimens was made from 6061 T6 aluminum alloy. It was calibrated with 100 lb. of dead weights in conjunction with a 10× lever system. The output of this dynamometer was found to be linear with the load in the range 100 to 1000 lb.; the linearity is assumed to continue up to the 1700 lb. capacity of the dynamometer.

The strain gage bridge output of the dynamometers was amplified by a Consolidated Electrodynamics 3-kilocycle carrier amplifier and recorded by means of an oscillograph employing high-frequency moving-coil galvanometers and traveling light-sensitive paper. The flat-frequency response range of this recording system is 0 to 500 cycles per sec. The amplifying system was calibrated before and after each test by means of a known resistance shunt connected across one arm of the strain gage bridge.

A double-walled cylindrical container, shown in Fig. 5, is the principal unit of the cold bath system. Liquid Freon 12 in the inner chamber was in contact with the specimens and part of the specimen grips and acted as the heat transfer agent. The cold bath container was sealed to and supported by the lower specimen grips during tests on the large specimens, as shown in Fig. 5. For tests on the small specimens, the cold bath container was sealed to the lower flexure grips through a flexible teflon membrane and was supported directly by the rapid loading machine. This sealing arrangement is illustrated in Fig. 6.

Three different test temperatures were used in this investigation: -21°F (-29°C), -111°F (-79°C), and -200°F (-129°C). These were obtained by means of suitable liquid baths in the double-walled container surrounding the test specimen. The temperature of -21°F was obtained by allowing Freon 12 to boil in contact with the specimen and the extension grips. A mixture of dry ice and Freon 12 was used to obtain the nominal test temperature of -111°F. Only the inner cylinder of the cold bath container was filled with coolant for tests conducted at these two temperatures. The nominal test temperature of -200°F was obtained by filling the entire outer annular chamber of the cold-bath system with liquid nitrogen, the inner chamber with Freon 12, and adjusting the power supplied to the electric heating element imbedded in the intermediate insulating Bakelite cylinder.

The temperatures were determined from potentiometer measurements of the emf of copper-constantan thermocouples that were attached to A- and B-series specimens with "Scotch" electrical tape or were attached to the flexure grips with screws just above and below the D- and E-series specimens. The maximum temperature range determined for tests at -21°F (-29°C) was from -20.2 to 21.4°F. For tests at a nominal temperature of -111°F (-79°C), the actual temperature measurements ranged from -109 to -112°F. For the tests at a nominal temperature of -200°F (-129°C), the measured temperatures ranged between -195 and -205°F.

3.2 Procedure for Tensile Tests

The upper and lower yield stresses of unnotched tensile specimens were obtained in the rapid loading machine described in Section 3.1 over a range of pre-yield elastic stress rates at several temperatures. The yield stresses of series B specimens of grain size 5 1/2 were obtained in the stress rate range of 3×10^{1} to 2×10^{7} lb. in.$^{-2}$sec.$^{-1}$ at -200°F, -111°F, and -21°F.

The upper and lower yield stresses of series B specimens of grain size 8 1/4 were obtained at -111°F in the stress rate range of 3×10^{1} to 2×10^{7} lb. in.$^{-2}$sec.$^{-1}$. The yield stresses of one specimen were determined at -21°F and just the upper yield stress of another specimen was determined at -200°F, both of these at about 1.1×10^{6} lb. in.$^{-2}$sec.$^{-1}$. Three series B and three series E specimens which had been annealed together were tested in pairs of a large and a small specimen to determine specimen size effects on the yield stresses. Two pairs were tested at -111°F and the other pair at room temperature (73°F, 23°C).

Finally, the yield stresses of series B specimens of both grain sizes were determined under the quasi-static conditions of about 10^2 lb /in.^{2}sec at room temperature (79°F, 26°C). These yield data were obtained so that notched specimens could be loaded to known values of the ratio of the nominal stress to the yield stress prior to examination for zones of plastic deformation.

Tensile tests on notched specimens were of three types: 1) loading to fracture, 2) loading to a predetermined stress slightly less than the nominal fracture stress, and 3) quasi-static loading to a particular value of σ_{nom}/σ_{yd}, as noted in the preceding paragraph.

Large grain size, series A specimens were loaded to fracture over a range of stress rates at each of three test temperatures. Most of the tests at -111°F and -21°F were conducted at the higher stress rate to avoid extensive plastic deformation.

Small grain size, series A specimens were loaded to fracture at -111°F and -200°F. Seven series D specimens of this grain size were also tested at -200°F to investigate specimen size effects in notched specimens.

Three large grain size specimens, A-31, A-39, and A-7, were loaded to high levels at a rate of about 2.4×10^6 lb/in.^{2} sec at -111°F and then unloaded so that a metallographic search for microcracks near the notch root could be made. Specimens A-39 and A-7 were loaded to a slightly higher level than the nominal fracture stresses of two other specimens at that temperature and stress rate. Stress history details of these specimens are included in Table 2 in Section

4.3. Specimens A-31 and A-7 were held near the highest stress level for several minutes to allow general yielding to occur and allow microcracks to open wider and thus be more easily detected. The third specimen was unloaded as quickly as possible after the initial high stress rate test at -111°F and was subsequently elongated slowly in tension at room temperature. Room temperature yielding should not create new microcracks, but should widen pre-existing microcracks.

3.3 Search for Microcracks

A metallographic search for microcracks was conducted in three unfractured large grain size specimens, A-31, A-39, and A-7, after they had been loaded almost to their nominal fracture stress level. The specimens were turned in a lathe to a diameter just greater than the diameter of the notch section so that the notch root could be accurately located. Very small reference holes were drilled radially into the specimens near the notch root. The specimens were then turned on centers in a lathe and hand polished with abrasive papers and diamond-loaded polishing cloths. A circumferential reference line was scribed through the drilled reference holes. These cylindrical examination surfaces were prepared at 0.003 in. intervals to depths of about 0.009 to 0.019 in. The 0.003 in. depth increments for examination are smaller than the typical grain diameters of about 0.005 in.

The polished cylindrical surface was examined for microcracks under a low power (30×) binocular microscope in essentially dark field illumination and also at higher magnifications in bright field in the as-polished and in the etched (5 sec in 4% HNO_3 in amyl alcohol) conditions. Photomicrographs at about 35× were taken of 0.030 in. wide circumferential strips centered under the notch root on each cylindrical examination surface. This procedure permits re-examination of the overlying surfaces in the event a microcrack is found deeper in the specimen. The technique employed for taking the photomicrographs of the cylindrical surface is discussed in Appendix I.

3.4 Determination of Plastic Zones

An attempt was made to determine the extent of the plastic enclaves near the root of the notched specimens by microhardness measurements with a Wilson Tukon Tester. This method was used earlier by Hendrickson, Wood, and Clark (27) in similar experiments. The method depends on the increase in hardness of ferrite in the plastic zone due to strain aging. The hardness values which were obtained in a survey for the present work varied randomly over a small range from grain to grain in the elastic region as well as in the plastic region. Although a few indentations could definitely be identified with the plastic region, the normal scatter of the hardness values prevented a determination of the elastic-plastic boundary.

Plastically deformed regions of nitrogen-bearing steels may be disclosed by the use of Fry's reagent. A silicon semi-killed steel does not respond differentially to this etching reagent, however. No other etching reagent was found that would reveal the plastically deformed zones in the steel used in the present investigation. (However, an etching reagent for this purpose has been reported recently by Clausing (23).) Apparent success in revealing the plastic enclaves was finally achieved after the specimens were given a surface nitriding treatment.

Three large and three small grain size, series A specimens which had been loaded under quasi-static conditions were prepared for determination of the plastically deformed regions. The specimens were iron plated for edge protection during polishing and then sectioned. Indentations were made with a Rockwell hardness tester on the sectioned surfaces to produce plastically deformed material which would serve to check the effectiveness of the subsequent nitriding and etching operations. The surfaces were then polished through 600 grit papers.

The specimens were nitrided in a hydrogen- 25 percent ammonia atmosphere at 950°F (510°C) for two hours and cooled by removing the specimen tube from the furnace. (Lower nitriding temperatures may be efficacious. One trial specimen responded satisfactorily after having been nitrided at 850°F (455°C).) An aging treatment of 50 min at 400°F (205°C) was used to allow the dissolved nitrogen to respond to the dislocations in the plastic zones and thus cause a contrast in response to Fry's reagent acting differentially on the plastic and the elastic regions. The response to Fry's reagent greatly improved after aging at room temperature for several months to over a year. Perhaps a better aging treatment would have been 17 hours at 150°C (300°F), as used by Crussard, et al. (18).

About 1 to 2×10^{-3} in. of steel was removed from the surface before final polishing and etching with a modified Fry's reagent. The composition of this reagent, which has been used by Hahn (56), is

$CuC\ell_2 \cdot 2H_2O$	19 g
$HC\ell$	40 cc
H_2O	30 cc
C_2H_5OH (ethyl alcohol)	25 cc.

The specimens were etched at room temperature for 3 to 6 sec.

Critical factors in the success of this etching procedure are the nitrogen concentration in the steel and especially the aging treatment. The condition of Fry's reagent was less important in these tests.

IV. EXPERIMENTAL RESULTS

4.1 Yield Data from Unnotched Specimens

The yield behavior of the steel was calculated from measurements of oscillograph records of load vs. time taken during the tensile tests on the unnotched specimens. Typical oscillograph records of tests on large and small grain size specimens are shown in Figs. 7 and 8, respectively. These records show the sharp drop in load supported by the specimen just after the upper yield stress has been reached. The records of Figs. 7 and 8a also exhibit the relatively constant load during specimen elongation at the lower yield stress. Figure 8b does not unequivocally show a lower yield stress plateau. This will be discussed later. The curves of Figs. 7a and 8b show a portion of the strain (and strain-rate) hardening curve following the lower yield stress. The curves of Figs. 7b and 8a do not show strain hardening because the loading piston of the testing machine reached the limit of its travel before the Lüder's band had propagated the entire gage length of the specimen.

The data obtained from the oscillograph records of load vs. time can be used to construct stress-strain diagrams when the spring constant of the specimen grips and testing machine is known. The stress-strain curves of Figs. 9 and 10 were obtained from Figs. 7a and 8b in this manner. A spring constant of 2.8×10^6 lb/in.^{2}sec was used for the large scale specimens of Fig. 9 and a spring constant of 5.2×10^6 lb/in.^{2}sec was used for the small scale specimen of Fig. 10. The strain calculations for the curves of

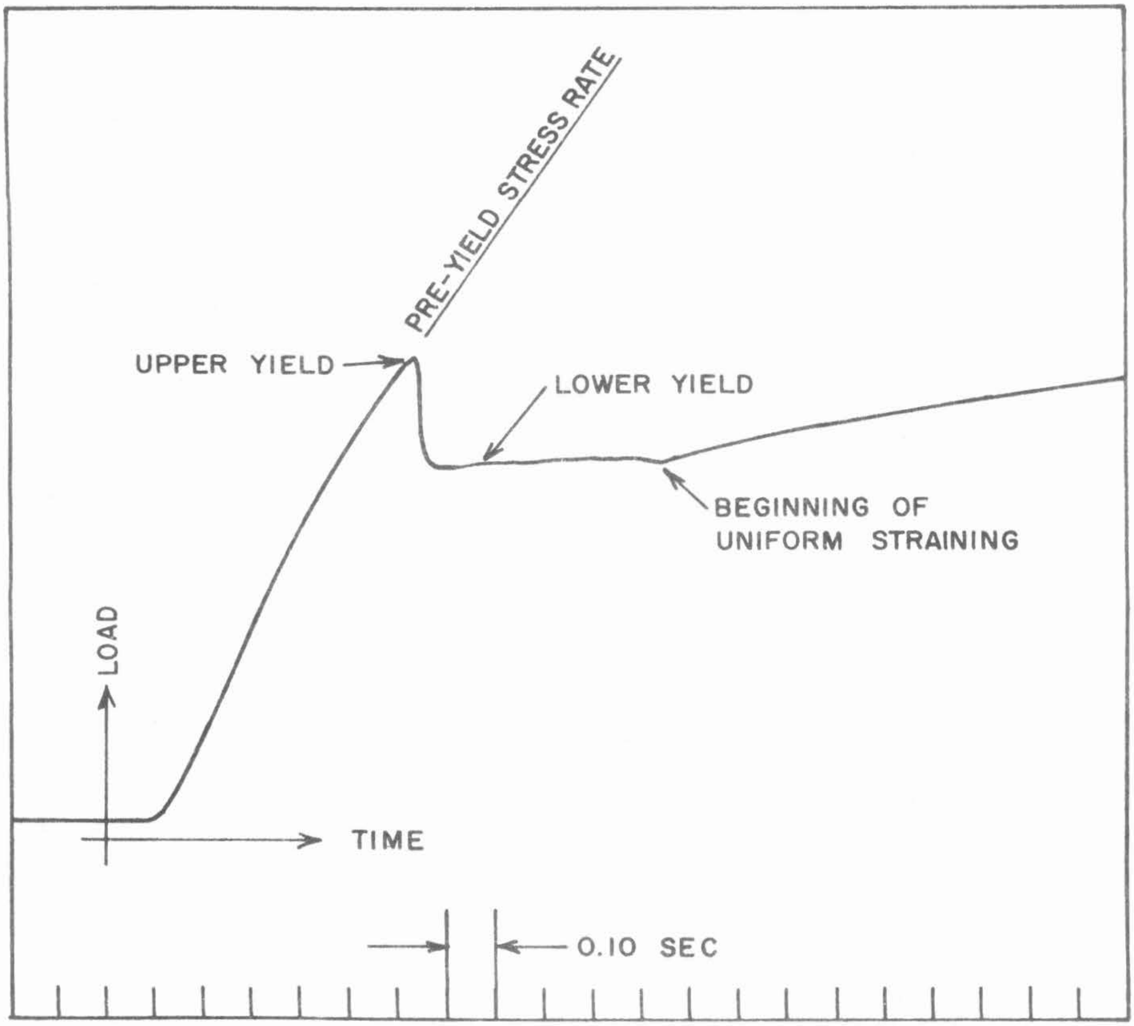

a. Specimen B-56; T = -21°F, $\dot{\sigma} = 6.8 \times 10^4$ lb/in.^{2}sec. Derived stress-strain curve shown in Fig. 9.

Fig. 7. Typical load vs. time records of unnotched specimens, ASTM grain size 5 1/2.

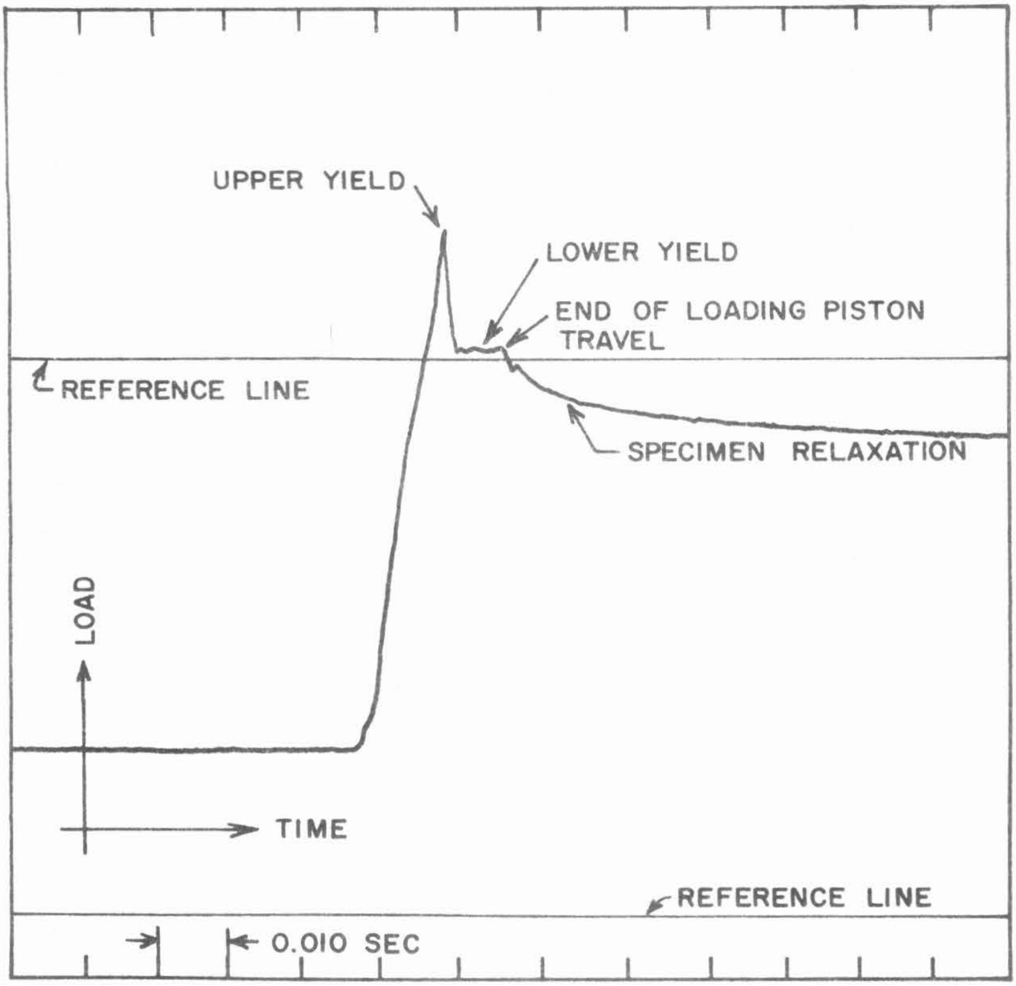

b. Specimen B-26; T = -111°F, $\dot{\sigma} = 8.8 \times 10^6$ lb/in.^{2}sec.

Fig. 7. (Continued.)

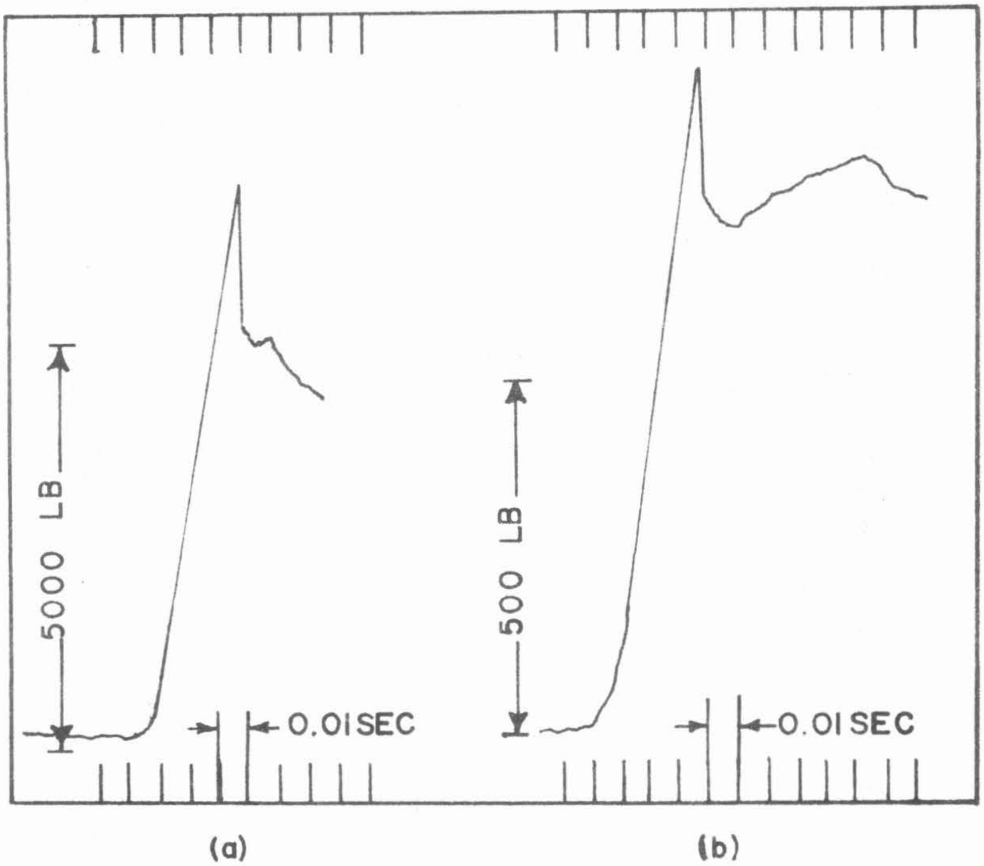

Specimen B-82	Specimen E-4
T = -111°F	T = -111°F
= 2.5×10^6 lb/in.^2sec	= 2.6×10^6 lb/in.^2sec

Fig. 8. Typical load vs. time records of unnotched specimens, ASTM grain size 8 1/4. Features similar to Fig. 7.

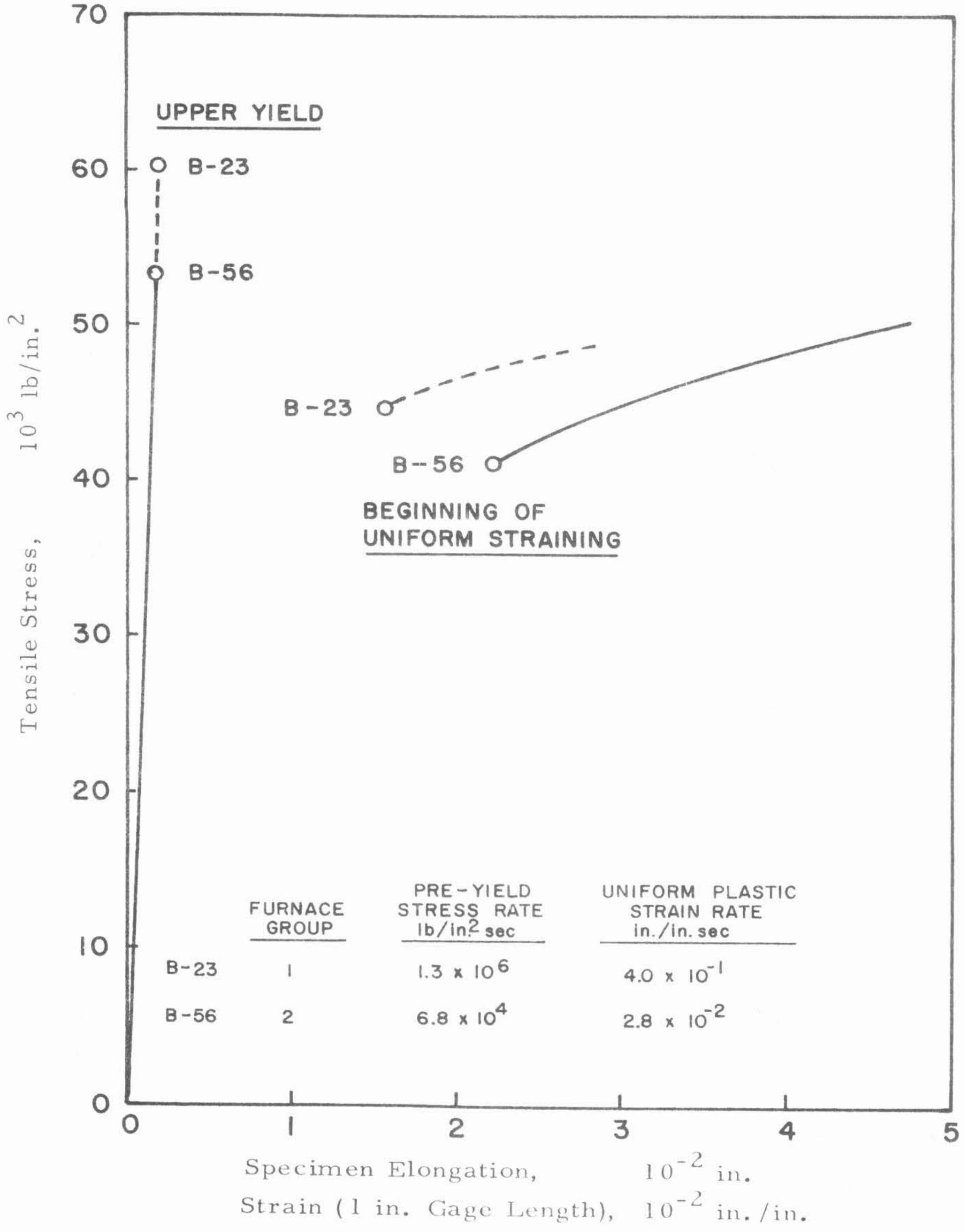

	FURNACE GROUP	PRE-YIELD STRESS RATE lb/in.^{2} sec	UNIFORM PLASTIC STRAIN RATE in./in. sec
B-23	1	1.3×10^6	4.0×10^{-1}
B-56	2	6.8×10^4	2.8×10^{-2}

Fig. 9. Approximate stress-strain curves for two large scale specimens, ASTM grain size 5 1/2. T = -21°F. Load vs. time record for B-56 shown in Fig. 7a.

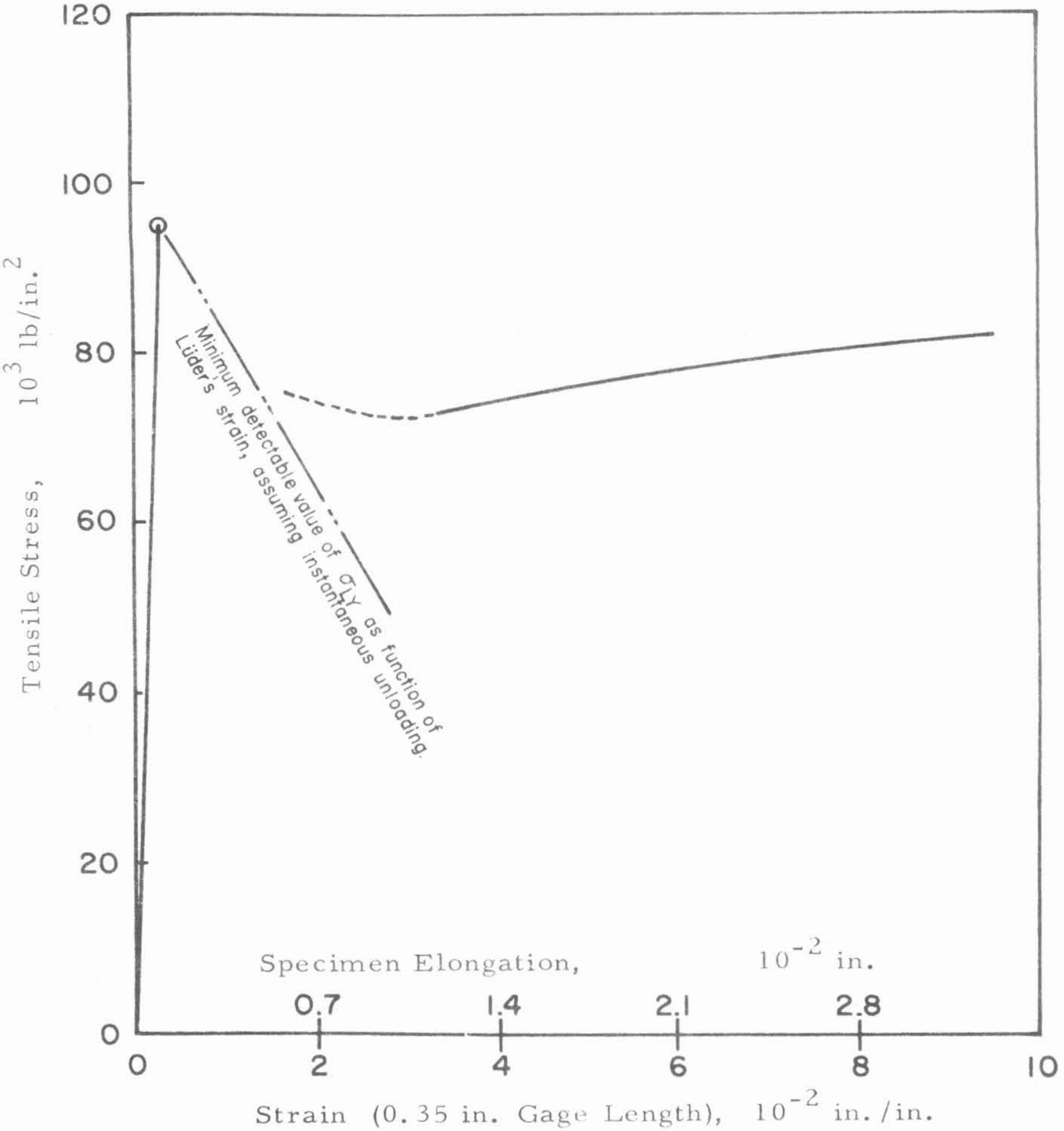

Fig. 10. Approximate stress-strain curve for small scale specimen, ASTM grain size 8 1/4. Specimen E-4. Load vs. time record shown in Fig. 8b. Strain rate during uniform yielding = 1.4 in./in. sec.

Figs. 9 and 10 are subject to fairly large errors (order of 20 percent or more) due to uncertainties in the stiffness of the hydraulic portion of the load system. The Lüder's strain for the test conditions of Fig. 9 will be taken to be 0.018 in./in. for the specimens from furnace group No. 2. The curves in Fig. 9 are shown only where the plastic strain is continuous throughout the gage length. The point at which continuous plastic straining starts in Fig. 10 is not known.

The upper and lower yield stresses of the ASTM grain size No. 5 1/2 steel are shown in Figs. 11 and 12, respectively, as a function of the pre-yield, elastic stress rate for each of the test temperatures. Logarithmic scales are used for the test rate since the yield stresses vary approximately linearly with this function. The pre-yield stress rate of the tensile tests is also shown along the abscissa in Fig. 12 to correlate the lower yield stress shown in Fig. 12 with the upper yield stress shown in Fig. 11 for the same specimen. The specimen <u>elongation</u> rate during Lüder's strain propagation is a physically more significant index of the test rate at the lower yield stress and is shown on the abscissa of Fig. 12. All of the data points marked by solid symbols were obtained from specimens annealed in one group (furnace group No. 1). The open symbols represent data from a second group of specimens. The higher values of the yield stresses obtained from the second group of specimens hardly appear significant in Figs. 11 and 12. However, nominal fracture stress data (see Fig. 18) also showed two groupings, depending upon the annealing group, and the Lüder's strains calculated for one specimen from each group are appreciably different (see

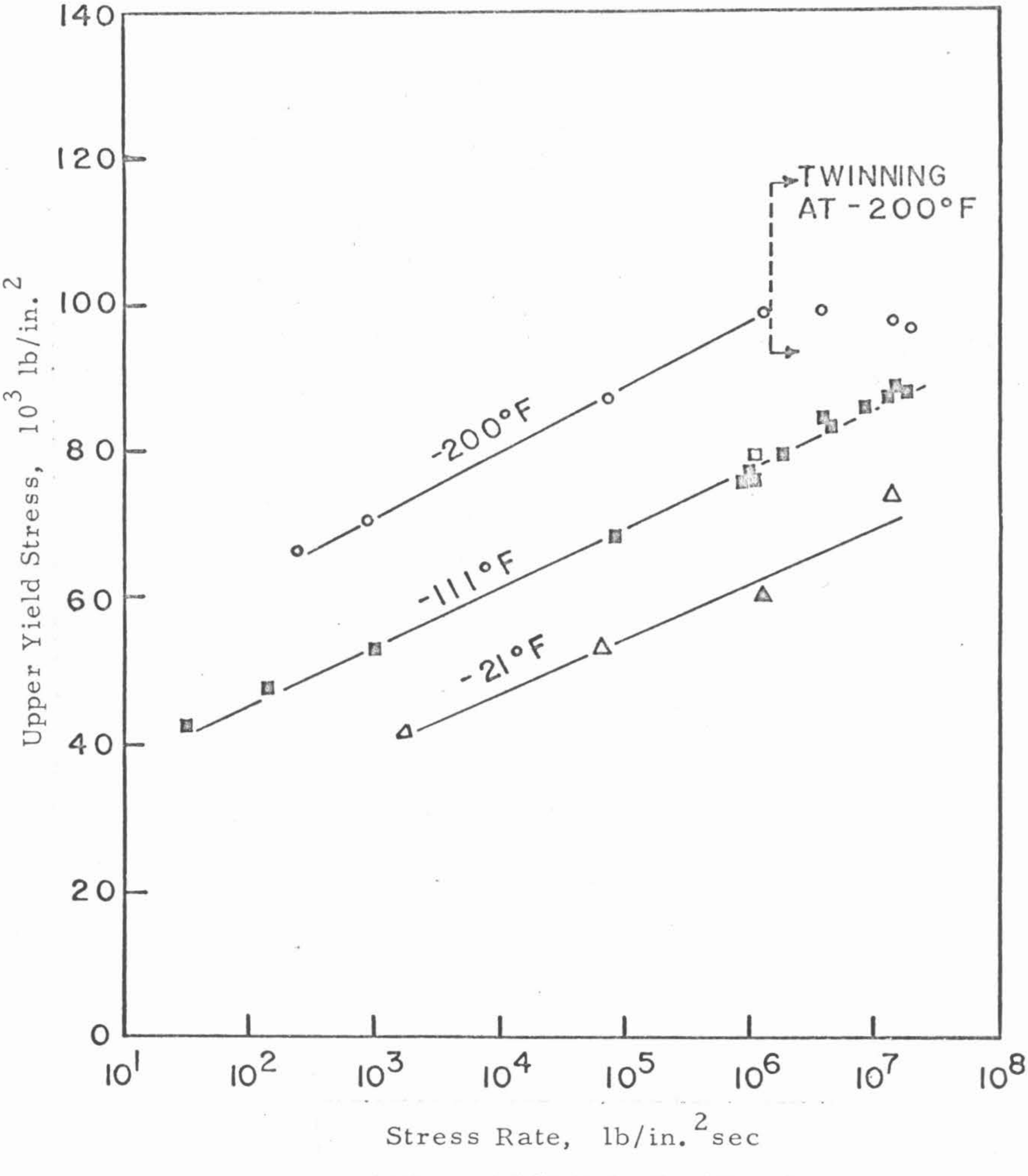

Fig. 11. Upper yield stress vs. stress rate for specimens of ASTM grain size 5-1/2.

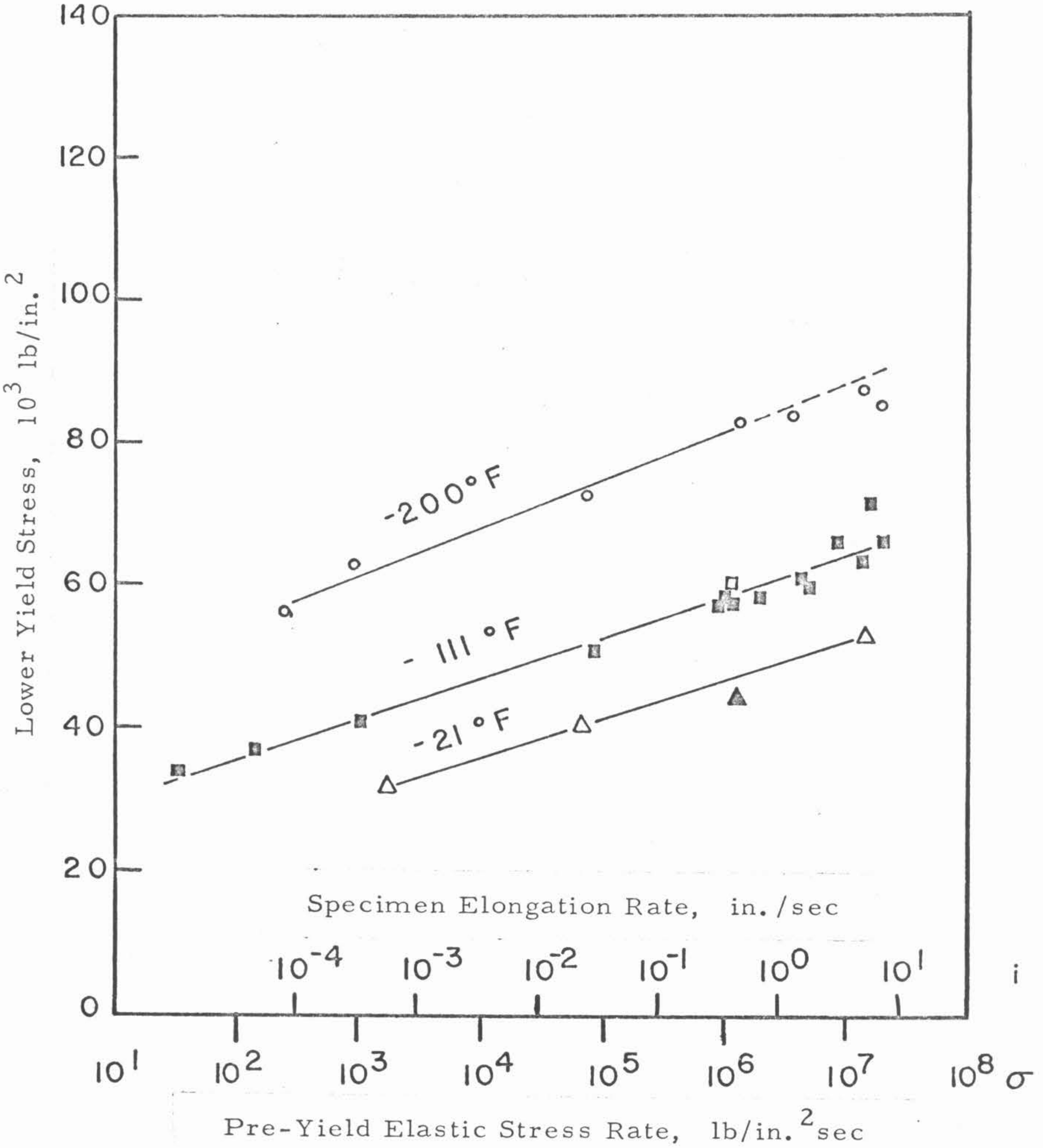

Fig. 12. Lower yield stress vs. elongation rate for specimens of ASTM grain size 5-1/2.

Fig. 9). These observations suggest that the mechanical properties of the two groups of specimens are slightly different.

The specimen which was tested at -200°F at 2×10^7 lb/in.^{2}sec (see Fig. 11) was examined metallographically. Twins were found in many of the grains, as shown in Fig. 13. Inspection of the upper yield stress data of Fig. 11 led to the conclusion that twinning causes the onset of plastic deformation at the upper yield stress in this large grain size steel at -200°F at stress rates above about 1.5×10^6 lb/in.^{2}sec , as indicated in Fig. 11. Subsequent plastic deformation at the lower yield stress may occur by slip or twinning, depending upon the specimen elongation rate. Examination of the trend of lower yield stress values in Fig. 12 suggests that plastic straining at the lower yield stress was caused by slip in all of the specimens tested at -200°F, with the possible exception of the one tested at the highest elongation rate. The twins shown in Fig. 13 appear to represent microstrain, which may slightly alter the stress-strain characteristics at the lower yield stress.

The upper and lower yield stresses of the small grain size specimens tested at -111°F are shown in Fig. 14 as a function of the test rate (logarithmic scale). The top curve is a least-squares, linear fit of the upper yield stress data and is plotted against the logarithm of the stress rate. The scale of elongation rate applies to the bottom curve, the lower yield stress. The results of one test at -21°F and one test at -200°F are also shown in Fig. 14. The value shown for the lower yield stress at -200°F is an upper limit; the testing machine stroke reached its limit before a constant load indicative of the lower

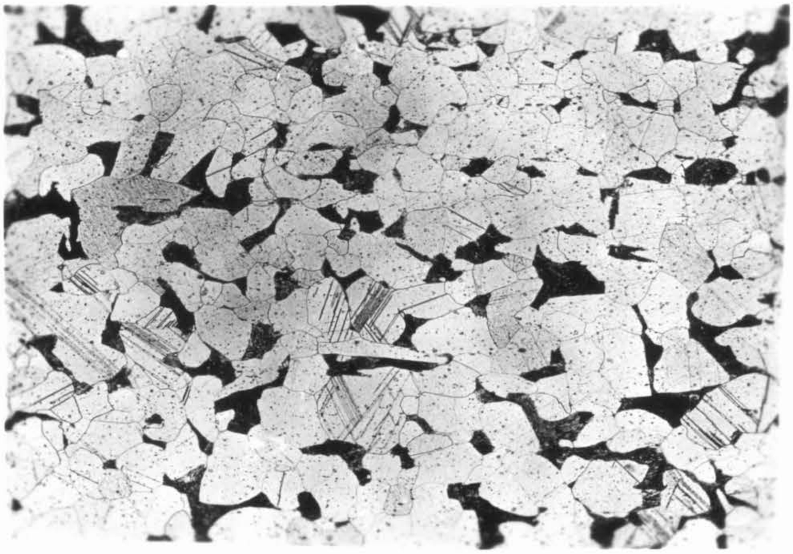

Fig. 13. Photomicrograph showing twinning in unnotched specimen of ASTM grain size 5 1/2 loaded at rate of 2 x 10^7 lb/in.^{2} at -200°F. Etch: 4% HNO_3 in Amyl alcohol. 75X.

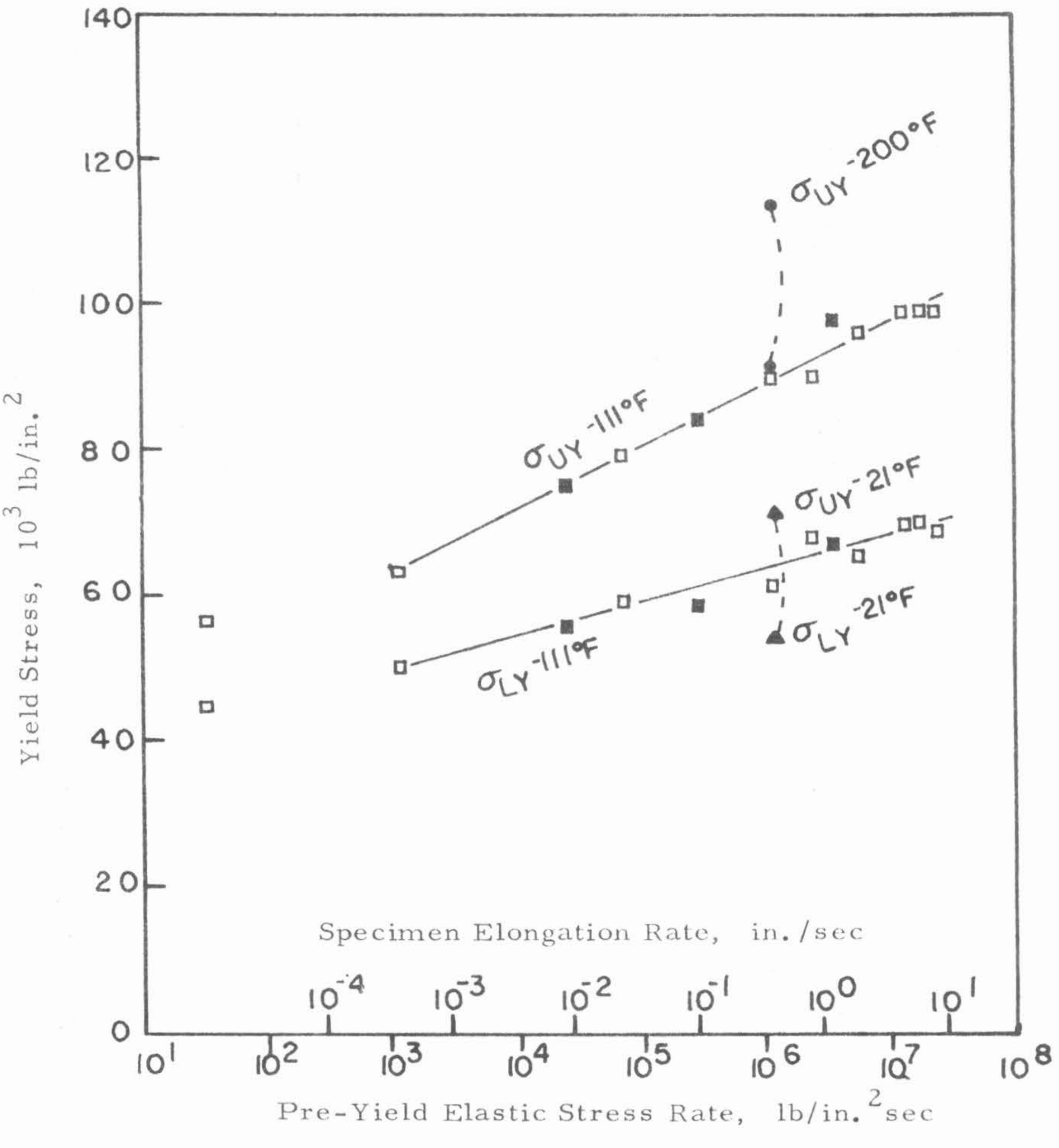

Fig. 14. Upper and lower yield stresses vs. test rate for specimens of ASTM grain size 8-1/4.

yield stress could be established. The open and the solid symbols denote two different furnace batches. The yield behavior of these two groups of specimens appears to be the same.

Three pairs of large scale, series B, and small scale, series E, unnotched specimens of ASTM G.S. No. 8 1/4 were tested to check the two specimen grip systems and dynamometer systems against each other and also to see if there might be a specimen size effect on the yield behavior of the steel. The results of these three sets of tests, two at -111°F and one at room temperature (73°F), are shown in Fig. 15. The data trend curves of Fig. 14 are included for comparison at -111°F. Similarity of the upper yield stress values for the two specimen sizes implies that the upper yield stress is not sensitive to specimen size within the range investigated here.

The lower yield stress values of the small scale specimens in Fig. 15 are shifted toward lower specimen elongation rates by a factor of 0.54 relative to the large specimens tested at the same pre-yield elastic stress rate. This shift is a result of the stiffer spring constant (in terms of nominal stress on the specimen per loading-piston displacement) of the testing machine for tests on small specimens. The apparent lower yield stress of the small scale specimens is substantially higher than for the large specimens. Part of the difference may arise because the Lüder's strain has swept entirely through the gage section of the small specimens before the nominal stress has been relaxed to the value of the lower yield stress. The oscillograph record of one of the small scale specimens, see Fig. 8b, does not show a constant load plateau which can definitely be

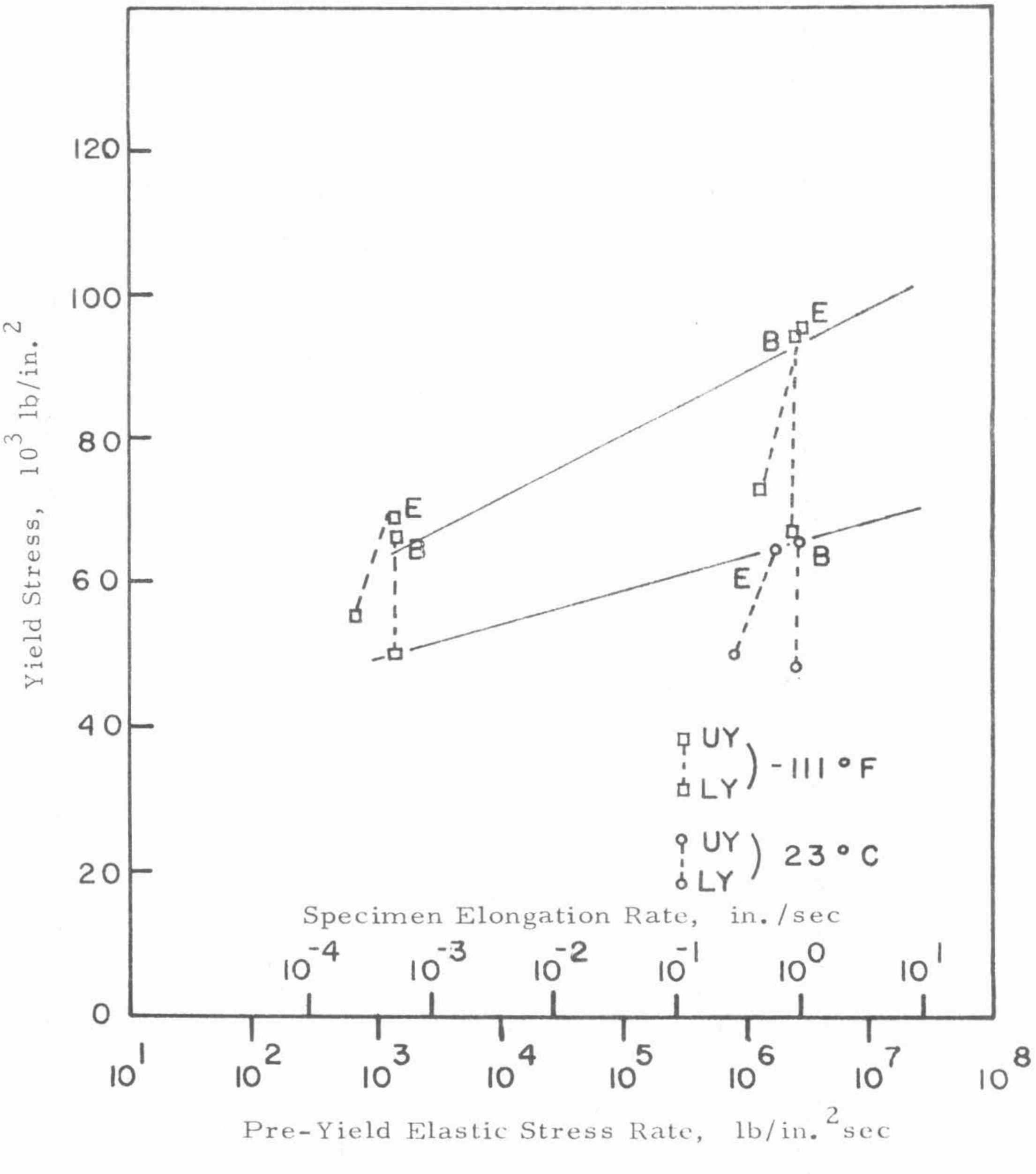

Fig. 15. Upper and lower yield stresses vs. test rate for large (series B) and small (series E) scale specimens.

identified as the lower yield stress. The stress-strain curve for this same specimen, see Fig. 10, shows how the lower yield stress can be obscured if the dimensions of the specimens and the machine stiffness do not have appropriate values with respect to the stress drop from the upper to the lower yield stress and the value of the Lüder's strain. The straight line sloping down from the upper yield stress in Fig. 10 is the locus of minimum values of the lower yield stress which could be detected for various amounts of Lüder's strain under instantaneous unloading to the lower yield stress. The Lüder's strain is probably between 0.01 and 0.02 for this material, so the capacity for unloading to the lower yield point is marginal in these specimens.

The machine and specimen characteristics are such that a Lüder's strain of 0.01 propagating entirely through the gage length can permit the nominal stress on a large scale specimen to drop by 28,000 lb/in.^{2}, in contrast to only 18,000 lb/in.^{2} on a small scale specimen. Examination of the oscillograph records and reference to the machine stiffness leads to the conclusion that the lower yield stress reported for the large scale specimens (both grain sizes) reasonably well depicts the true lower yield stress for specimens of this cross section, and at least represents an upper limit to the true value. The values of the "lower yield" stress shown in Fig. 15 for the small scale specimens may be higher than the true values partly because of the test conditions. However, there may still be a specimen diameter size effect. Tests on small diameter specimens with twice the gage length in this testing machine should resolve this question. Such tests were not made.

The upper yield stress of the two grain sizes used in this investigation of this steel as used in previous fracture studies (27) is shown at -111°F and -200°F in Fig. 16. The grain size of this steel as used in the previous studies has been determined recently to be about ASTM G.S. No. 8, instead of 6.5 as reported earlier. The data are displayed to aid in estimating the upper yield stress of the present small grain size steel, ASTM G.S. No. 8 1/4, at -200°F since only one test has been made at this temperature. The difference between the upper yield stress of the ASTM G.S. No. 8 1/4, represented by the dashed line, and the ASTM G.S. No. 8 steels at -200°F is assumed to equal the difference for these grain sizes at -111°F. Comparison of the upper yield stress values for the steels of ASTM G.S. Nos. 5 1/2 and 8 at these two temperatures indicates that the above assumption is not likely to lead to an error of more than 1,000 lb/in.^{2} in the ASTM G.S. No. 8 1/4 curve at -200°F.

The lower yield stress of the ASTM grain size No. 8 1/4 steel at -200°F has been estimated from the lower yield stress data obtained from the small grain size specimens tested at -111°F and the large grain size specimens tested at -111°F and -200°F. Two assumptions were used in the construction of the curve for the ASTM G.S. No. 8 1/4 steel at -200°F. The first assumption is that the lower yield stress is a linear function of the logarithm of the specimen elongation rate and that the slope is independent of temperature and grain size when the value of the lower yield stress exceeds the value of the "static" lower yield stress by a sufficient amount (about 20,000 lb/in.^{2}). Rosenfield and Hahn (43) have noticed that the lower yield stress of several mild steels varies linearly with the strain rate, which is in agreement with

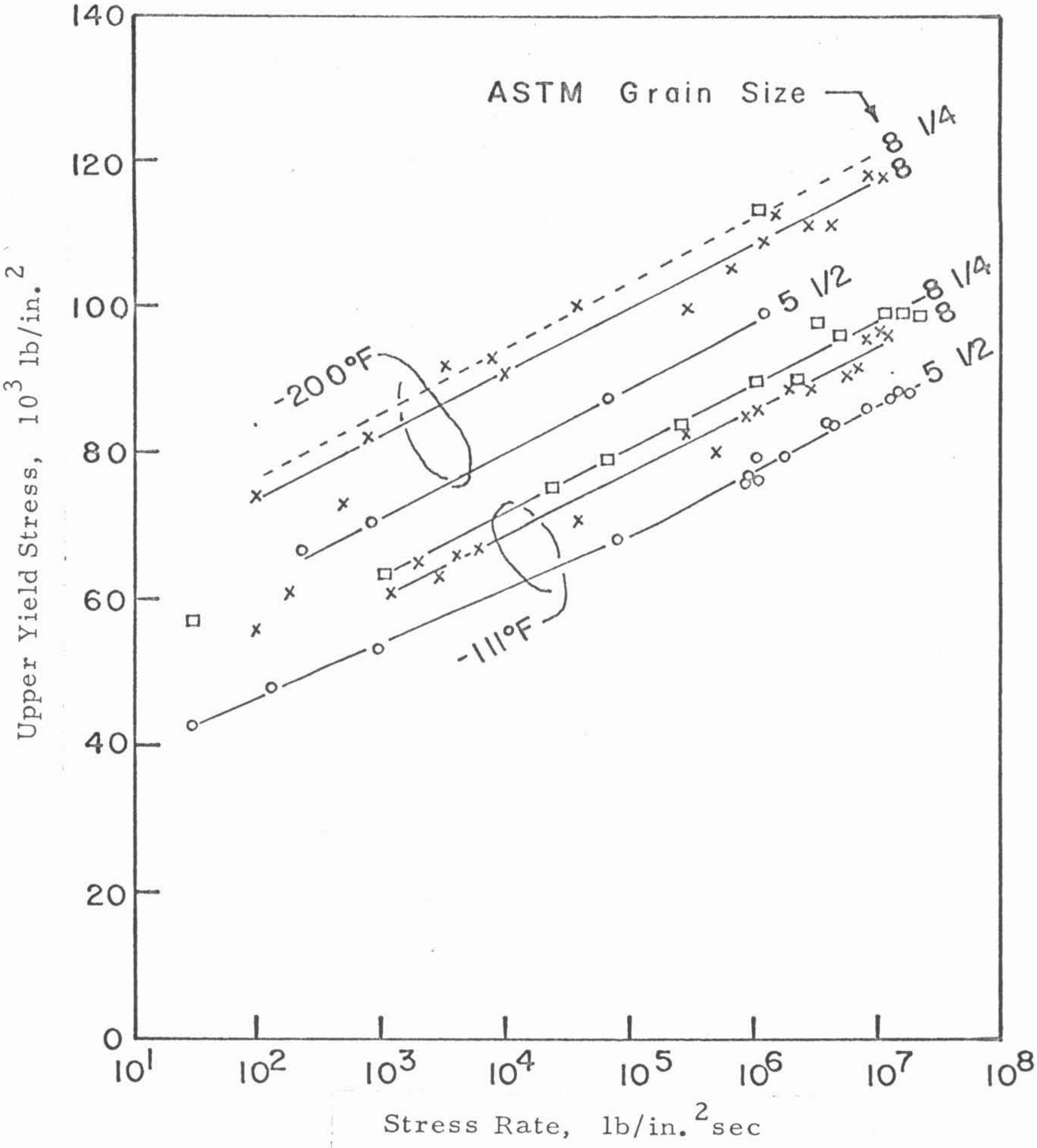

Fig. 16. Estimated value of upper yield stress for material of ASTM grain size 8-1/4 at -200°F (dashed line). Data upon which estimate is based are also shown.

this assumption. The slope of the curves of the lower yield stress vs. the logarithm of the specimen elongation rate has been determined from the data for the ASTM G. S. No. 5 1/2 steel at -200°F. Portions of the yield data for both grain sizes at -111°F have been fitted with curves of this slope, as shown by the solid lines in Fig. 17.

The second assumption is that the strengthening effect arising from the grain size is the same at -200°F as at -111°F. Thus the difference in the lower yield stress values for the steel in the small and the large grain size conditions at -200°F was assumed to be the same as at -111°F. Kazinczy, Backofen and Kapadia (44) have observed that k_y in the Hall-Petch lower yield stress expression $\sigma_{LY} = \sigma_i + k_y d^{-\frac{1}{2}}$ (where d is the grain diameter) is independent of the temperature in the range 90 to 300°K (-300 to +80°F). Their observations support this second assumption. Petch (44), however, expressed surprise that an increase in k_y had not been observed at the lower temperatures by Kazinczy et al. since others had observed such an increase in k_y. The dashed curve of Fig. 17 has been constructed with the aid of these two assumptions and will be taken as the lower yield stress behavior of the ASTM G.S. No. 8 1/4 steel at -200°F for the purposes of this thesis.

4.2 Fracture Stress Data from Notched Specimens

Fracture data for the notched specimens were obtained from oscillograph records of load vs. time taken during the fracture test. Figure 18 shows a typical load-time record of a fracture test. The sharp drop in load marks the fracture event. A calibration curve is

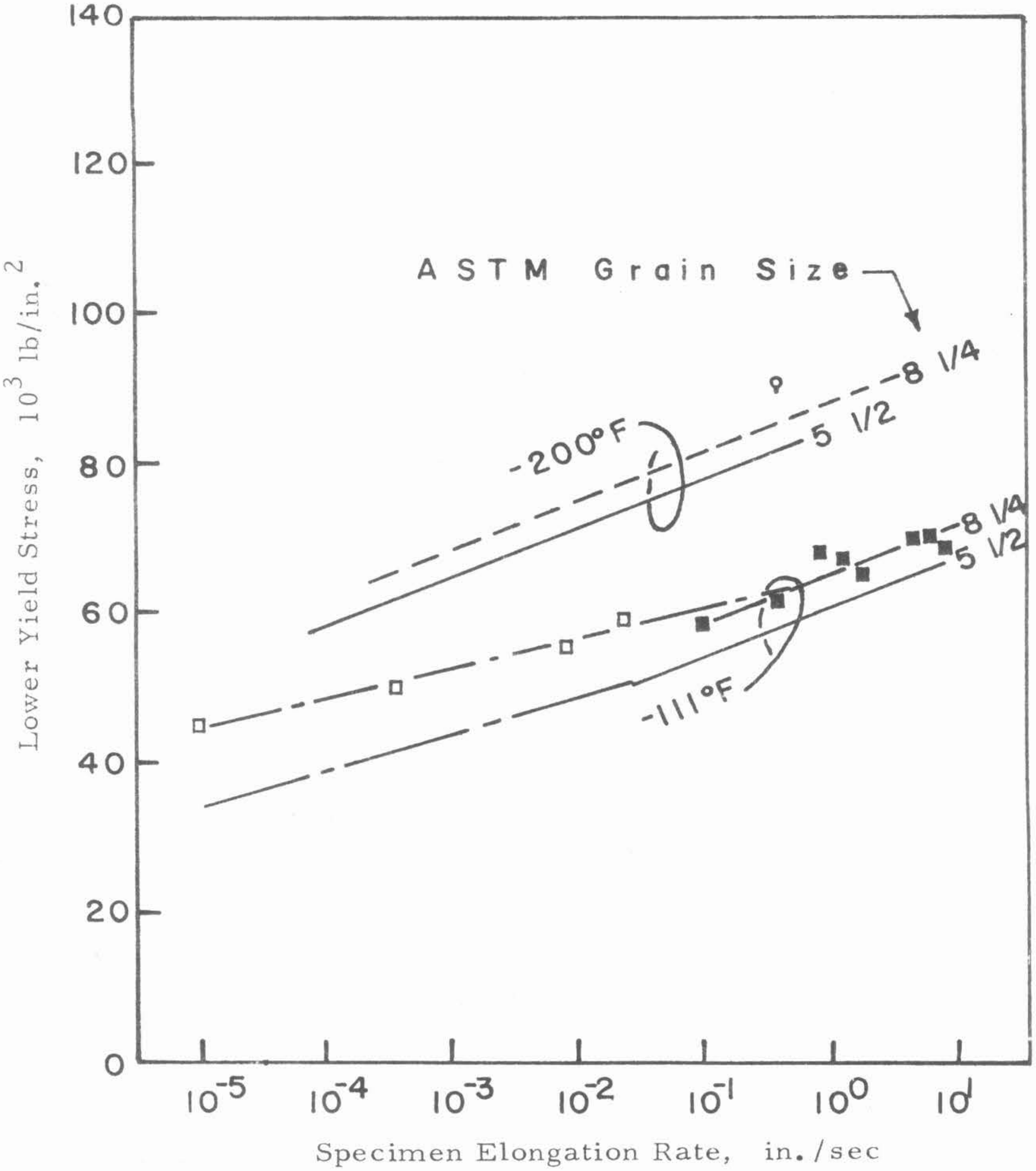

Fig. 17. Estimated value of lower yield stress for steel of ASTM grain size 8 1/4 at -200°F.

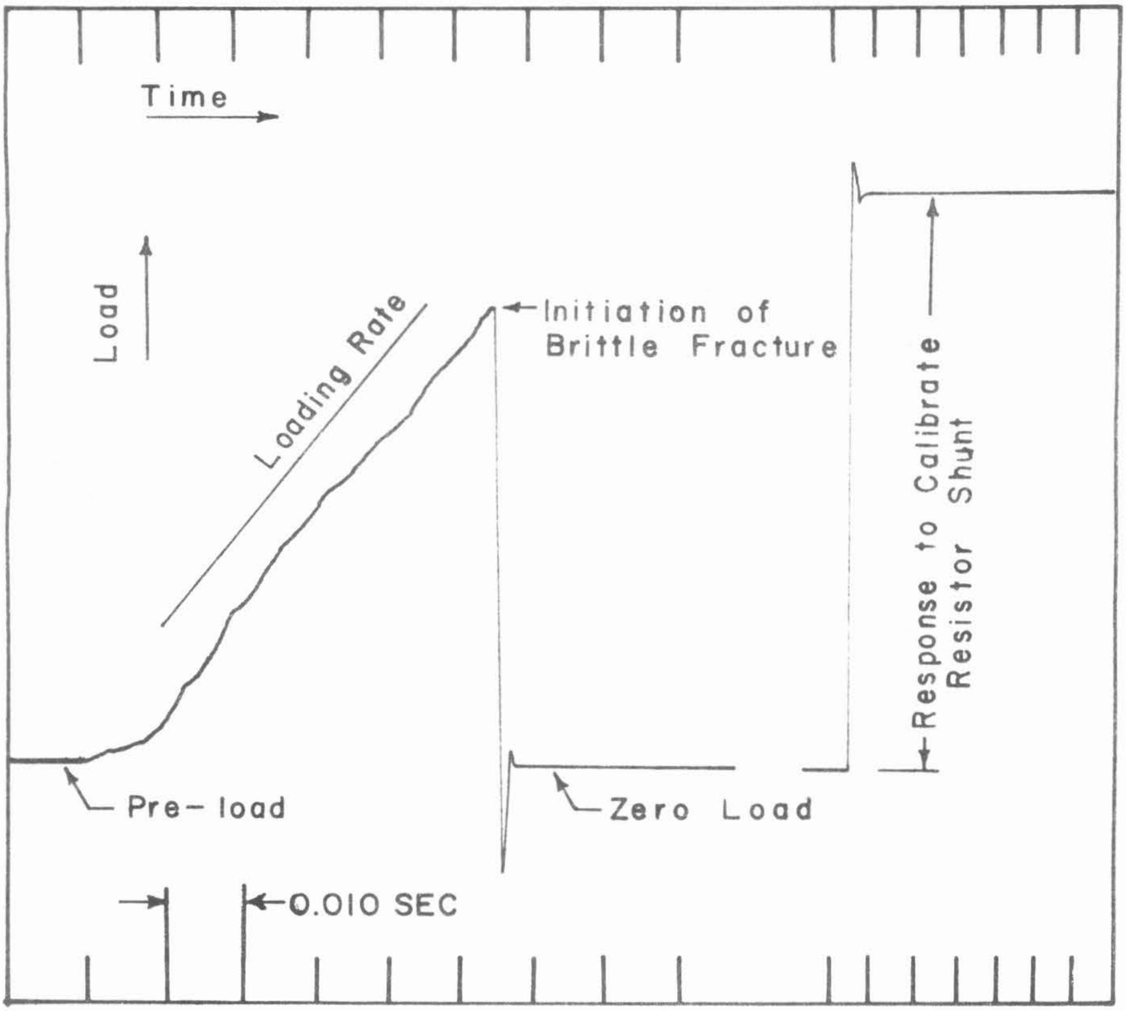

Fig. 18. Typical load vs. time record of fracture test on notched specimen.

also shown to illustrate the galvanometer response rate to a step-function signal input. The values of the nominal fracture stress (maximum tensile load supported by the specimen just prior to failure by fracture, divided by the minimum cross sectional area at the notch section) and the nominal test rate obtained from each test record are listed in Table 1. (Table 1 also contains other calculated values, which will be explained in Chapter VI.)

The nominal fracture stress of the large grain size specimens is plotted against the nominal stress rate (logarithmic scale) in Fig. 19. The open symbols denote the same furnace batch (No. 2) of specimens whose yield stress values are also shown by open symbols in Figs. 11 and 12. The nominal fracture stress values of the specimens of furnace group 1 were consistently higher than for group 2 at -111°F. The yield behavior was the opposite (see Figs. 11 and 12). Thus the mechanical properties of the two furnace batches are slightly different. The X's show the maximum stress level to which the unfractured notched specimens, A-7, A-31 and A-39, were subjected prior to a metallographic search for microcracks and represent lower limits for the nominal fracture stress values for these three specimens. These specimens were from the same furnace group as those fractured specimens depicted by the open symbols. Thus two of the unfractured specimens were loaded to a higher nominal stress level than two others which had fractured.

Figure 20 shows the nominal fracture stress of the small grain size specimens as a function of the nominal stress rate (logarithmic scale). The fracture data of Hendrickson et al. (27) from a

TABLE 1. Nominal and Local Fracture Stress Data

Specimen No.	Notch fidelity, ρ/ρ_{ideal}	Annealing group	Nominal stress rate, lb/in.^{2}sec	Nominal fracture stress, σ_{nomf}, 10^3lb/in.^{2}	Yield stress, σ_{yd}, 10^3lb/in.^{2}	$\sigma_{nomf}/\sigma_{yd}$	Maximum tensile stress at fracture[1] 10^3lb/in.^{2}	Depth of plastic enclave, 10^{-3}in.
ASTM G. S. No. $5\frac{1}{2}$, -200°F								
A-72	0.70	2	2.1×10^7	65.8	79	0.833	124-128	9.8
A-16	0.85		1.5×10^6	79.1	71.6	1.104	125-130	16
A-35	0.98		8.6×10^4	88.8	63.4	1.40	121-126	29
A-17	0.88		1.1×10^3	101.7	(52)[2]	1.95[2]		
A-46	0.90	↓	1.7×10^2	97.7	(47.5)	2.06		
ASTM G. S. No. $5\frac{1}{2}$, -111°F								
A-30	0.94	2	1.1×10^7	96.7	54	1.79	113-117	59
A-37	0.86		2.7×10^6	94.6	51	1.85		
A-7	0.89		2.6×10^6	>96.3 N.F.	51	1.89		
A-31	0.96		2.4×10^6	>82.5 N.F.	51	1.62	103-107	43
A-39	0.90		2.3×10^6	>95.4 N.F.	51	1.87		
A-24	0.87	↓	2.3×10^6	93.3	51	1.83		
A-5	0.95	1	2×10^7	105.9	55.5	1.91		
A-10	~0.79		5.6×10^6	101.7	52.6	1.93		
01	~1.19		2.1×10^6	109.0	51.0	2.13		
PA	~0.65		9×10^5	106.9	49.0	2.18		
A-65	~0.92		8.8×10^5	101.0	49.0	2.06		
A-62	1.12	↓	4×10^4	104.8	42.0	2.49		
ASTM G. S. No. $5\frac{1}{2}$, -23°F								
A-38	0.99	2	1.9×10^7	105.3	44.5	2.36		
A-29	0.97	↓	8.8×10^5	103.0	38.4	2.68		

---

[1] The two values pertain to the predictions of the two curves of σ_{max}/σ_{yd} in Fig. 33.

TABLE 1. Nominal and Local Fracture Stress Data

(cont'd.)

Specimen No.	Notch fidelity, ρ/ρ_{ideal}	Annealing group	Nominal stress rate, lb/in.^{2}sec	Nominal fracture stress, σ_{nomf}, 10^3lb/in.^{2}	Yield stress, σ_{yd}, 10^3lb/in.^{2}	$\sigma_{nomf}/\sigma_{yd}$	Maximum tensile stress at fracture[1], 10^3lb/in.^{2}	Depth of plastic enclave, 10^{-3}in.	Tensile stress 0.0111 in. from plastic wedge tip toward notch root, 10^3lb/in.^{2}
ASTM G. S. No. $8\frac{1}{4}$, -200°F									
A-84	0.967	4	1.5×10^6	93.8	75.0	1.25	137-142	21.8	121.5
A-85	0.831	↓	2.5×10^3	101.0	(57.5)[2]	1.75	120-124	55.8	119
D-5	1.016	4	8.3×10^6	119.7	77.3	1.55	154-159	14.2	119
D-4	1.029	│	3.8×10^6	105.8	75.1	1.41	143-149	11.1	75.1
D-6	0.935	│	1.4×10^6	115.9	72.2	1.605	145-151	15.9	121.5
D-12	0.964	│	3.2×10^5	137.8	68.2	[2.02[2]			
D-7	1.005	│	2.8×10^4	141.3	57.4	2.46			
D-11	1.016	│	1.25×10^3	133.7	(49.4)	2.71			
D-3	1.051	↓	2.1×10^2	126.4	(45.4)	2.78]			
ASTM G. S. No. $8\frac{1}{4}$, -111°F									
A-25	~0.89	3	2.04×10^7	90.26	62.5	1.44	121-125	30.3	114
A-33	~0.84	│	9.1×10^6	99.48	60.8	1.636	123-128	44.0	121
A-3	~0.89	↓	5.5×10^6	98.1	60.0	1.636	121-126	44.0	119.5
A-83	1.02	4	4.4×10^6	97.0	59.8	1.62	121-126	42.5	118
A-45	~0.89	3	4.0×10^6	94.9	59.6	1.59	119-123	40.0	116.5
A-36	0.89	│	2.7×10^6	128.4	58.5	[2.19]			
A-69	0.89	│	1.8×10^6	99.5	57.9	1.72	120-124	52.5	119
A-8	~0.89	↓	1.5×10^6	129.8	57.4	[2.26			
A-81	0.93	4	1.3×10^6	132.0	57.0	2.32			
A-4	~0.79	3	8×10^5	131.6	56.0	2.35]			

---

[2] Parenthesis mean yield stress data were extrapolated; brackets mean stress analysis not applicable.

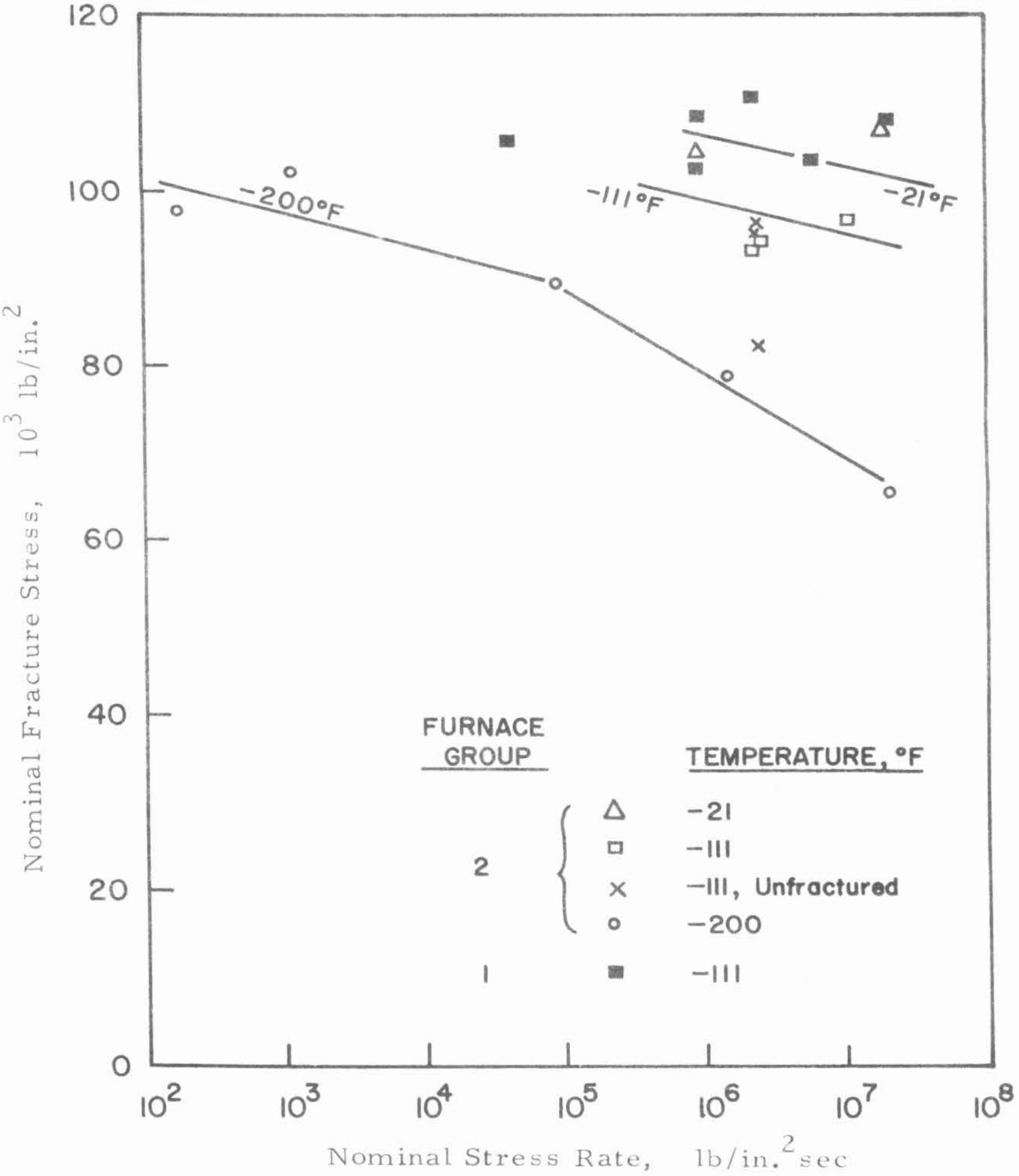

Fig. 19. Nominal fracture stress vs. nominal stress rate for notched specimens of ASTM grain size 5 1/2. The data trend curves for the specimens from furnace group no. 2 were determined from a plot of σ_{nomf} vs. σ_{yd}, where σ_{yd} was determined from Fig. 35.

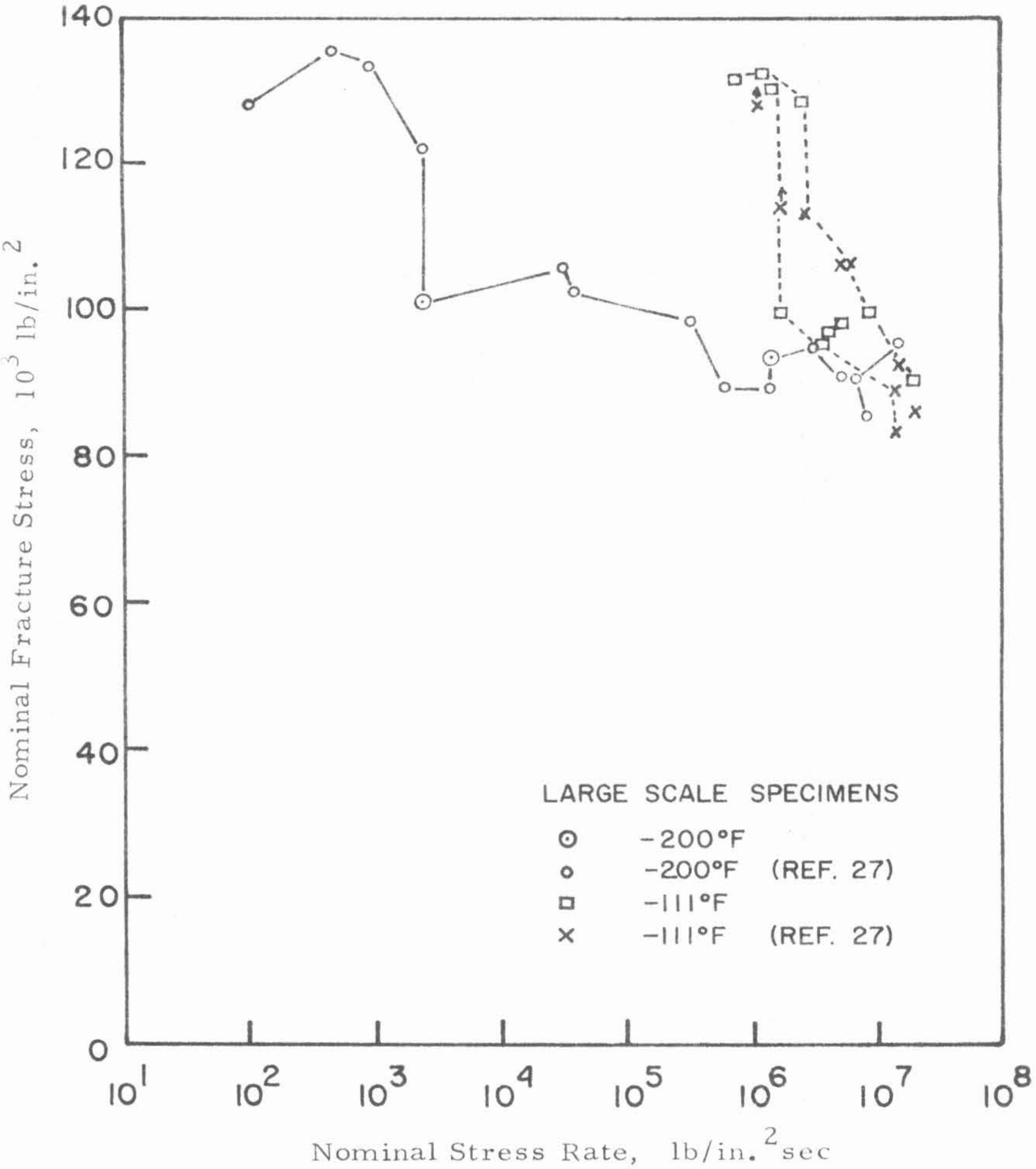

Fig. 20. Nominal fracture stress vs. nominal stress rate for notched specimens of ASTM grain size 8 1/4.

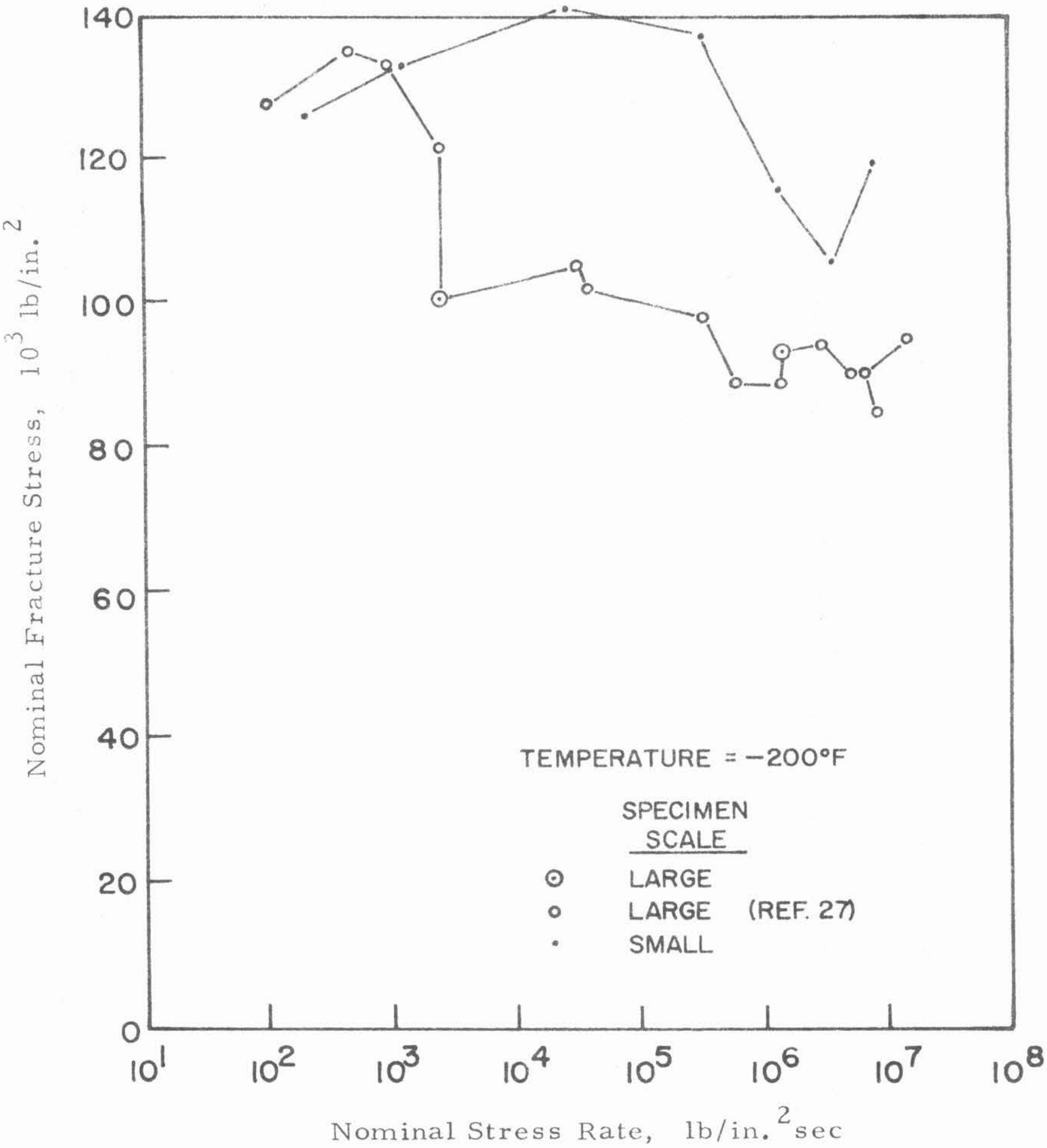

Fig. 20. (Continued)

previous study are also shown in this figure. Attention is called to three groups of fracture data. The first group consists of present and previous fracture data at -111°F (large scale specimens only) at nominal stress rates above about 10^6 lb/in.^{2}sec in Fig. 20a; the second consists of present and previous data at -200°F for large scale specimens, shown in both Figs. 19a and b for purposes of comparison; and the third consists of data from the small scale specimens of the present study at -200°F, shown in Fig. 19b.

The present fracture data at -111°F exhibits a sharp transition in the nominal fracture stress values at a nominal stress rate of about 2×10^6 lb/in.^{2}sec. The fracture data on the same steel of the previous study (but of ASTM grain size No. 8, vs. 8 1/4 for the present investigation) show a similar, though less abrupt, change in the nominal fracture stress behavior at -111°F. The coincidence of the transition in nominal fracture stress as a function of stress rate for the ASTM G.S. Nos. 8 1/4 and 8 specimens at -111°F suggests that the fracture data from both groups of specimens may be combined to deduce a fracture transition at -200°F for the large scale specimens. On this basis, the nominal fracture stress transition for the ASTM grain size No. 8 1/4, large scale notched specimens, is estimated to occur at a nominal stress rate of about 2×10^3 lb/in.^{2}sec at -200°F. The nominal fracture stress transition for the small scale specimens of this grain size at -200°F occurs at a nominal stress rate at least two orders of magnitude greater than for the large scale specimens.

The oscillograph record for one large scale specimen with the small grain size tested at -111°F is shown in Fig. 21. The specimen

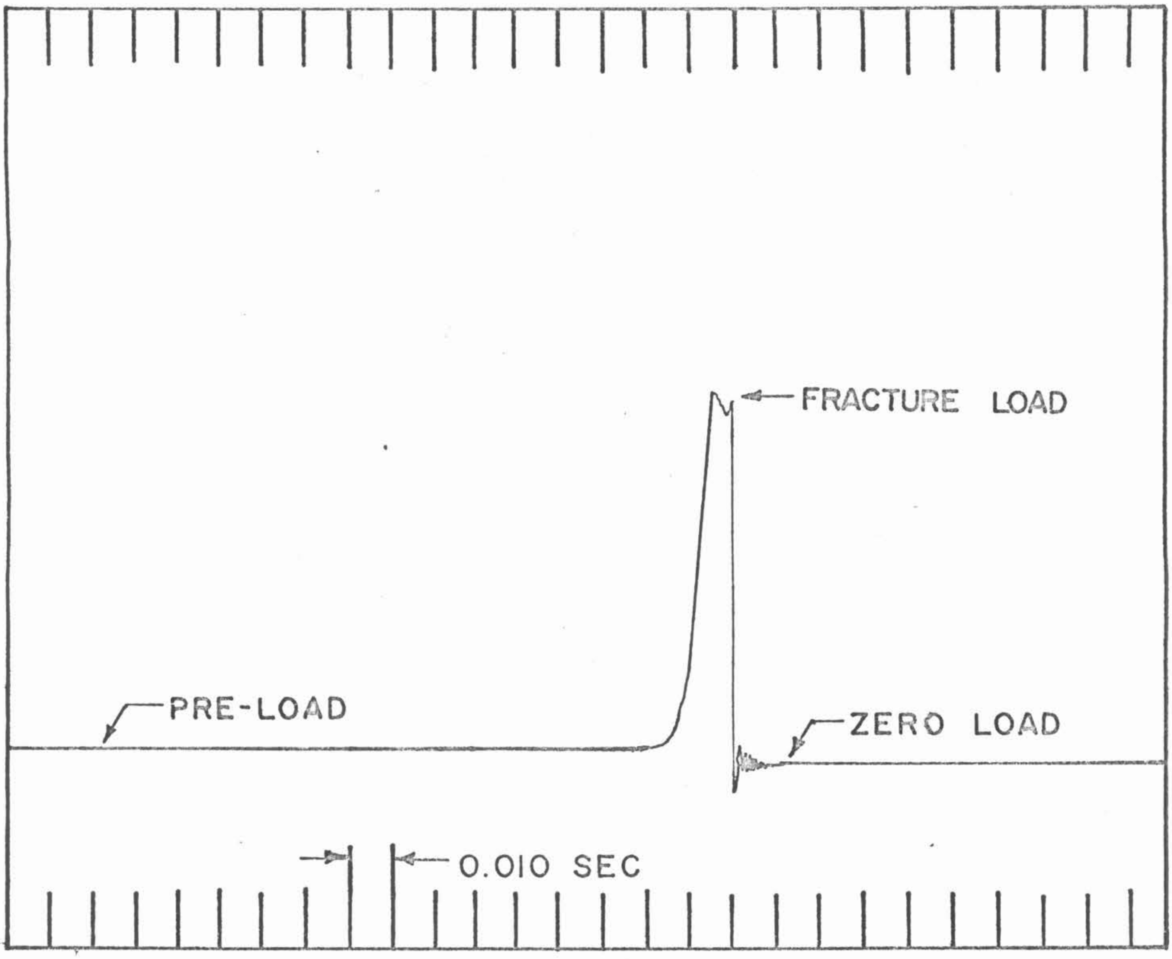

Fig. 21. Load vs. time record of fracture test in which an unloading disturbance occurred before fracture.

experienced a small amount of unloading due to a malfunction of the testing machine. After loading resumed, the specimen broke at a nominal stress level of 83,000 lb/in.^{2}, which is slightly lower than the maximum value of the stress just prior to unloading and substantially lower than the nominal fracture stress (about 90,000 to 100,000 lb/in.^{2}) of other specimens at this stress rate. This fracture record is cited to illustrate the profound effect a seemingly minor deviation in loading history (unloading of about 5,000 lb/in.^{2} nominal) may have upon the nominal fracture stress.

4.3 Microcrack Search

The maximum nominal stresses to which the notched specimens A-31, A-39, and A-7 were subjected prior to being examined for microcracks are listed in Table 2 and are indicated by the x's in Fig. 19. The calculated values of the maximum tensile stress listed in Table 2 are based on the lower yield stress data for this steel and the elastic-plastic stress analysis described in Chapter V. The other entries in Table 2 summarize the extent of the microcrack search and the results.

Figure 22 shows photomicrographs of portions of the polished and etched cylindrical sections below the notch root of specimen A-31. Approximately one-fifth of the circumference is shown. The horizontal reference line near the top of each photomicrograph is a circumferential scratch located an axial distance of about 0.012 in. from the notch root. (See Fig. 22c to aid in estimating this distance on the photomicrographs.) The notch root lies approximately over (out of the plane of the photomicrograph) the edge of cavity ① which is closest to the circumferential reference scratch. Three cavities were found

TABLE 2. Preparation of Specimens and Results of Microcrack Search.

All specimens were of ASTM grain size 5 1/2 and were loaded at a nominal rate of 2.4×10^6 lb/in.^{2}sec at -111°F.

Specimen no.	Maximum nominal stress, 10^3 lb/in.^{2}	σ_{max} 10^3 lb/in.^{2}	Plastic elongation, 10^{-3} in.		Depth of microcrack search 10^{-3} in.	Results
			Initial loading	Room temp.		
A-31	82.5	105	5-10 (est.)	5	19	One cavity opened to free surface at notch root. Two more cavities located in depth interval 0.003 to 0.016 in. below notch root. See Fig. 22.
A-39	95.4	110*	0.2	3.3	9-16 (bent)	Microcracks were not found.
A-7	96.3	110*	3	None	13-15 (bent)	One cracked pearlite colony 0.011 in. below notch root. No other microcracks. See Fig. 23.

---

* Calculated for $\sigma_{nom}/\sigma_{yd} = 1.75$.

(a) 0.0029 in. below notch surface 36.3×

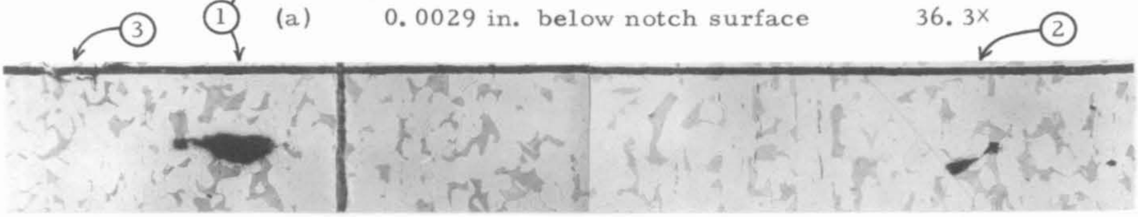

(b) 0.0066 in. below notch surface 37.3×

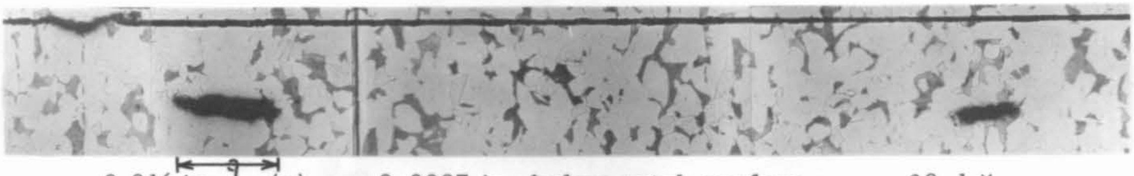

(c) 0.0097 in. below notch surface 38.1×

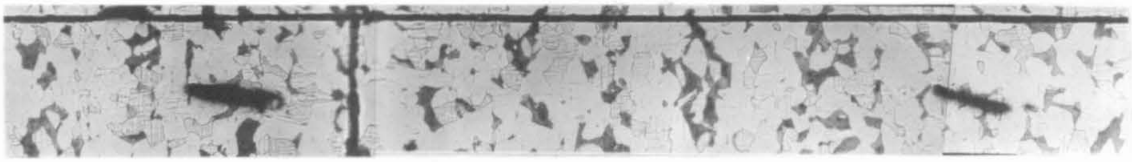

(d) 0.0128 in. below notch surface 39.0×

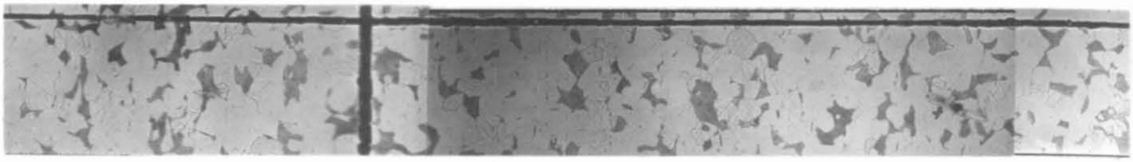

(e) 0.0155 in. below notch surface 39.9×

Fig. 22. Photomicrographs of successive cylindrical sections under notch root showing voids. (Multiply listed magnifications by 0.85.)

in the notch section of this specimen. One cavity opened to the surface of the notch root; the other two cavities lay deeper than 0.003 in. below the notch surface. The greatest depth of these cavities below the notch root was about 0.016 in. Examination of the next lower section at a depth of 0.0195 in. did not reveal any new voids.

Crack ② appears to be associated with a large pearlite colony. But crack ① appears to traverse significant pearlite colonies only in Figs. 22 a and d. The metallurgical structure near crack ③ is obscured by the scribed line.

Specimen A-31 had been elongated a large amount after being loaded to the maximum stress level so the voids cannot be definitely identified with microcrack formation during the initial rapid load application at -111°F. Surface markings caused by plastic deformation of the grains indicated that the cavity which opened to the notch root surface, cavity ①, did so after a moderate amount of deformation had taken place.

Examination of specimen A-39, which had been unloaded as quickly as possible after being loaded to a nominal stress of 95,400 $lb/in.^2$, failed to reveal any microcracks. The examination was carried to 0.009 to 0.016 in. below the notch surface.

The only microcrack found in the third specimen, A-7, was a cracked pearlite colony, shown in Fig. 23. This crack was observed 0.011 in. below the notch root. It did not intersect the next higher or lower examination surfaces (± 0.003 in.). This specimen had also been elongated during the original loading cycle and the time of nucleation of the microcrack with respect to attainment of the

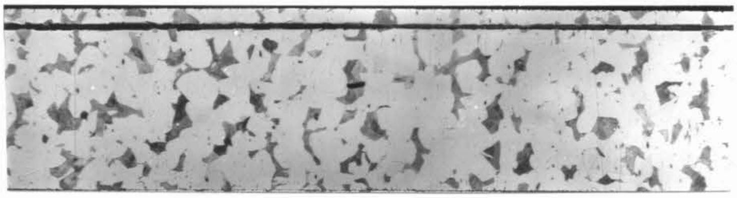

a. About 35X

b. 200X

Fig. 23. Photomicrographs of cylindrical section under notch root showing crack through pearlite colony.

maximum stress is not known.

4.4 Plastic Zones

The nominal stresses to which the three large-scale notched specimens of both grain sizes were subjected under quasi-static load conditions at room temperature prior to examination for plastically deformed material are listed in Table 3. The upper and lower yield stresses for unnotched specimens tested under the same conditions are also given. The ratios of nominal stress on the notched specimens to the upper and lower yield stresses are listed to serve as dimensionless indices of the elastic-plastic stress state. The root radii of these notches ranged from 0.0106 to 0.0114 in., slightly larger than most of the notches of the fractured specimens.

The plastic zones of the small grain size specimens, as revealed by nitriding and etching with Fry's reagent, are shown at 5.3X magnification in Fig. 24; the plastic zones of the large grain size specimens are shown in Fig. 25. Markings which are irrelevant to the plastic strain state are due to 1) iron plating around the edges, 2) staining from reagent seepage near the edges, 3) rounded corners to facilitate polishing, and 4) darkening of strained material around the hardness indentations. Banding of the pearlite is observed parallel to the tensile direction and diagonal scratches from polishing are present. The banding is less pronounced in the specimens with the larger grain size.

The examination surfaces are not quite diametral planes. This fact does not significantly alter the interpretation of the plastic wedge-

TABLE 3. Quasi-Static Loading of Notched Specimens

Specimen no.	$\dot{\sigma}_{nom}$, lb/in.^{2}sec	σ_{LY} , 10^3 lb/in.^{2}	σ_{UY} , 10^3 lb/in.^{2}	σ_{nom}, 10^3 lb/in.^{2}	σ_{nom}/σ_{LY}	σ_{nom}/σ_{UY}	Wedge depth, 10^{-3} in.	Included angle at tip of plastic wedge
ASTM Grain Size 8 1/4								
B-89	3×10^2	35.1	48.0					
B-91	4×10^1	34.1	49.1					
A-93	4×10^1	34.5	48.5	38.5	1.12	0.80	18-19	56°-60°
A-90	8×10^0	↓	↓	48.0	1.39	0.99	21-34	58°-52°
A-91	3×10^1			65.9	1.91	1.36	52-67	58°-50°
ASTM Grain Size 5 1/2								
B-93	2×10^2	34.0	40.4					
B-94	4×10^1	30.3	41.2					
A-94	6×10^1	32.0	40.8	32.1	1.00	0.78		
A-97	3×10^1	↓	↓	57.8	1.80	1.41		
A-98	3×10^1			69.5	2.17	1.70		

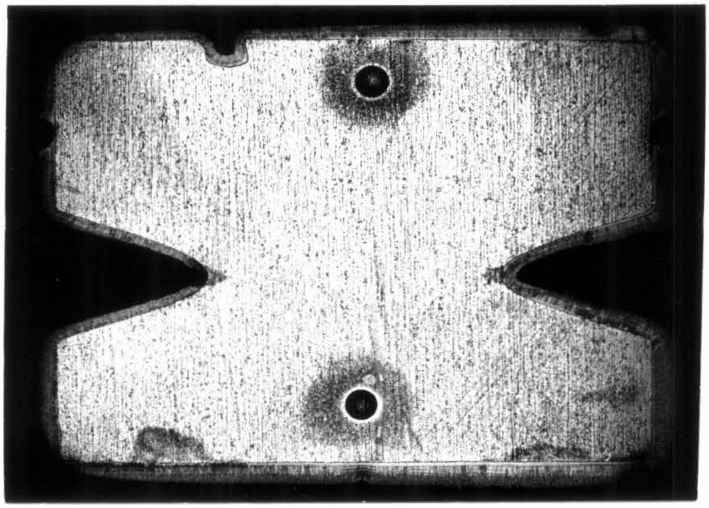

a. A-93. $\sigma_{nom}/\sigma_{LY} = 1.12$, $\sigma_{nom}/\sigma_{UY} = 0.80$

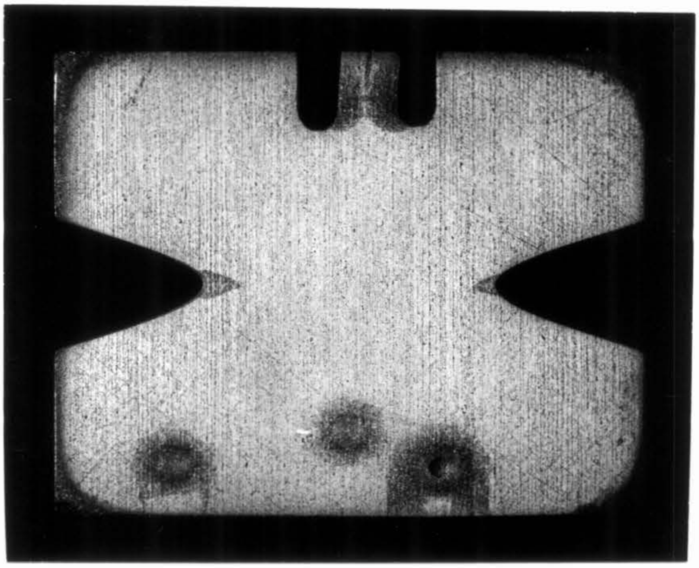

b. A-90. $\sigma_{nom}/\sigma_{LY} = 1.39$, $\sigma_{nom}/\sigma_{UY} = 0.99$

Fig. 24. Etch patterns showing plastically strained regions in notched specimens of ASTM grain size 5 1/2. Sections parallel to axis of symmetry. Static loading; tensile axis vertical. Surface nitrided, then etched with Fry's reagent. 5.3X.

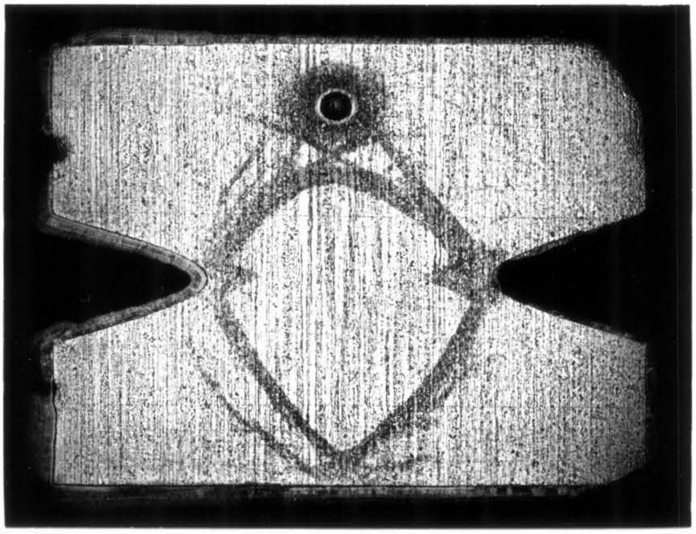

c. A-91. $\sigma_{nom}/\sigma_{LY} = 1.91$, $\sigma_{nom}/\sigma_{UY} = 1.36$

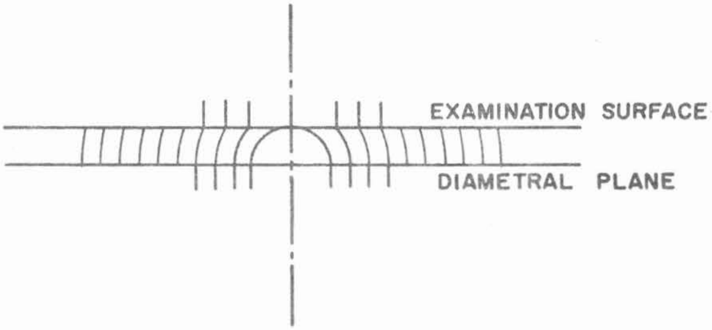

d. Horizontal scale transformer to determine the true radius vector to a point on the examination surface.

Fig. 24. (Continued.)

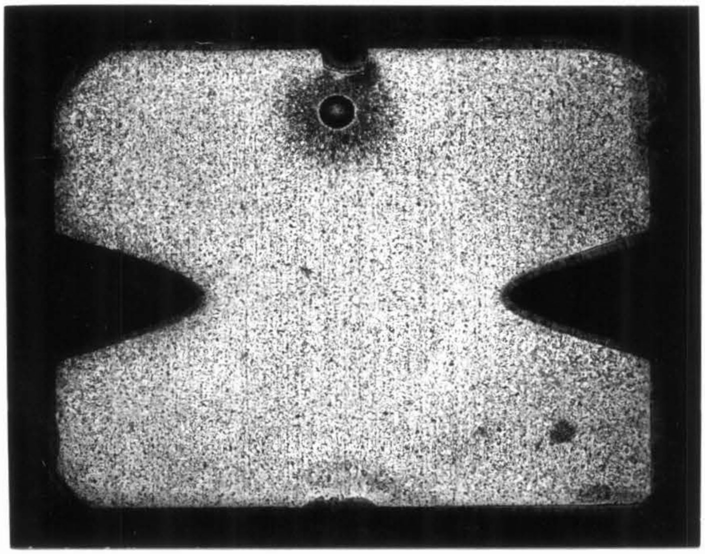

a. A-94. $\sigma_{nom}/\sigma_{LY} = 1.00$, $\sigma_{nom}/\sigma_{UY} = 0.78$

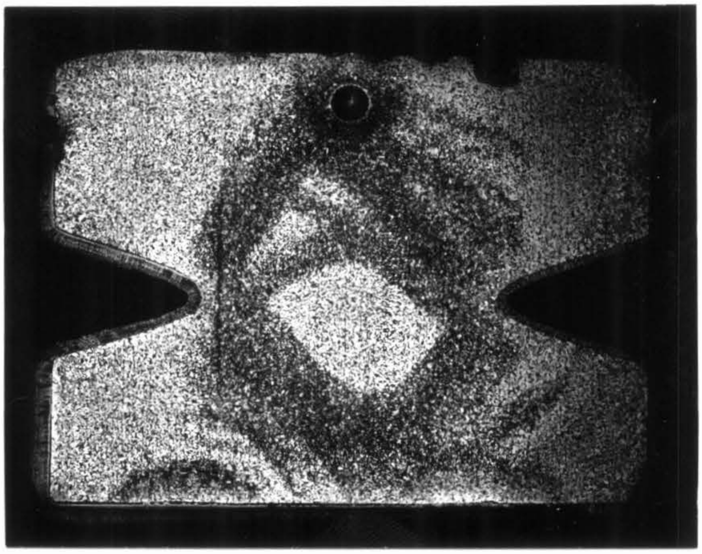

b. A-97. $\sigma_{nom}/\sigma_{LY} = 1.80$, $\sigma_{nom}/\sigma_{UY} = 1.41$

Fig. 25. Etch patterns showing plastically strained regions in notched specimens of ASTM grain size 5 1/2. Sections parallel to axis of symmetry. Static loading; tensile axis vertical. 5.3X.

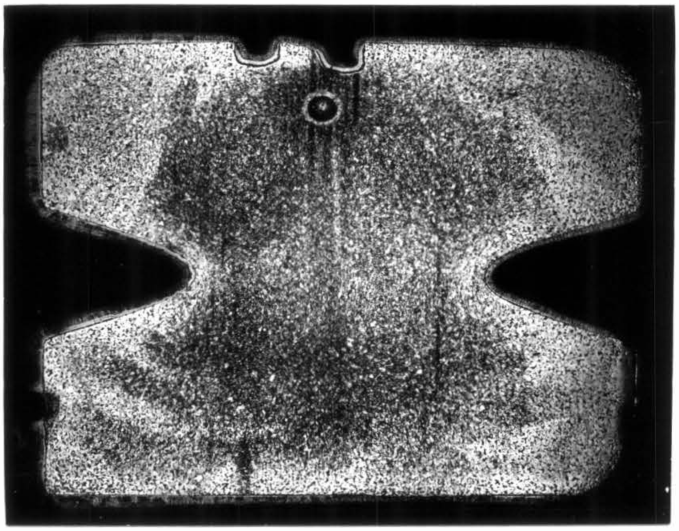

c. A-98. $\sigma_{nom}/\sigma_{LY} = 2.17$, $\sigma_{nom}/\sigma_{UY} = 1.70$

Fig. 25. (Continued.)

shaped enclaves at the notch root in Fig. 24, nor the overall strain patterns in Fig. 25. The horizontal position at which cylindrical surfaces of constant radius intersect a diametral plane and the plane of Fig. 24c is indicated by the horizontal scale transformer shown in Fig. 24d. The use of this horizontal scale transformer aids in the determination of the true radial location of the features shown in Fig. 24c.

The presence of bending moments during initial stressing is implied by the unequal sizes of the wedge-shaped plastic enclaves on the two sides of the specimens in Figs. 24b and c. The circular arcs connecting the notch roots above the minimum section in Figs. 24c and 25b and below the minimum section in Fig. 25c may also imply bending.

At low stress levels the plastic enclaves are confined to wedge-shaped regions at the root of the notch in the small grain size specimens. The boundary of the darkly etched wedge-shaped region is quite distinct, as shown in Fig. 26, which is an enlargement (35X from original) of the left-hand enclave of Fig. 24b. Some portions of the boundary definitely coincided with grain boundaries. The grains in the tip of the wedge did not etch as darkly as those closer to the root of the notch.

The shape of the plastic enclaves at low stress levels for the large grain size specimens is not known. Figures 25b and c show that the steel near the (iron plated) notch surface did not respond to the nitriding and etching treatment. Thus the absence of dark regions near the notch in Fig. 25a merely limits the size of the plastic

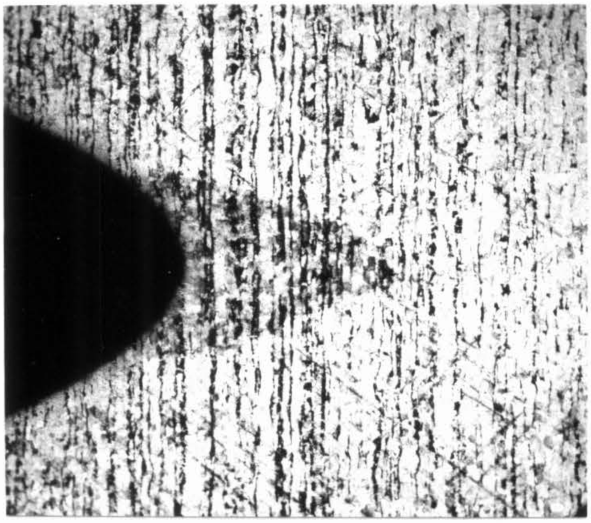

Fig. 26. Photomicrograph of plastic enclave at notch root shown on left side of specimen A-90, Fig. 24b. 35X.

enclave to the region within which the etch was ineffective (about 0.02 in.).

The greater development of the plastic cone pattern (plastic zones reaching toward the specimen axis) in Fig. 25b than in Fig. 24c may be due to the following causes: 1) the onset of general yield may be governed in large part by the upper yield behavior through the value of σ_{nom}/σ_{UY}, 2) some other yield characteristic may cause the onset of general yield to occur at a lower value of σ_{nom}/σ_{LY} in the larger grain size specimens, and/or 3) the Lüder's strain and strain hardening characteristics may be such that thicker plastic spikes, arcs or cones are needed in larger grain size specimens to relieve the stresses in a highly stressed region.

These yield patterns were obtained under quasi-static loading conditions at room temperature. Both Green and Hundy (20) and Crussard et al. (18) report changes in the details of the strain patterns for impact loading. The effects of the intermediate rates of loading used here have not been investigated.

V. ANALYSIS

5.1 Approximate Stress Distribution in Notched Specimens

The maximum tensile stress in a loaded elastic body containing a notch occurs at the notch surface and can be calculated fairly accurately by techniques developed by Neuber (28). The presence of plastic enclaves, of the type shown in Figs. 24 and 26, for example, causes the point at which the maximum tensile stress occurs to be located in the interior of the body and greatly complicates the calculation of the stress distribution in the body.

An elastic-plastic stress analysis for tensile loading of the notched specimen geometry used for this thesis has been performed by Hendrickson, Wood and Clark (27, 41). Their procedure and results are discussed in Section 8.2. The plastic enclave boundary predicted by their calculations is different from the boundary determined with the aid of Fry's reagent in this study, however. The comparison is shown in Fig. 27 for a σ_{nom}/σ_{uY} ratio of about one. The two dot-dash curves of Fig. 27 represent the plastic enclave boundaries on each side of the specimen shown in Fig. 24-b. The dashed curves and the solid curves represent the theoretically determined boundaries and the experimentally determined boundaries (by microhardness measurements), respectively, according to Hendrickson et al. (27) for σ_{nom}/σ_{uY} ratios greater and less than that applied to the specimen shown in Fig. 24-b.

The boundaries of the wedge-shaped plastic enclaves of Figs. 24, 26 and 27 show marked similarities to the characteristic directions of the slip-line fields for a similar notch geometry shown

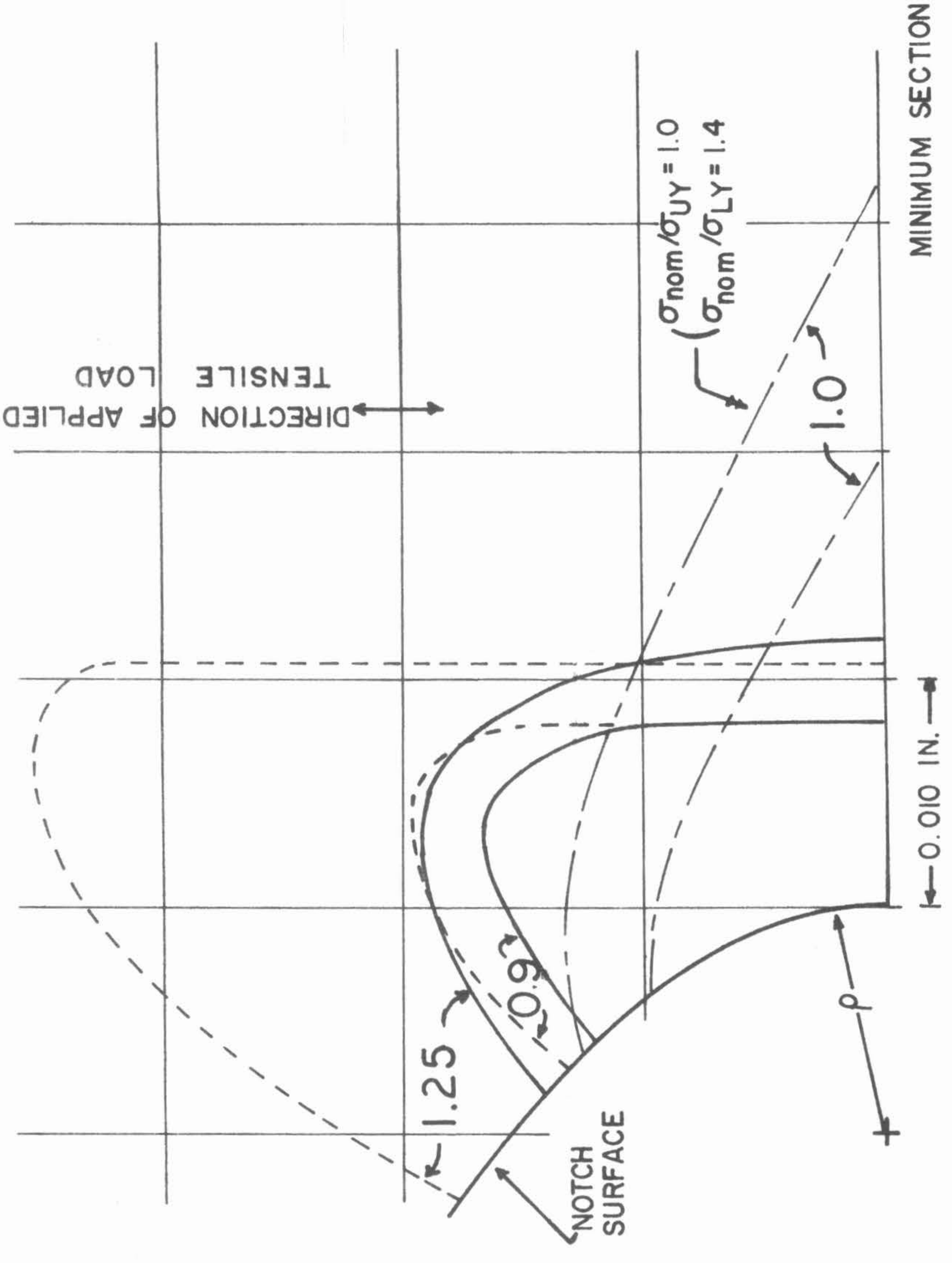

Fig. 27. Location of plastic-elastic interface near notch root in specimens loaded to value of σ_{nom}/σ_{UY} about 1.0. Dashed curve predicted by stress analysis of Hendrickson et al. (27). Solid curve determined by hardness measurements (27). Dash-dot curve determined with Fry's reagent in this investigation.

by Green and Hundy (20) and by Wilshaw and Pratt (30). This similarity suggests that the stress distribution in the plastic enclaves of the specimens tested in this study (the region $a \geq r \geq b$ in Fig. 28) may be calculated by slip-line field theory. If the stress distribution on the elastic core in the minimum section of the notched specimens (the region $b \geq r \geq 0$ in Fig. 28) could also be calculated, then the maximum tensile stress could be determined as a function of the nominal stress on the minimum section of a notched specimen and the yield stress of the material in the plastic regions. Analyses of the stresses in the plastic and in the elastic regions will be discussed separately.

A. *Slip-line field analysis for plastic enclaves* - The slip-line field theory outlined by Hill (29) can be used to calculate stresses in a plastically deforming region that is in a state of plane strain and for which suitable boundary conditions are known. Assumptions concerning material properties and stress states which are most easily handled by the slip-line field theory include the following:

1) The material is homogeneous and isotropic. Homogeneity implies averaging stresses over dimensions larger than the grain size or other metallurgical structure size.
2) The stress-strain state is one of plane strain wherein the third principal strain is a constant, but not necessarily equal to zero.
3) Plastic deformation occurs when the maximum shear stress reaches a critical value. This is the Tresca yield criterion.
4) The maximum shear stress is constant in the plastically deforming region; i.e., the material is non-strain hardening.
5) Displacements at the notch surface are small enough so that the

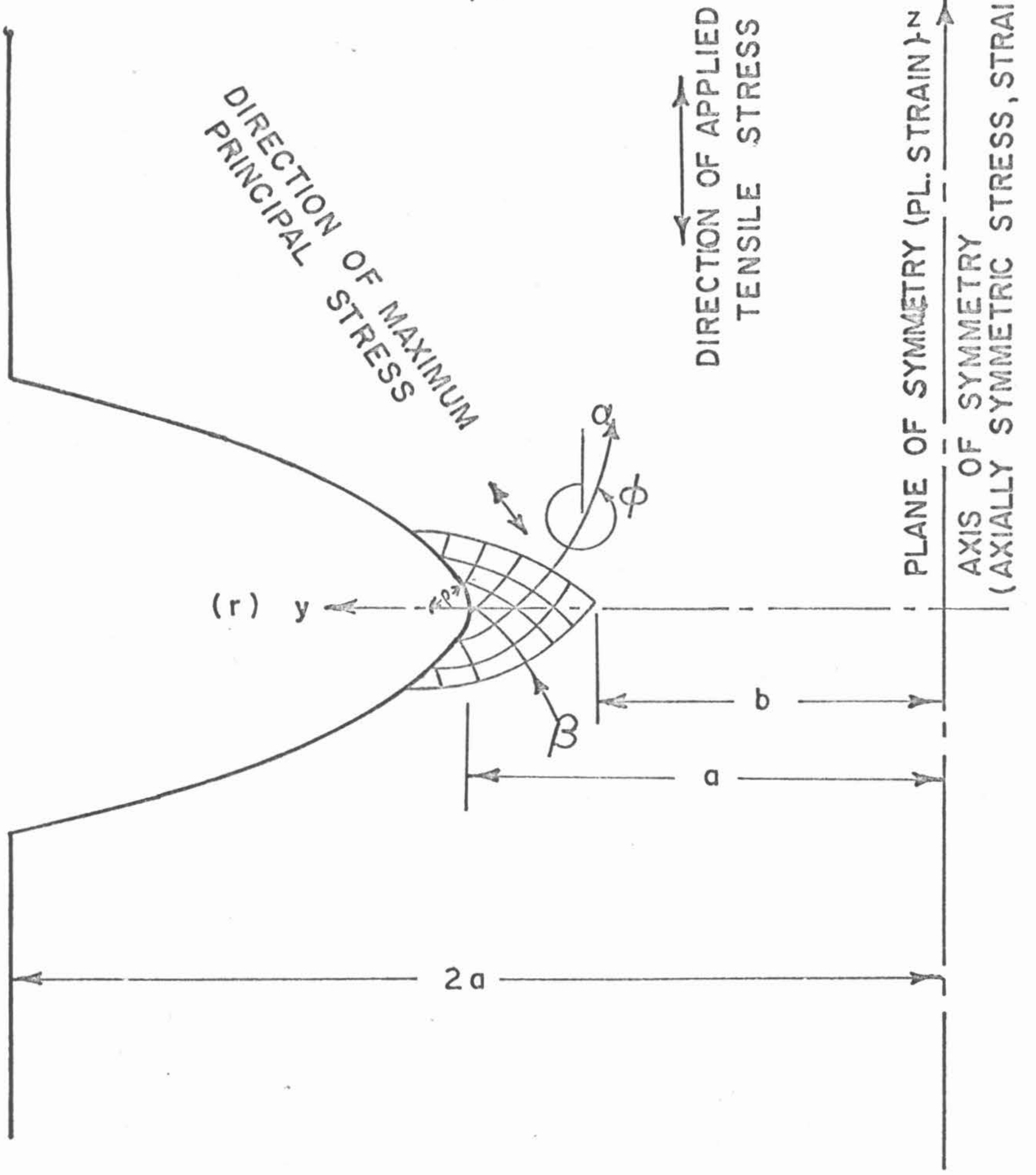

Fig. 28. Schematic drawing of specimen geometry used in stress analysis.

geometry of the notch surface remains unchanged during deformation.

The mathematics of the slip-line field theory is outlined in Appendix II using the notation and general procedure of Hill (29). The slip-line field theory is applied in Appendix II to the hyperbola-shaped notch contour of Fig. 28 for the condition of plane strain. The boundary conditions are that the normal stresses perpendicular to and tangent to the notch surface in the y-z plane are principal stresses and are equal to zero and σ_{yd}, respectively.

The error which results when the axially symmetric stress state of the notched specimens is approximated by a plane strain stress state is shown in Appendix II to have about the same magnitude as the error which results from the neglect of the strain hardening in the plastic region. These two errors are additive in their effect on the slip-line field and compensating in their effect on the value of the hydrostatic stress component. The flow stress of the material in the plastic region is not actually known because of inadequate knowledge of the stress-strain relation for plastic strains smaller than the Lüder's strain. Therefore the effect of strain hardening cannot be accurately calculated. Thus the plane-strain, constant-flow-stress solution for the slip-line field is not only expedient, but may also be more accurate than the solution which would have been obtained for the axially symmetric stress state.

Figure 29 shows the slip-line field (the directions of the maximum shear stress) obtained from the plane-strain solution; the ratio of the axial stress to the yield stress, σ_z/σ_{yd}, at various points

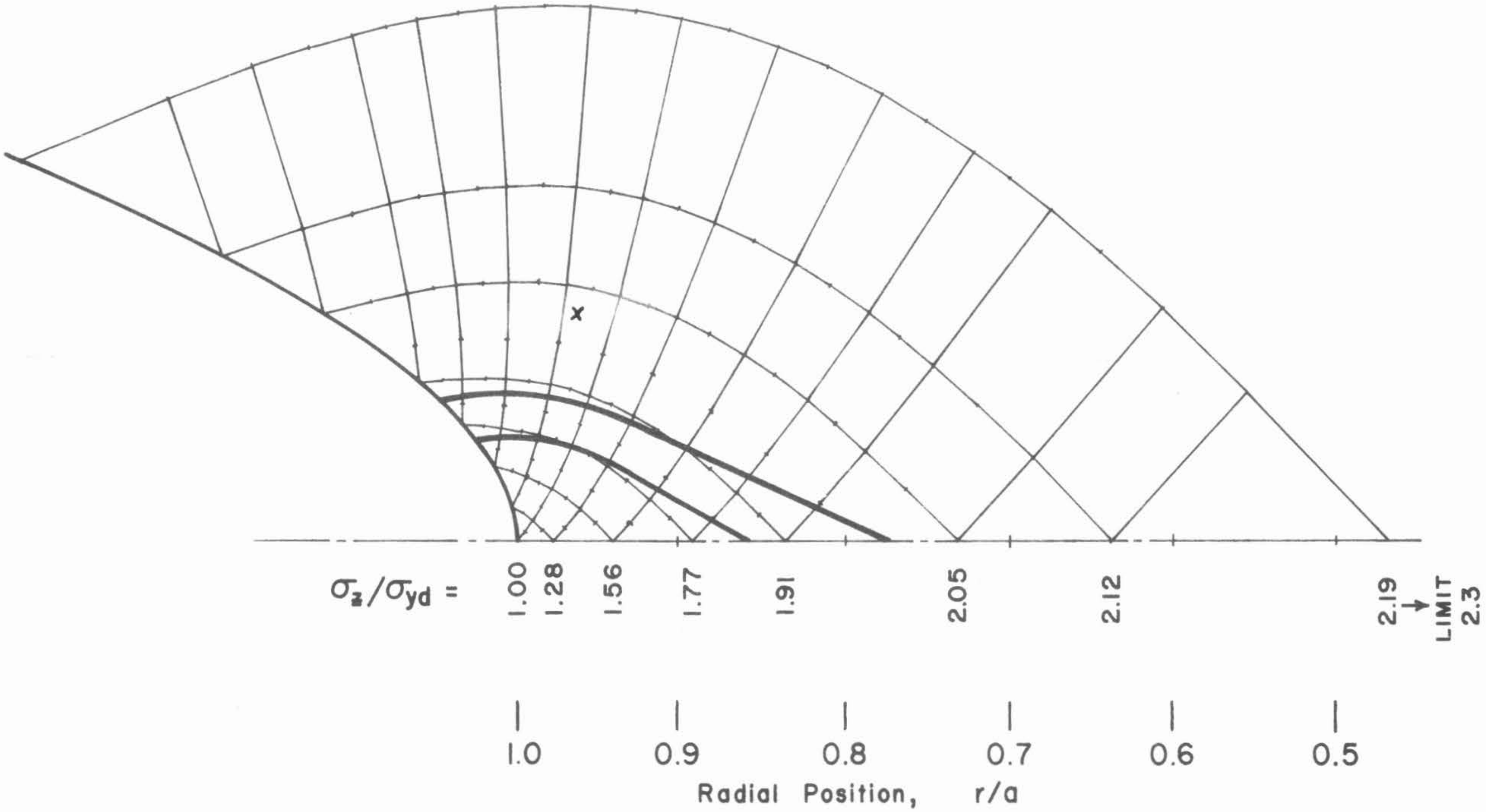

Fig. 29. Slip-line field for hyperbola shaped notch with $\rho/a = 1/15$. Plane strain. Heavy curves show plastic-elastic interface on two sides of specimen loaded to $\sigma_{nom}/\sigma_{LY} = 1.39$.

on the plane $z = 0$; and the plastic enclave boundary of the specimen shown in Fig. 24-b. The value of σ_z/σ_{yd} on the plane $z = 0$ is plotted as a function of the distance below the notch root in Fig. 30. The stress state at a point is given by the slip-line field solution only when the slip-lines connecting that point with the notch surface lie wholly within the plastic enclave. Thus the plastic enclave boundary will be assumed to follow a slip line for the purposes of this analysis. Then the axial force transmitted across a plastic enclave of depth $a \geq y \text{ (or } r) \geq b$ can be calculated by numerical integration of the axial stress over ring-shaped elements of area (axial symmetry of the notched specimens being considered now) on the $z = 0$ surface in the plastic enclave. This calculation is performed in Appendix II.

The major results that are now obtained from the stress analysis in the plastic region are the value of the maximum axial stress (at the plastic wedge tip, $r = b$) and the value of the axial tensile load transmitted across the plastic enclave as a function of the enclave depth. These values are recorded in Table 4 of Appendix II for reference after the stresses in the elastic core ($b \geq r \geq 0$ in Fig. 28) have been calculated.

B. Approximate Stress Distribution in the Elastic Core - It is difficult to perform an exact analysis for the stresses in the elastic core of the notched specimens after plastic enclaves have developed because the size of the enclaves analyzed with the aid of the slip-line field in the previous section is not known as a function of the applied load. Thus resort will be made to the inverse strategy of constructing a stress distribution in the elastic core that reflects the specimen geometry on the one hand and is sensitive to the local stresses at the

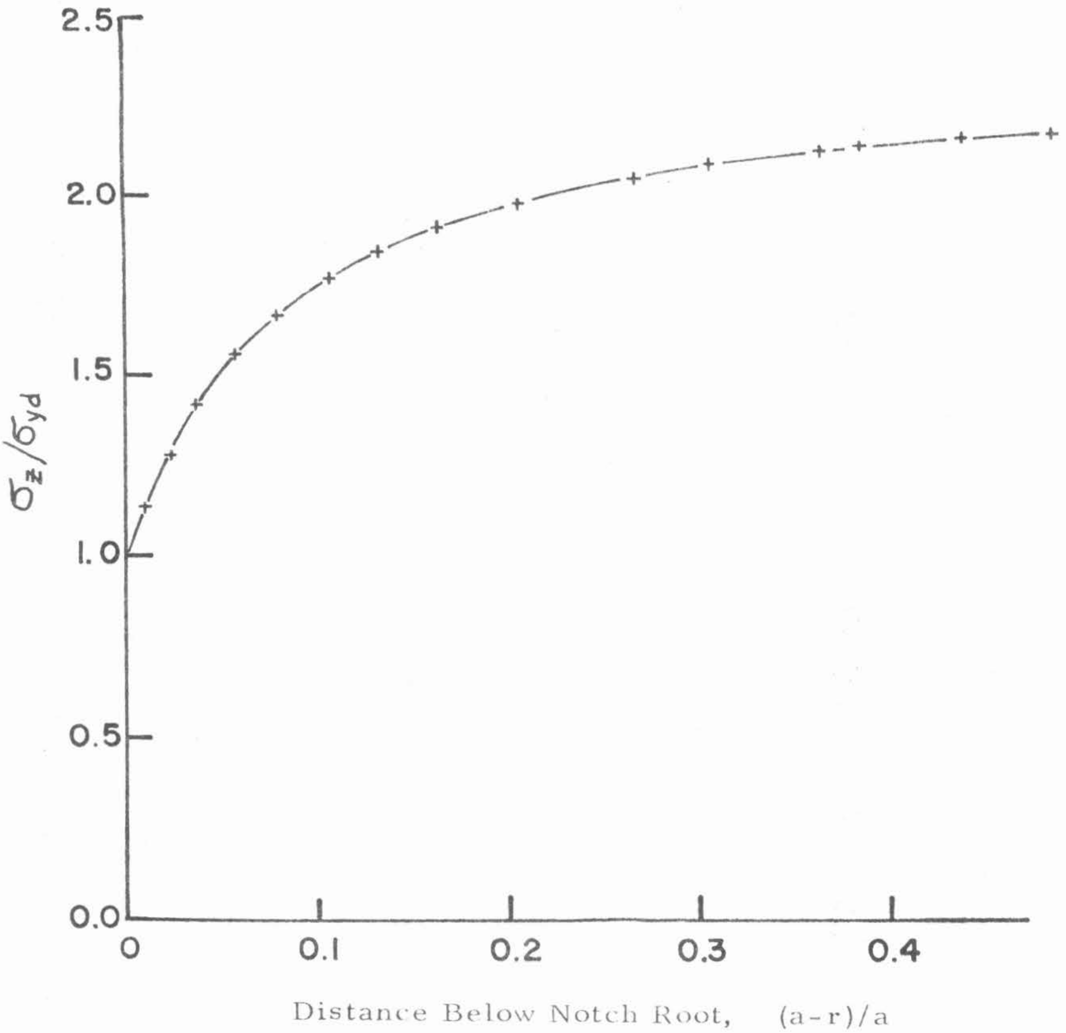

Fig. 30. Axial stress ratio, σ_z/σ_{yd}, predicted by stress analysis in plastic region as a function of distance below notch root.

tip of the plastic enclave on the other hand. This assumed stress distribution may then be integrated over the area of the elastic core to determine the axial load supported by the elastic core for any plastic enclave size. Two estimates of the elastic stress distribution will be made in order to determine the extent to which the ratio σ_{max}/σ_{yd} as a function of the σ_{nom}/σ_{yd} will be affected by the uncertainties of the stress distribution in the elastic core.

Neuber (28) has calculated the stress distribution in an axially symmetric elastic body containing a circumferential notch in the shape of an infinitely deep hyperboloid of revolution loaded in axial tension. The mathematical expressions for the stresses are given in Appendix III, along with the mathematical details involved in the following discussion. The axial, radial, and circumferential stresses, σ_z, σ_r, and σ_θ respectively, on the minimum section through the notch, $z = 0$, are shown in Fig. 31 as a function of the radius for the notch geometry, $\rho/a = 1/15$ used for the notched specimens described earlier in this thesis. A Poisson's ratio of $\nu = 0.30$ has been assumed for this steel.

The first estimate of the stress distribution in the elastic core, the region $b' \geq r \geq 0$ in Fig. 32, is based on the assumption that the stresses are distributed according to the elastic solution shown in Fig. 31 everywhere in the elastic core and that the axial stress, σ_z, is continuous across the plastic-elastic boundary at the tip of the plastic wedge. Thus tne axial stress on the entire minimum section would be given by the slip-line field solution σ_z^ρ in the region $a \geq r \geq b'$ of Fig. 32 and by the portion of Neuber's elastic solution for

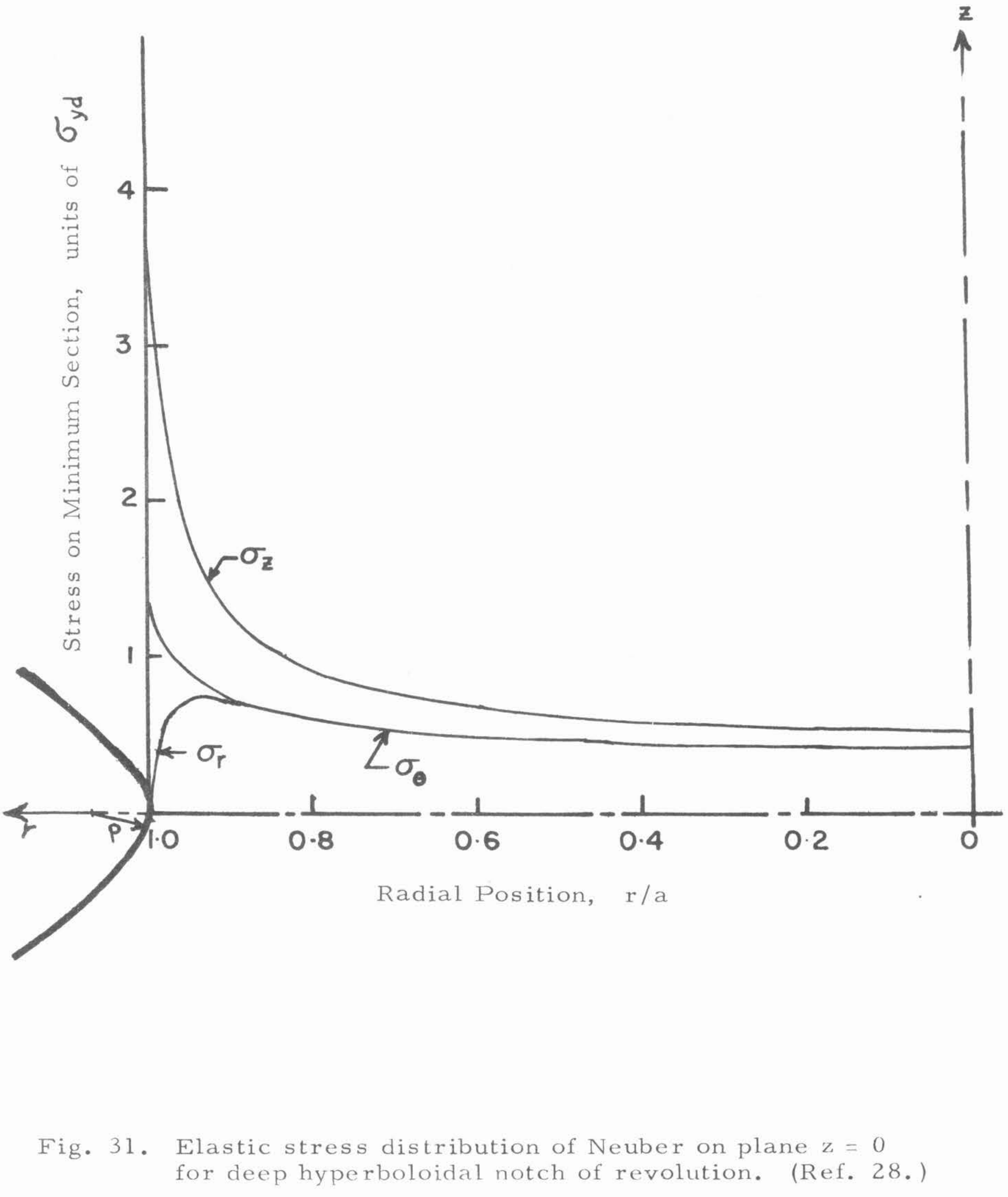

Fig. 31. Elastic stress distribution of Neuber on plane $z = 0$ for deep hyperboloidal notch of revolution. (Ref. 28.)

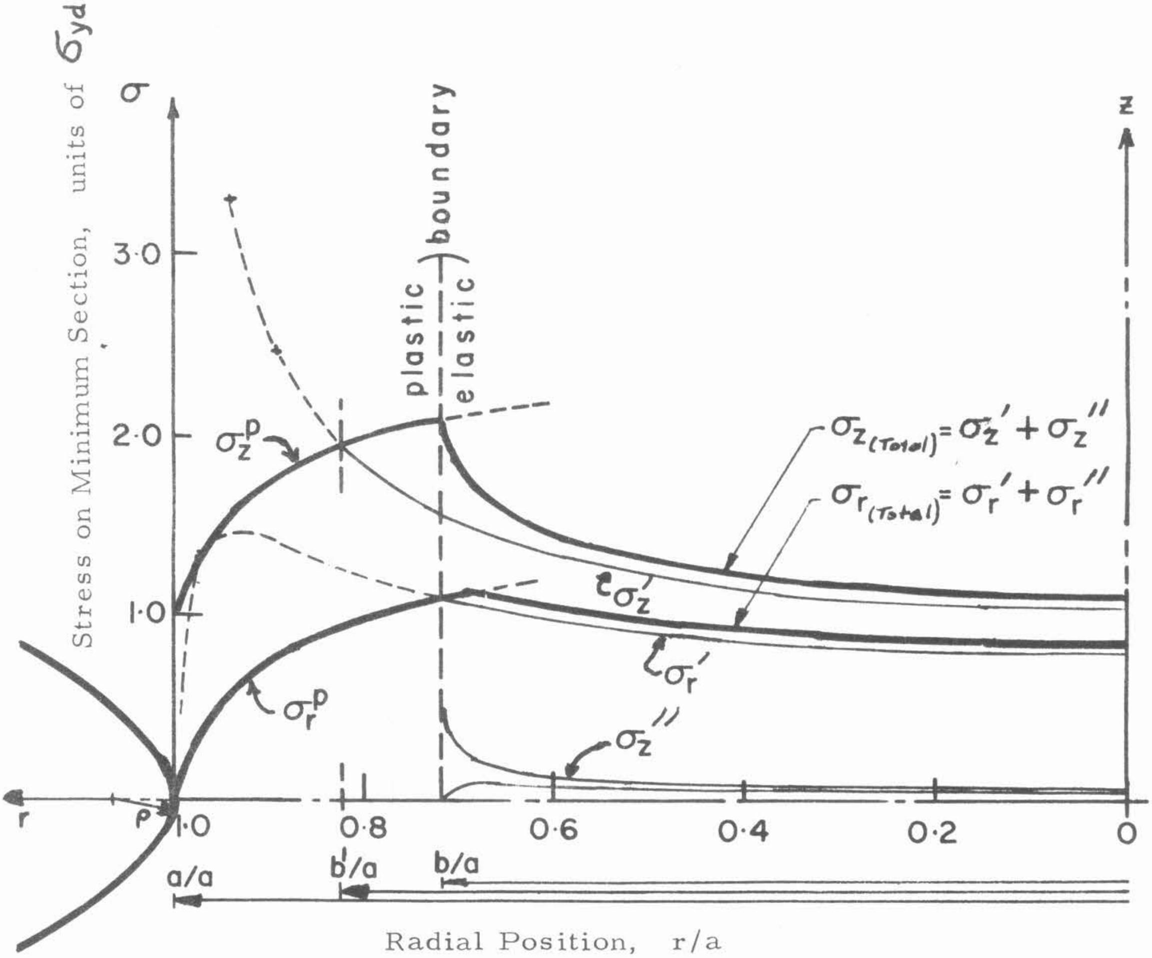

Fig. 32. Axial and radial stresses on plane $z = 0$ for two approximations used in stress analysis.

σ_z' in the region $b' \geq r \geq 0$, where the nominal stress, σ_{nom}', involved in Neuber's solution has been adjusted to make $\sigma_z^p = \sigma_z'$ at $r = b'$.

The axial stress, σ_z', has been integrated over the area of the elastic core to determine the axial tensile load transmitted by the elastic core for several depths of penetration of the plastic enclave. These calculations are performed in Appendix III and the results are recorded in Table 4 of Appendix II. This calculation, combined with the previous calculations of tensile loads and stresses in the plastic enclave, permit the construction of Fig. 33, wherein the ratio σ_{max}/σ_{yd} (occurring at the tip of the plastic wedge-shaped enclave) and the plastic enclave depth are shown as a function of σ_{nom}/σ_{yd}. The solid lines show the relationships predicted by this first approximation of the stress distribution in the elastic core.

A second estimate of the stress distribution in the elastic core has been made in which both the axial and radial stress components are continuous across the plastic-elastic boundary on the minimum section of the specimen. (The first estimate of the stress distribution in the elastic core has resulted in a discontinuity of the radial stress component at the plastic-elastic boundary, as is shown by the curves for σ_r^p and σ_r' at $r = b'$ in Fig. 32.) Suppose that the plastic enclave extends from $r = a$ to $r = b$ in Fig. 32 and that the axial and radial stress components in this region are given by σ_z^p and σ_r^p, respectively. The nominal stress, σ_{nom}', of Neuber's elastic solution is adjusted so that the radial stress components are continuous at $r = b$. Then the stress components in the elastic core given by

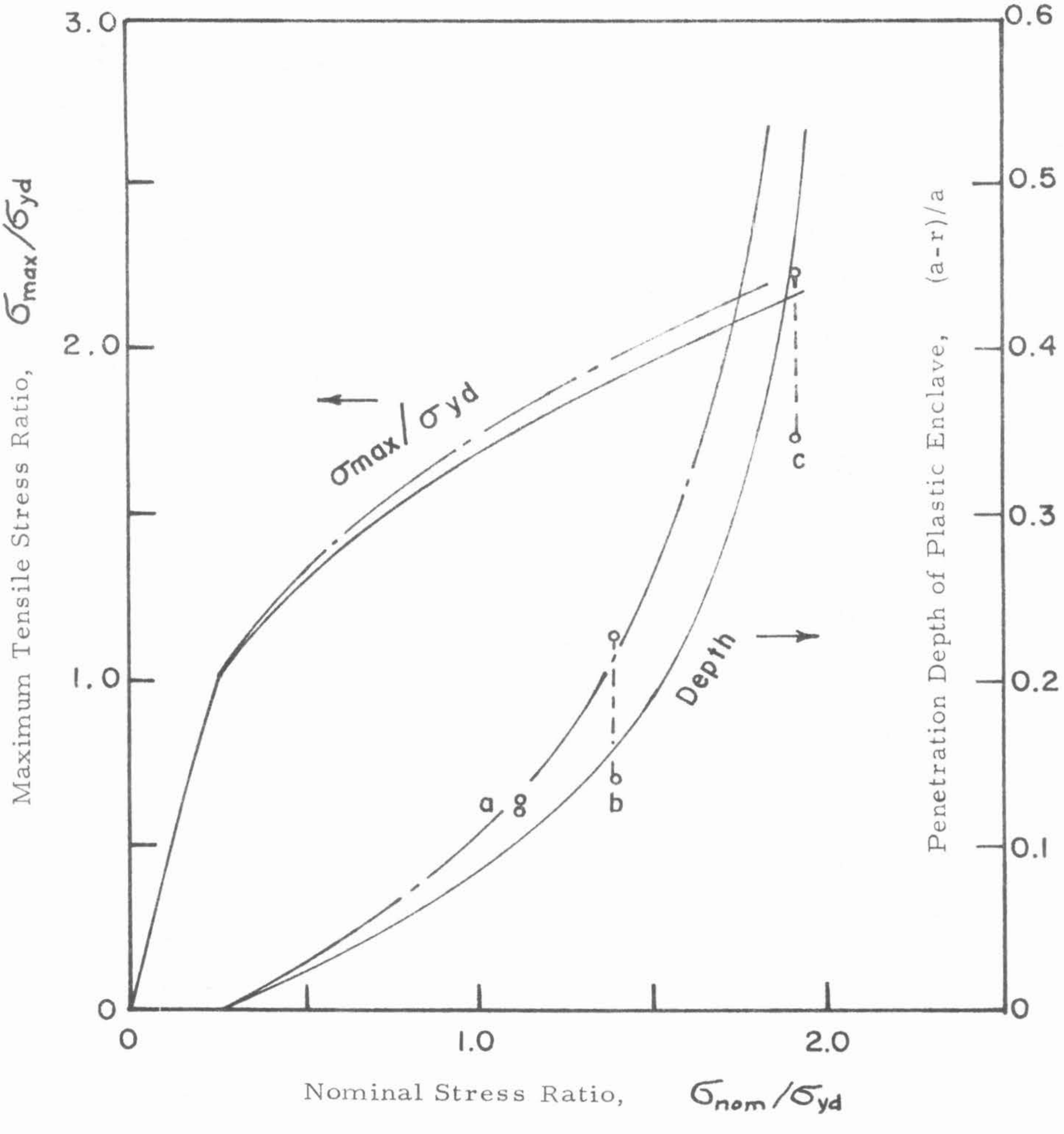

Fig. 33. Maximum tensile stress ratio, σ_{max}/σ_{yd} , and plastic enclave depth vs. nominal stress ratio, σ_{nom}/σ_{yd}.

Neuber's solution for this nominal stress value are shown by σ_z' and σ_r' in the region $b \geqslant r \geq 0$. Now the axial stress, σ_z, is discontinuous at the plastic-elastic boundary. This defect is corrected in the following manner. Suppose that the plastic enclave resembles a notch and causes an additional stress concentration in the elastic region at r = b. For convenience, the hypothetical notch which represents the plastic enclave will be assumed to be a hyperboloid of revolution entirely similar to the original notch whose root is located at r = a, but scaled down so that the hypothetical notch root is located at r = b. Thus the radius of curvature at the root of this hypothetical notch is $\rho'' = \rho \frac{b}{a}$. The nominal stress, σ''_{nom}, of the Neuber solution for this hypothetical notch is chosen so that the total axial stress in the elastic region, $\sigma_z' + \sigma_z''$, at the plastic elastic boundary on the minimum section is equal to σ_z^p. Since $\sigma_r'' = 0$ at r = b, the radial stress component is still continuous at r = b.

The final stress distribution in the plastic and elastic regions for this second approximation of the stresses in the elastic core is shown by the dash-dot curves where they differ from the first approximation in Fig. 32. The relationships among σ_{max}/σ_{yd}, the plastic enclave depth and σ_{nom}/σ_{yd} obtained from this second approximation of the stresses in the elastic core are shown by the dot-dash curves in Fig. 33. The calculations involved in constructing the curves in Fig. 33 are given in Appendix III.

5.2 The Value of the Yield Stress in the Plastic Region

Numerical values of the stress acting on the minimum cross-section of the notched specimens at the instant of fracture may be calculated by means of the foregoing stress analysis provided that the yield stress appropriate for each particular test condition is known. The yield stress in the plastic enclaves of the notched specimens is a function of the temperature and rate of load application because the upper and lower yield stresses in a simple tension test are functions of these variables. The yield stress in the plastic enclaves will be assumed to be more closely related to the lower yield stress than to the upper yield stress because large regions (compared to the grain diameter) of plastically deformed material are present in both the plastic enclaves of the notched specimens and in unnotched tensile specimens during elongation at the lower yield stress. This assumption differs from that of Hendrickson, Wood and Clark (27), who assumed that the yield stress in the plastic enclave was equal to the upper yield stress determined from a simple tension test.

The plastic elongation which occurs at the lower yield stress in a simple tension test takes place by the propagation of a plastic strain front of constant amplitude (the Lüder's strain) along the gage length of the specimen rather than by a uniform rate of plastic strain over the entire gage length. Therefore the lower yield stress must be a function of the rate of propagation of the Lüder's strain front rather than a function of the average plastic strain rate. The assumption is made that the yield stress in the plastic enclave of a notched specimen during a test at a given temperature is equal to the lower yield stress in an unnotched tensile specimen tested at the same temperature in which the Lüder's strain front propagates at the same velocity as the velocity of propagation of the plastic enclave boundary in the notched specimen.

The elongation rate of an unnotched specimen and the Lüder's front velocity at the lower yield stress are related by

$$\dot{L} = \sqrt{2}\, v_L \varepsilon_L \qquad [5.1]$$

where $\dot{L}$ is the specimen elongation rate (the abscissae of Figs. 12, 14, 15 and 17), v_L is the Lüder's front velocity (measured normal to the Luder's front), ε_L is the Lüder's strain, and the factor of $\sqrt{2}$ occurs because the Lüder's front makes an angle of about 45 degrees with the specimen axis. If the Lüder's strain is taken to be about 0.018 for all test rates and temperatures and for both grain sizes (this assumption is likely to be true within a factor of two, which is relatively inconsequential), the specimen elongation rate is equal to one fortieth (1/40) of the Lüder's front velocity. This calculation is based on the assumption that only one Lüder's front is propagating through the gage length of the specimen. Equation 5.1 and Figs. 12, 14, 15 and 17 permit the determination of σ_{LY} as a function of v_L for the various test conditions and grain sizes.

The velocity of the plastic enclave boundary in a notched specimen may be estimated with the aid of the photomicrographs in Fig. 24. The calculation is based on the wedge-shaped enclaves only. It is assumed that the wedge-shaped plastic enclaves shown in Fig. 24c attained their final dimensions just prior to the onset of general yield. The stress ratio (nominal stress divided by the lower yield stress) at the instant general yield was nucleated was probably slightly less than 1.91, the value which caused the plastic strain pattern in Fig. 24c. However, the value of 1.91 will be used for the value of σ_{nom}/σ_{LY} associated with the plastic wedge size shown in Fig. 24c.

Average values of the half-width of the plastic wedges shown in Fig. 24 are plotted against σ_{nom}/σ_{LY} (assuming quasi-static test conditions) in Fig. 34. The average slopes of the two segments of this curve are equal to 0.021 in. within a factor of two. Thus the plastic-elastic boundary will be assumed to move at the rate of 0.021 in. per unit change in σ_{nom}/σ_{LY} for the large scale notched specimens used in this investigation. (The wedge boundary velocity will vary approximately linearly with the specimen scale factor.) The plastic wedge front velocity in these large scale notched specimens prior to general yield is thus taken to be

$$V_w = \frac{(0.021 \text{ in.})\,\dot{\sigma}_{nom}}{\sigma_{LY}} \qquad [5.2]$$

where V_w is the velocity of the boundary of the plastic wedge, $\dot{\sigma}_{nom}$ is the nominal stress rate, and σ_{LY} is the (yet to be determined) lower yield stress value associated with the test conditions.

The assumption that $V_w = V_L$ when the shear stress at the plastic wedge boundary in a notched specimen is equal to the shear stress at the Lüder's front in an unnotched specimen now permits a lower yield stress value to be associated with a nominal stress rate on the large scale notched specimens. The value of σ_{LY} to be used in equation 5.2 has yet to be determined, but the magnitude of $\dot{\sigma}_{nom}$ is so much more important that any reasonable estimate for σ_{LY}, e.g., $\sigma_{LY} \approx$ 50,000 lb/in.^{2}, is acceptable for a first approx-

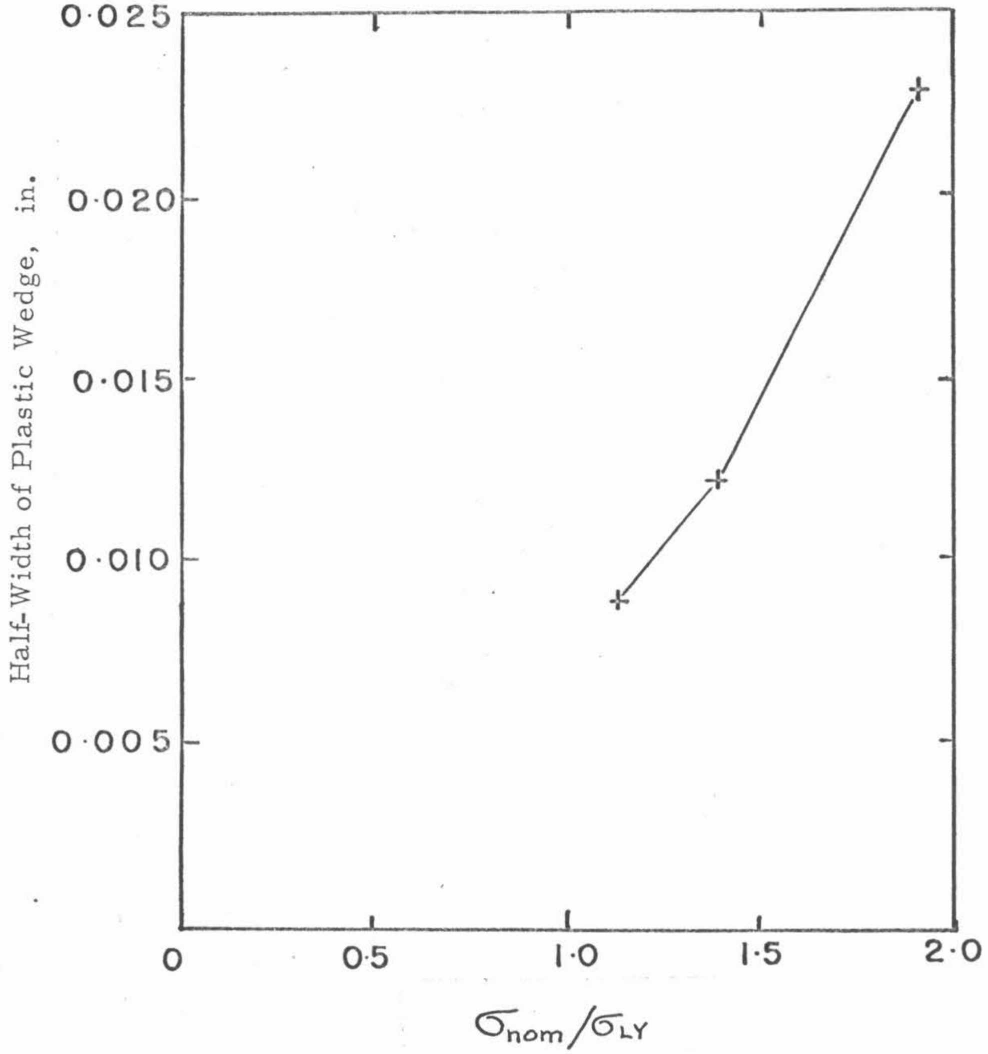

Fig. 34. Growth rate of plastic enclave.

imation. The approximate value of V_w can now be calculated from equation 5.2. The desired value of the lower yield stress is that value which is associated with an unnotched-specimen elongation rate equal to one fortieth of V_w (from equation 5.1) at the appropriate temperature. The value of σ_{LY} obtained from this calculation could be used in equation 5.2 to obtain a new value of σ_{LY} by repeating the calculation. This new value of σ_{LY} will not be improved significantly by further iteration.

The calculations outlined above have been performed on the lower yield stress data of Figs. 12, 14 and 17 and the results are shown in Fig. 35. The curves of Fig. 35 show the yield stress at the plastic-elastic boundary as a function of the nominal stress rate of the large-scale notched specimens, according to the plastic-elastic boundary velocity concepts discussed in this section.

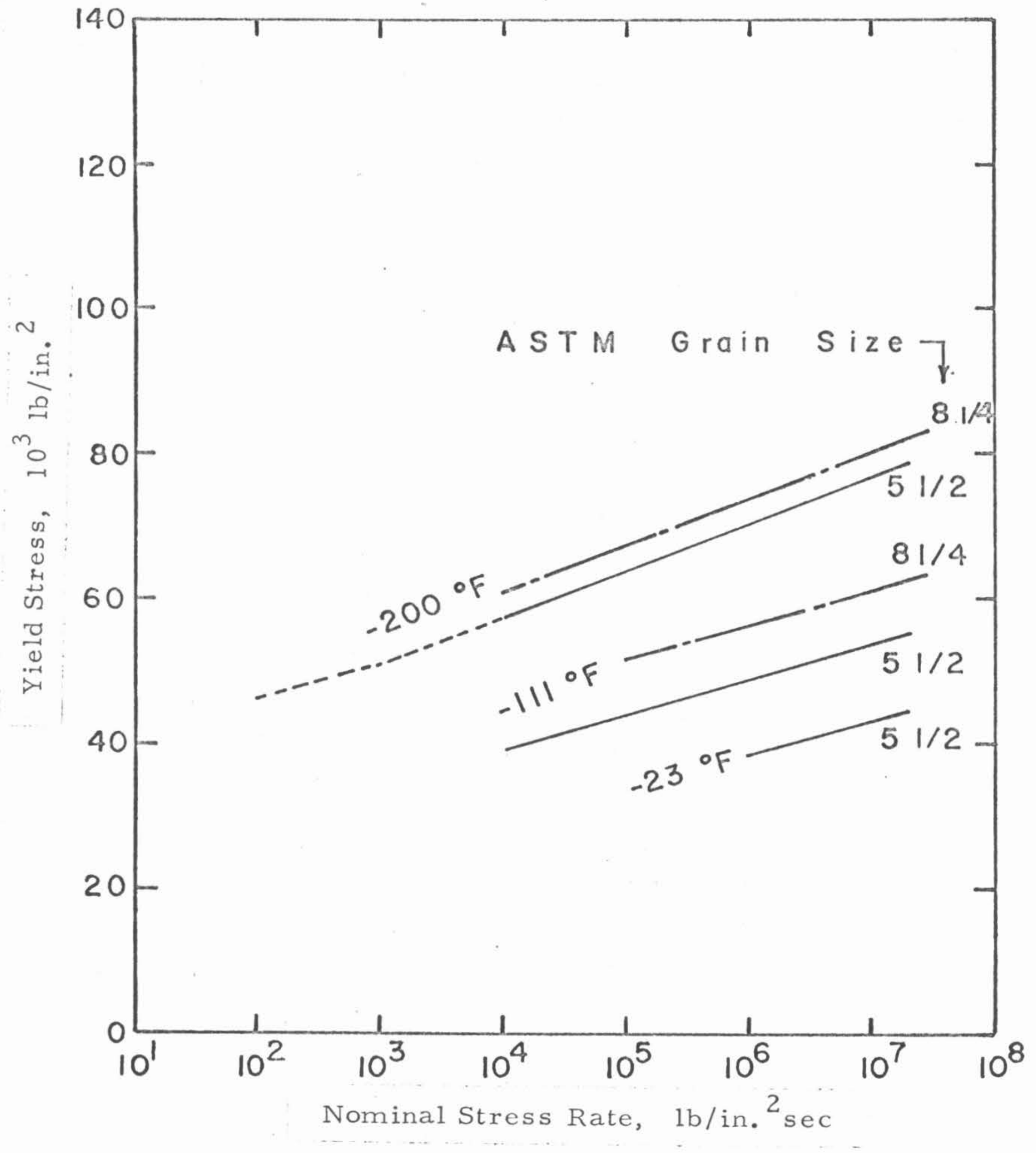

Fig. 35. Yield stress in plastic enclave at root of notch vs. nominal stress rate. Dashed portion of curve is an extrapolation.

VI. RESULTS OF LOCAL FRACTURE STRESS CALCULATIONS

The yield stress of the material in the plastic enclaves prior to the onset of general yield has been calculated for each of the notched specimens with the aid of Fig. 35. These values of σ_{yd} are listed in Table 1. The loading rate for the small scale specimens, series D, was divided by the factor 2.6 for the purpose of obtaining a yield stress through the use of Fig. 35. The factor 2.6 is the ratio of the scale factors of the large and small scale specimens and was applied to the small scale specimens since the yield stress calculation of Section 5.2 is based on the velocity of the propagation of the plastic-elastic interface in the large scale specimens.

The ratio of the nominal fracture stress to the yield stress is also given in Table 1. The penetration depth of the wedge-shaped plastic enclaves shown in Fig. 24c after the onset of general yield is plotted by the pair of circles labeled "c" in Fig. 33 as a function of σ_{nom}/σ_{yd} (equal to σ_{nom}/σ_{LY} for quasi-static test conditions). Comparison of the penetration depth of this enclave and of the predictions of the stress analysis developed in Section 5.1 shows that the stress analysis is applicable only when $\sigma_{nom}/\sigma_{yd} \lesssim 1.75$.

The value of the maximum tensile stress at the instant of fracture initiation has been calculated for each of the notched specimens for which $\sigma_{nom}/\sigma_{yd} \lesssim 1.75$. The average of the values of σ_{max}/σ_{yd} shown in Fig. 33 was used in these calculations. The calculated values of σ_{maxf} are listed in Table 1 and are also plotted in Fig. 36 as a function of the plastic enclave depth in units of the average grain chord. The values of σ_{maxf} for the small grain size specimens range from 121,000 lb/in.^{2} at the tip of the largest plastic enclaves to 157,000 lb/in.^{2} at the tip of the next to the smallest plastic enclave.

The onset of general yield in the large grain size specimens has not been investigated in sufficient detail to ascertain that general yield has not occurred in the specimen shown by the "x" in Fig. 36. The value of σ_{nom}/σ_{yd} for this large grain size specimen was 1.79. This value suggests general yield. Therefore, a value of σ_{maxf} less than about 123,000 lb/in.^{2} for the large grain size specimens should not be inferred with certainty from Fig. 36.

The value of the maximum tensile stress, σ_z , at a point 11.1×10^{-3} in. from the tip of the wedge-shaped plastic enclave, toward the notch root, has been calculated for each of the small grain size specimens involved in Fig. 36. The calculation was performed with the aid of the curve of σ_z/σ_{yd} vs. distance under the notch root shown in Fig. 30. The values of σ_z at this interior point are shown in Fig. 37. All but one of these values lie in the range 118,000 ± 4,000 lb/in.^{2}.

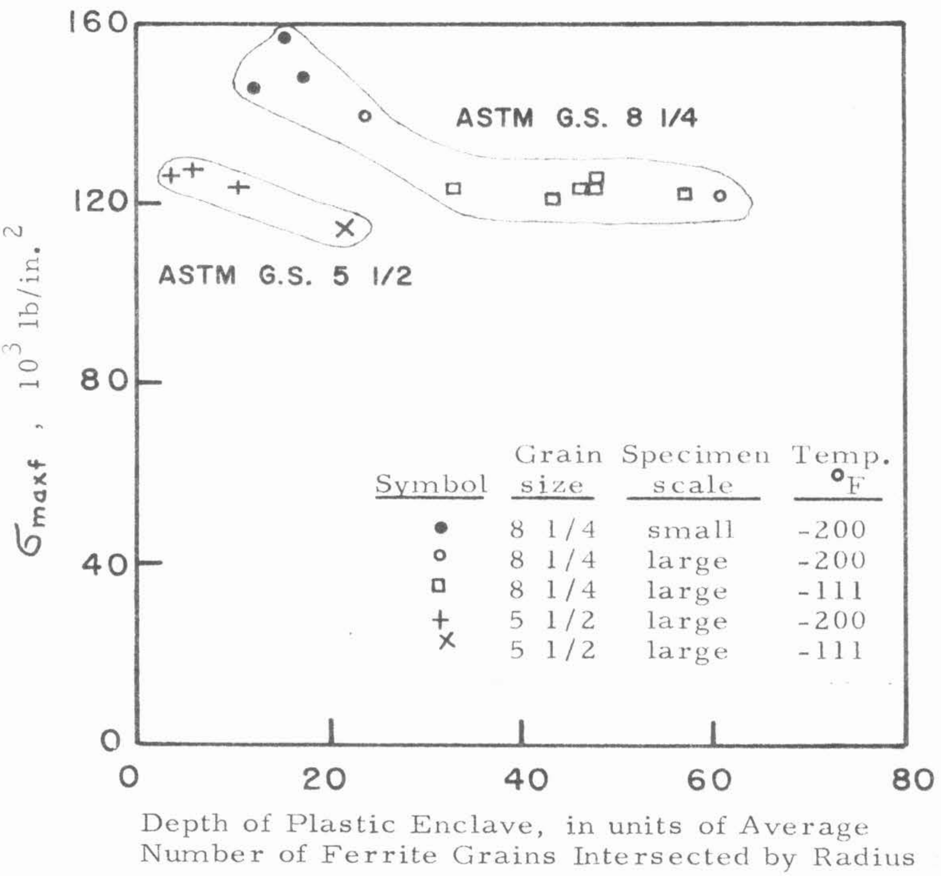

Fig. 36. Maximum tensile stress at fracture vs. plastic enclave depth.

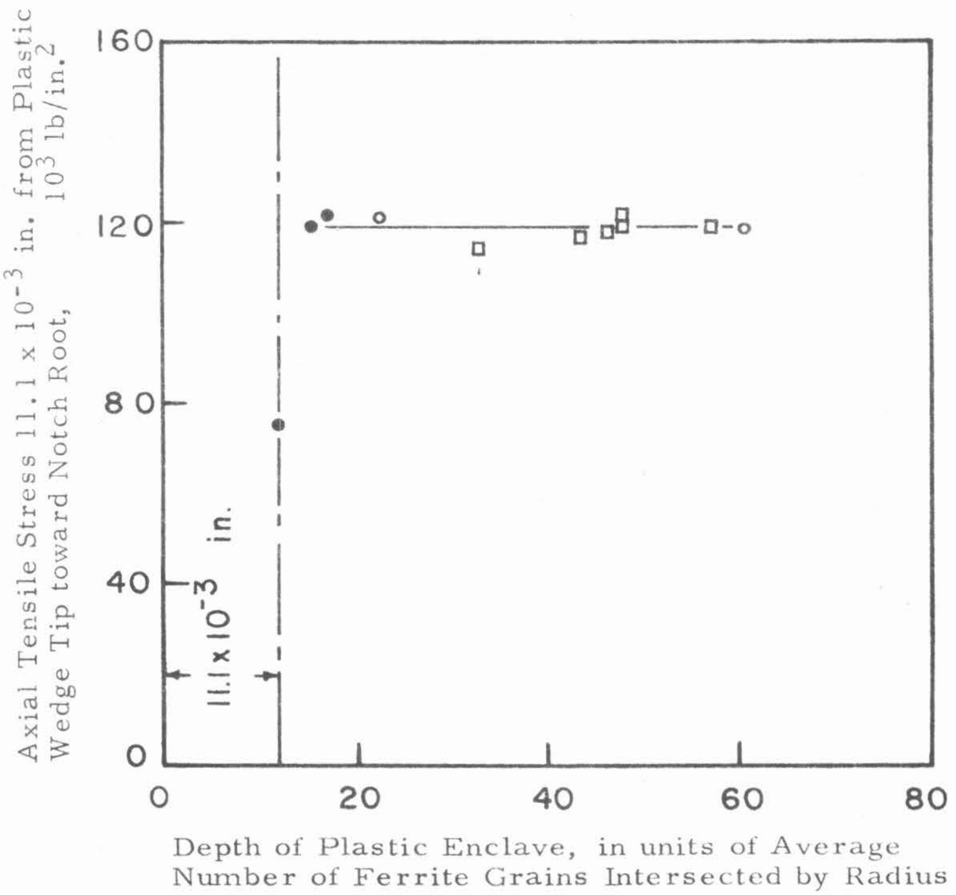

Fig. 37. Axial stress at a specific point in the plastic enclave vs. enclave depth. Symbols are keyed to Fig. 36.

VII. DISCUSSION OF FRACTURE INITIATION

7.1 Fracture Mode Transition

The nominal fracture stress values for the small grain size specimens shown in Fig. 20 and listed in Table 1 show a transition from low values of about 90,000 to 100,000 lb /in.^{2} at high nominal stress rates to high values of about 130,000 lb /in.^{2} at lower nominal stress rates. These approximate values apply to the large scale specimens. This transition in nominal fractures stress values appears to be related to the onset of general yield of the type shown in Fig. 24c.

Examination of Fig. 20a shows that fracture tests have been run at the low stress rate limit of the low nominal fracture stress mode at the fracture mode transition for the small grain size, large scale specimens. The limiting values of $\sigma_{nomf}/\sigma_{yd}$ at -200°F and -111°F for the low nominal fracture stress mode are 1.75 and 1.72. (No significance is attached to the difference between these values since there is scatter in the nominal fracture stress data and the flow stress values at -200°F have been estimated indirectly by the method discussed in association with Fig. 17.)

The penetration depth of the plastic wedges in the notched specimen that was loaded quasi-statically until general yield had just occurred, as shown in Fig. 24c, is plotted with the pair of circles labeled "c" in Fig. 33. The stress analysis described in Section 5.1 predicts that plastic enclaves would penetrate to that depth at a load ratio of $\sigma_{nom}/\sigma_{yd} \approx$ 1.70 to 1.85. The agreement between the values of σ_{nom}/σ_{yd} calculated for the onset of general yield and for the limit of the low nominal fracture stress mode is taken as evidence that the fracture level transition is associated with the onset of general yield in these notched tensile specimens. The smallest value of $\sigma_{nomf}/\sigma_{yd}$ calculated for fracture in the high stress mode is 2.2 for the large scale specimens and 2.0 for the small scale specimens. Thus, fracture is initiated in the high nominal fracture stress mode after the onset of general yield in this investigation.

The nominal fracture stress transition is not as abrupt for the large grain size specimens as for the small grain size specimens. Most of the large grain size specimens fractured at a nominal stress of about 100,000 lb /in.^{2} after the onset of general yield. The etch pattern shown in Fig. 25 b suggests that the onset of general yield occurs at a lower value of σ_{nom}/σ_{yd} in the large grain size specimens than in the small grain size specimens, but the nominal fracture stress value is fairly insensitive to the fact of the onset of general yield.

7.2 Maximum Stress at Fracture

The minimum calculated value of the maximum local tensile stress at the instant of fracture, about 122,000 lb /in.^{2} at the tip of the large plastic wedge-shaped enclaves in the small grain size material, as shown in Fig. 36, is considerably smaller than the value of 210,000 lb /in.^{2} reported by Hendrickson, Wood, and Clark (27) for this same steel with a very slightly larger grain size (ASTM grain size No. 8, vs. 8 1/4 in this investigation). The discrepancy between these two stress values arises in part from the identification of the yield stress in the plastic enclaves with σ_{LY} in this thesis and with σ_{UY} in their work. The stress analysis described in Section 5. 1 of this thesis also predicts a slower rate of increase in the value of the axial stress as a function of distance below the notch root in the plastic enclaves, as will be shown in the discussion of these stress analyses in Section 8. 2.

Wood and Clark (45) have measured the fracture stress on unnotched specimens of this steel in tensile tests at -320°F (-196°C). Two specimens that had been loaded "quasi-statically" ($\dot{\sigma}_{nom} \approx 7 \times 10^2$ lb /in.^{2}sec.) fractured at about 111, 000 lb /in.^{2} after about 2 to 3 percent plastic strain. They had been subjected to an upper yield stress value of about 125, 000 lb /in.^{2} and had reached a minimum value of the tensile stress of about 106, 000 lb /in.^{2} at 0. 6 percent plastic strain during the course of the test prior to fracture. A third specimen fractured immediately upon attaining the upper yield stress value of about 127, 000 lb /in.^{2}. Fracture also occurred in 8 out of 13 of their delay time tests (simple tension) at -320°F at tensile stresses ranging from 114, 000 to 128, 000 lb /in.^{2}. Failure to have observed fracture in the other 5 specimens of this group may imply that the stress was too low (111, 000 lb /in.^{2} for two specimens) or that the maximum plastic strain of between 1 and 2 percent obtainable in these tests was too small to initiate fracture in some of the specimens. (Three of the specimens which had not fractured had been subjected to a pre-yield stress level of about 127, 000 lb /in.^{2}.)

The significance of the remarkable coincidence in the values of the maximum tensile stress at the instant of fracture initiation in the notched specimens tested for this thesis and of the fracture stress observed by Wood and Clark is difficult to assess, since markedly different values of the maximum shear stress and of the plastic strain are present in the two cases. Also, the dislocation activity associated with yielding may be somewhat different at the very low test temperature employed by Wood and Clark. The value of the maximum shear stress ranged between 30,000 and 40,000 lb /in.^{2} in the plastic enclaves of the notched specimens tested for this thesis and ranged between 55,000 and 64,000 lb /in.^{2} in the unnotched tensile specimens tested by Wood and Clark. The plastic strain near the tip of the wedge-shaped plastic enclaves in the notched specimens has been estimated to have a value of $\epsilon_p \approx 0.1$ percent. (The basis for this estimate will be discussed in Section 8.3.) On the other hand, plastic strains of the order of several percent seem to be necessary for fracture initiation at this stress level in the unnotched tensile specimens. Until the nature of the embrittling effect of moderate plastic strains (several percent) in unnotched tensile specimens is understood, the mechanism that permits fracture to be initiated in a region of smaller values of the plastic strain and of the shear stress near notches will probably remain obscure.

Clausing (23) has calculated the value of the maximum tensile stress at the instant of fracture initiation in this steel as a function of the local plastic strain in notched specimens in which the ratio of the root radius of the notch to the radius of the minimum section was about unity. He concluded that fracture could be initiated by a tensile stress of about 95,000 lb /in.^{2} after a plastic strain of about 1 percent. The fracture stress increased with increasing strain to about 140,000 lb /in.^{2} after a plastic strain of 14 percent. His fracture stress values also agree favorably with the value of σ_{maxf} calculated in this thesis and the fracture stress found by Wood and Clark (45).

It is interesting that Clausing calculated a fracture stress value of about 95,000 lb /in.^{2} after about 1 percent plastic strain in his notched specimens, while Wood and Clark did not observe fracture at a tensile stress of 106,000 lb /in.^{2} at 0.6 percent plastic strain in their quasi-static tests. One possible cause for this apparent contradiction could be related to the difficulty in performing accurate elastic-plastic stress analyses in notched steel specimens. Another cause might be an actual difference in material properties arising from slight differences in the annealing treatment. A third cause may actually arise from an interdependence of the shear stress and the plastic strain on an embrittling effect. A fourth cause may be related to the difference in the material properties at the different test temperatures. The relative importance of these four possible causes for the apparent difference in fracture initiation behavior cannot be assessed with the data available here.

The obvious conclusion that fracture is initiated in this mild steel in a plastic region where the tensile stress has attained a value of about $120,000 \begin{smallmatrix} +\ 10,000 \\ -\ 20,000 \end{smallmatrix}$ lb /in.^{2}, depending upon the plastic strain, appears somewhat uncertain in view of the high values for the maximum tensile stress shown in Fig. 36 at the tip of the smallest plastic enclaves.

7.3 Plastic Enclave Size Effect

The calculated value of σ_{maxf} in the small grain size notched specimens increases with decreasing plastic enclave depth below about 0.03 in., as shown in Fig. 36. If the value of the maximum tensile stress, albeit located at the tip of the plastic wedge in a region of very small plastic strain, controls the initiation of fracture, then a geometry-scale size effect is implied by the trend of σ_{maxf} in Fig. 36.

However, the axial tensile stress in all but one of the small grain size specimens at a point 11.1×10^{-3} in. from the plastic wedge tip toward the notch root has an approximately constant value of $118,000 \pm 4,000$ lb/in.^{2} at the instant of fracture, as shown in Fig. 37. (The capricious behavior of the specimen which does not follow the pattern set by the others is reminiscent of the quasi-static tests of Wood and Clark in which one specimen broke before any appreciable specimen elongation could occur after the upper yield stress had been attained.) If the value of the maximum tensile stress at this interior point is the critical parameter in a fracture criterion for this steel in the small grain size state, then there is no further apparent size effect over this range of plastic enclave depths.

One interpretation of a fracture stress criterion in a plastic region at a specific distance from the plastic-elastic interface could be based on the necessity of achieving critical plastic strain activity prior to fracture initiation. Felbeck and Orowan (11) reported that a cold-worked layer 0.012 to 0.016 in. thick existed adjacent to fracture surfaces in their steel. This cold-worked layer could be an unavoidable consequence of the high stress fields near the tip of a propagating sharp crack, or it could be an important aspect of crack propagation by providing suitable dislocation activity to nucleate new microcracks just ahead of the main crack. The points in the plastic enclave where the axial tensile stress was calculated for Fig. 37 are situated about a constant distance of $\sin 28^{\circ} \times 11.1 \times 10^{-3}$ in. $= 5.22 \times 10^{-3}$ in. from the plastic-elastic interface.

The fracture data obtained on unnotched specimens by Hahn, et al. (15), shown in Fig. 1, and by Wood and Clark (45), as discussed in Section 7. 2, are consistent with the concept of an embrittling effect from plastic strains up to a value of several percent. Crussard, et al. (18) have suggested that the maximum tensile stress is not a suitable fracture criterion, but that both the tensile stress and the embrittling effect of plastic straining are involved in the fracture criterion.

Larger plastic strains closer to the notch root in the specimens tested in this study are implied by two observations. 1) The fact that the plastic enclave boundary becomes more nearly parallel to the slip-line field at points farther from the tip of the plastic wedge implies the existence of larger plastic strains there. This will be shown in Sections 8. 3 and 8. 4. 2) The region in which high microhardness values were measured by Hendrickson, Wood, and Clark (27) is located immediately adjacent to the notch root, as shown in Fig. 27. Thus, the region in which the more uniform value of 118, 000 lb / in.^{2} was calculated for the fracture stress, as shown in Fig. 37, contains larger plastic strains than exist at the wedge tip, where the values for σ_{maxf} , shown in Fig. 36, were calculated.

However, the stress calculation employed for the data in Fig.

37 does not imply a stress-strain criterion for fracture that is independent of the specimen scale size, because the tensile stress was not calculated at geometrically equivalent points in the specimens of the two different sizes. It should not be assumed, though, that the stress-strain states of geometrically similar specimens should be identical.

An accurate stress-strain analysis for notched specimens of mild steel should include not only the appropriate stress-strain flow behavior for small plastic strains and strain rate effects, but also the effect that limited slip band lengths have upon the yield behavior of the material. The yield behavior of mild steel in regions where micro-slip bands are limited to lengths several times as long as the average grain diameter may be appreciably different from the yield behavior in large regions of plastic flow, as will be discussed in Section 8. 5.

Only after the stress and plastic strain states have been properly calculated, at least to the approximation of a homogeneous, isotropic material, and the stress and plastic strain state at the point of initiation of fracture has been determined, is it possible to ascribe residual size effects to statistical effects (36, 37), to the necessity of averaging the stresses over some critical assemblage of grains (11, 46), and/or to the loss of geometrical similarity when a microcrack of grain diameter dimensions develops (38). Notice that the loss of geometrical similarity because of plastic yielding characteristics over grain diameter dimensions will already be incorporated in the refined stress analysis techniques. Consideration of the stress state in the neighborhood of a point might be the first order attempt to adapt the calculations based on homogeneous, isotropic, continuum mechanics to the embrittling effect of a weak assemblage of grains in the real, inhomogeneous material.

7.4 Conjectures on the Phenomenology of Fracture Initiation

The conditions that are conducive to fracture initiation in a mild steel are probably describable in terms of a locus of values in maximum tensile stress - plastic strain space. (The actual inhomogeneity of the material implies that stress-strain calculations based on a homogeneous material may have to be averaged over some volume element related to a small multiple of the average grain volume.) The fracture locus in this space would depend upon the exact state of the material and would be modified by prior plastic straining followed by aging, for example. Different nominal fracture modes would be observed as the fracture locus was approached along different stress-strain paths.

When the first plastic enclave of restricted size develops near a notch in a mild steel, the plastic strains are very small, so a high tensile stress value is needed to initiate fracture. As the plastic enclave grows with increased loading of the specimen, larger tensile stresses are built up near the new plastic-elastic interface. At the same time, though, the plastic strain in other parts of the plastic enclave is increasing, causing both a direct embrittling effect and a slight increase in the maximum tensile stress because of strain hardening. It is presumed that the fracture locus is met at a fairly high tensile stress level and a fairly small plastic strain level.

If fracture has not been initiated before the onset of general yield, the stress state near a notch is altered markedly by the formation of the first thin sheets of plastically deformed material at the onset of general yield. Now a region of high plastic strain exists just under the notch root in a region where the hydrostatic tensile stress component is still quite small. With increasing load supported by the specimen, the plastic spikes grow in thickness (because of strain hardening) and regions of moderately high plastic strain (about the Lüder's strain value) extend farther into the specimen from the notch root. The plastic strain value that has the maximum embrittling effect must be located near the front of the advancing plastic spikes. Finally, the front will penetrate deeply enough below the notch that the maximum tensile stress has attained a sufficiently high value to initiate fracture. The cracked pearlite patch shown in Fig. 23 may be associated with this mode of fracture initiation.

Depending upon the test conditions, rate and temperature, and the properties of the material, this second opportunity for fracture initiation may or may not have been fulfilled before the plastic strains near the notch root become large enough to nucleate cracks by a ductile mode. This third approach to the fracture locus will occur at the highest plastic strain and the lowest tensile stress values.

Clausing (23) has investigated a stress-strain locus for fracture initiation and has observed a ductile mode occurring at a strain of 30 percent in notched specimens and about 60 percent in unnotched specimens. The fracture stress could have any value between 110, 000 and 140, 000 lb. /in. ^{2} during fibrous initiation in the notched specimens.

The photomicrographs of successive cylindrical surfaces below the notch root in the large grain size specimen, No. A-31, that was elongated extensively at room temperature, are shown in Fig. 22. Two voids, ② and ③ , are confined to the depth interval from 0.003 to 0.016 in. below the notch surface. These voids do not extend to the free surface. The width of the third void, ① , suggests that it also was nucleated below the notch root. Thus, the nucleation site for these three voids was at an interior point where the value of the plastic strain is very high and the value of the maximum tensile stress is moderately high; not in the region of the maximum plastic strain at the notch root.

Thus, it appears that all regions in a plastic enclave developing in a mild steel must be investigated for stress-strain values and compared with a fracture criterion locus in stress-strain space. The region in the plastic enclave where the fracture criterion is most likely to be met, and the point on the fracture locus which describes the stress-strain state in this region will probably change as the plastic enclave grows.

VIII DISCUSSION OF YIELDING

8.1 Role of Yielding in Fracture Studies

An understanding of the yield behavior of mild steel is important in a study of the brittle fracture behavior of this material for the following reasons: 1) General yield and brittle fracture are, in a sense, competing modes of failure of steel structures. 2) The yield behavior of the steel must be known in order that the stress and plastic strain state through a structure can be calculated (and compared with a fracture criterion). 3) Yielding plays an instrumental role in fracture initiation. Plastically deformed material is found to a depth of several grain diameters on both sides of a propagating crack (11), and it has been shown that yielding must precede fracture initiation in mild steel (13, 14, 15, 18, 23).

Attention will be directed in this chapter toward the problems associated with the analysis of the stress state in and near regions of discontinuous plastic straining. Particular consideration is given to the question of whether all of the relevant properties of a material which exhibits a yield instability have been incorporated into existing stress analysis techniques. The conveniences of isotropy and homogeneity will normally be assumed for most of the discussion and will be explicitly revoked only when the inaccuracies arising from their use are thought to be comparable to errors arising from other sources.

8.2 Previous Elastic-Plastic Stress Analyses in Plane Strain

A numerical relaxation technique has been used by Allen and Southwell (31) to calculate values of the Airy stress function which satisfy finite difference representations of the biharmonic equation in the elastic region and a second order, second degree partial differential equation in the plastic region of a plane-strain notched specimen geometry loaded in tension. The stress function was first relaxed subject to the elastic equation at all nodes of the finite difference net. All nodes at which the calculated value of the maximum shear stress equaled or exceeded the yield criterion were subsequently relaxed subject to the plastic equation while the remaining nodes were simultaneously relaxed subject to the elastic equation. Throughout the relaxation procedure, a node was considered to remain in the elastic region only so long as the calculated value of the maximum shear stress at that point was less than the value of the yield criterion. In this way a plastic-elastic interface was determined by drawing a line (surface in three dimensions) between adjacent nodes which had been relaxed subject to the two different partial differential equations.

Hendrickson, Wood and Clark (27) applied the numerical stress analysis technique used by Allen and Southwell (31) to the specimen geometry (in plane strain) studied for this thesis. They explicitly identified the Tresca yield criterion with the non-linear partial differentiation equation employed in the plastic region. The results of their calculations differ in two important respects from the results reported in Chapters IV and V of this thesis. First, the shape of the plastic enclaves determined by them is different from the shape of the plastic enclaves revealed by etching with Fry's reagent in this study. Figures 27 and 24 illustrate the contrast. The plastic enclaves are revealed in the present work as being wedge shaped with a sharp point (on a scale larger than the grain diameter) at the minimum section, $z = 0$. The plastic enclave contour deduced by Hendrickson et al. does not exhibit a similar discontinuity. Furthermore, the plastic enclave predicted by Hendrickson et al. encloses large regions of material in the axial direction from the notch root not identified as being plastic in the etch figures. A feature of these regions is that one set of slip lines is terminated at both ends by the elastic-plastic interface. This may be seen by comparing the Hendrickson enclave shown in Fig. 27 with the slip line field for this notch contour shown in Fig. 29.

The second major disagreement between the results of the stress analysis performed by Hendrickson et al. and the work performed for this thesis lies in the calculated value of σ_z / σ_{yd} on the plane $z = 0$ in the plastic enclave as a function of distance below the notch root. The axial stress distribution over a portion of the minimum section near the notch root calculated by Hendrickson for a plane strain specimen loaded in tension such that $\sigma_{nom}/\sigma_{yd} = 0.81$ is shown in Fig. 38. This stress distribution integrated over the minimum section of an axially symmetric specimen corresponds to a nominal tensile stress ratio of $\sigma_{nom}/\sigma_{yd} = 0.98$ (rather than 0.90, as reported by Hendrickson et al.). The axial stresses calculated by the slip-line field theory and by the two approximate elastic stress analyses discussed in Chapter V are also shown in Fig. 38 for the load

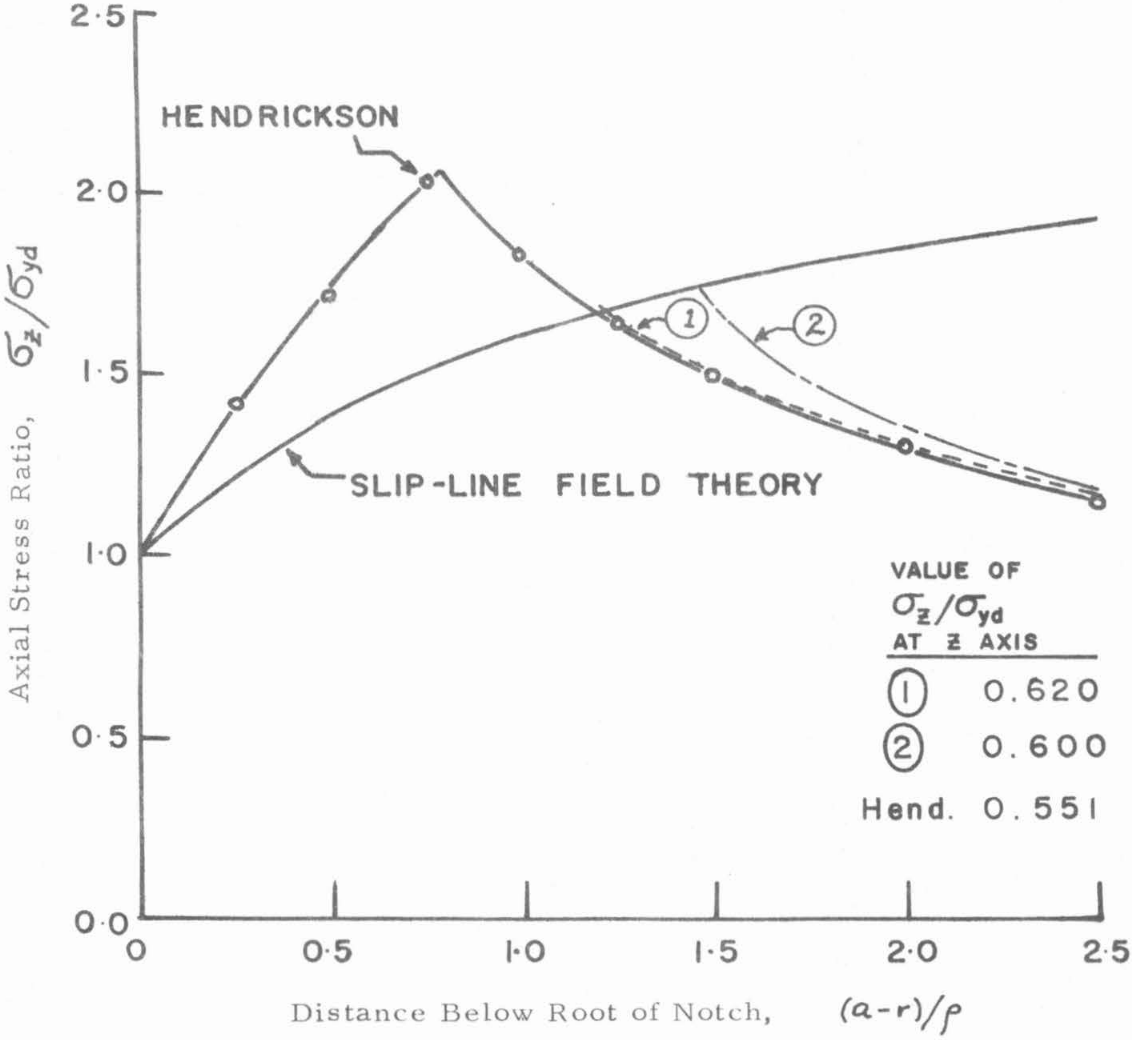

Fig. 38. Comparison of the elastic-plastic stress states near a notch predicted by Hendrickson, Wood and Clark (27) and by the analysis described in this thesis. The axial stress ratio, σ_z/σ_{yd}, is shown as a function of the distance below the notch root in the minimum cross section.

intensity ratio σ_{nom}/σ_{yd} = 0.98 (axial symmetry). The curves with positive slope correspond to stresses calculated in the plastic regions. The axial stress calculated by Hendrickson in the plastic region increases about twice as fast as a function of distance below the notch root as does the axial stress calculated by the slip-line field theory. Since the same assumptions concerning the material properties were made for the plastic region of both stress analyses, at least one of the stress analyses must be in error.

The stress analysis performed by Hendrickson (41), and reported by Hendrickson, Wood and Clark (27), has been examined in some detail and a number of possible sources of error have been located.

1.) The non-linear second order partial differential equation for the Airy stress function in the plastic region is essentially hyperbolic in nature (Hill (29)) so appropriate care must be taken in formulating the field equations and applying the boundary conditions. The slip-line field theory is based on the hyperbolic nature of the equations and thereby ensures appropriateness of the solution when suitable boundary conditions are known (which is the case for most of the plastic region shown in Fig. 29). The hyperbolic nature of the nonlinear partial differential equation is evidenced by the absence of the value of the stress function at the central node of the group of nodes involved in the finite difference representation of the equation (Shield (47) and Morse and Feshbach (48)). Any properly formulated set of equations and boundary conditions for the plastic region must predict the same values for the stresses as are predicted by the slip-line field theory. It is not obvious that the relaxation technique used by Allen and Southwell (31) and by Hendrickson et al. (27, 41) in the plastic region satisfies this requirement.

2.) The nodes of the relaxation net may be too widely spaced relative to 1) the curvature of the slip-line field and 2) the depth of the plastic enclave. The mesh size should probably be small enough that the rotation of the principal stress axes is less than perhaps five degrees over the entire relaxation pattern associated with each point.

3.) The stress function may not have been relaxed sufficiently. Values of the axial stress ratio, σ_z/σ_{yd} , and of the transverse stress ratio, σ_y/σ_{yd} , were calculated from values of the stress function given in Fig. 12 of reference (41). These values are shown as a function of position in and near the plastic enclave in Fig. 39. The vagary of the values of the stress ratios in the column located a distance $\Delta y = \frac{1}{4}\rho$ below the notch root is taken as evidence that the stress function has not been relaxed well throughout the plastic region. The adjacent elastic region also shows similar non-uniformity of stress gradients. While it is possible that larger blocks of nodes show better overall relaxation, this would just intensify the previous objection that the relaxation net may have been too coarse.

The three possible sources of errors discussed above refer mainly to the discrepancy between the axial stress ratio predicted by Hendrickson and by the slip-line field theory used in this thesis, as was shown in Fig. 38. The excessive width (in the axial direction) of the plastic enclave as predicted by Hendrickson (see Fig. 27) may

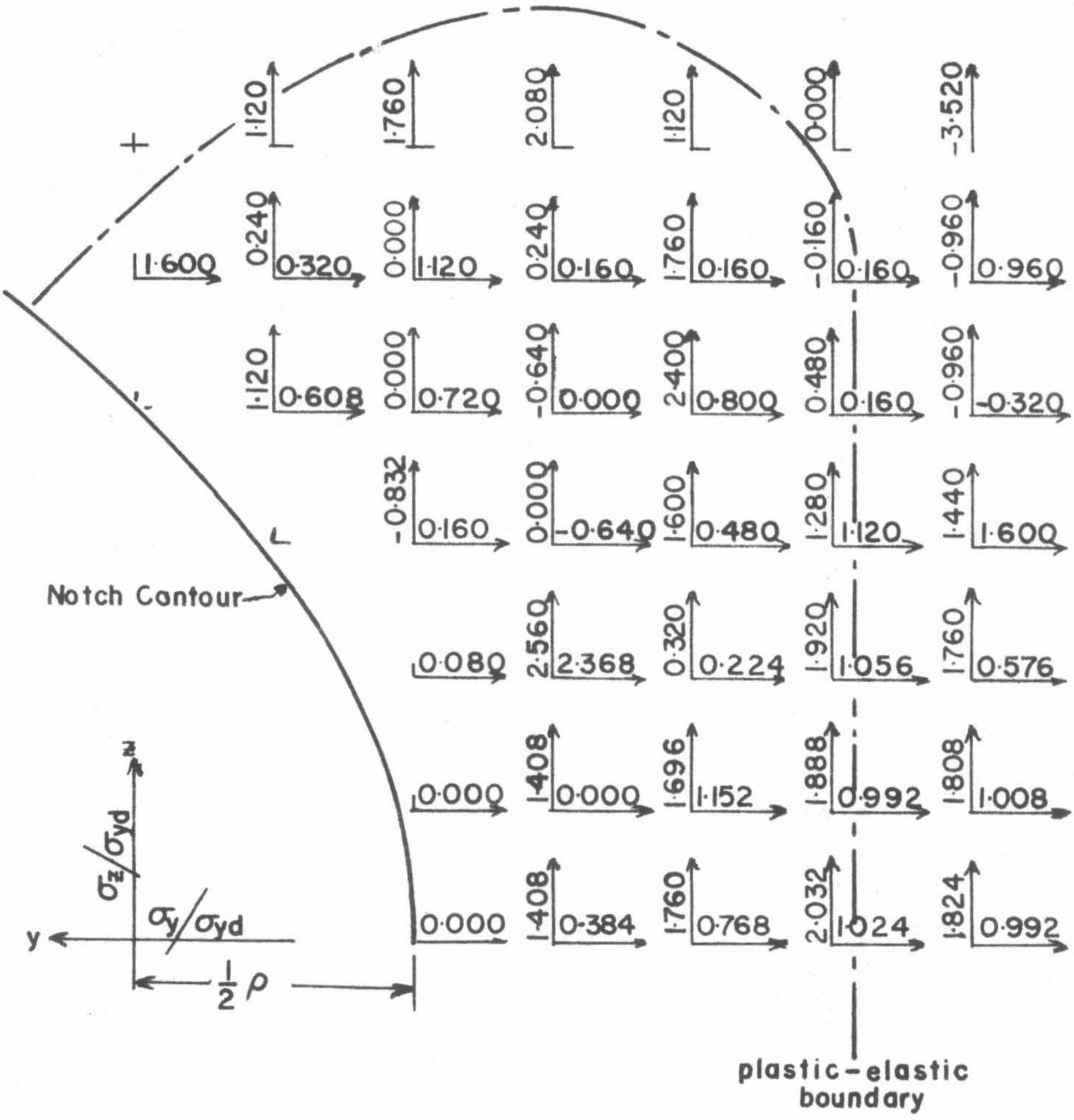

Fig. 39. Values of σ_y/σ_{yd} and σ_z/σ_{yd} in plastic enclave at notch root calculated from stress function given by Hendrickson (41).

have been caused in part by failure to consider the plastic strains and their influence on the stress field. This matter will be discussed later in this chapter.

Even if the stress analyses performed in Chapter V of this thesis and by Hendrickson et al. (27) had shown agreement in most major respects, two more improvements in the application of the results of the plane-strain analysis by Hendrickson are possible.

1.) The nominal stress ratio in axial symmetry to which a stress distribution calculated in plane strain corresponds should have been calculated by integrating the axial stress distribution over the area of the minimum section. For example, the stress distribution calculated by Hendrickson for a nominal stress ratio of $\sigma_{nom}/\sigma_{yd} = 0.81$ in plane strain was assigned to an axially symmetric specimen loaded to give a nominal stress ratio of 0.90. However, this reported stress distribution (calculated from the stress function given in Figs. 11 and 12 of Hendrickson's thesis (41)) has been numerically integrated over the minimum section of an axially symmetric body and has been found to correspond to a nominal stress ratio of 0.98.

2.) The flow stress of the material inside the plastic enclave might better have been correlated with the lower yield stress than the upper yield stress as measured on unnotched specimens. The basis for this suggestion will be discussed later in this chapter.

The circular notch contour which was analyzed in tension by Allen and Southwell (31) was much less sharp ($\rho/a = 1$) than the one analyzed by Hendrickson, Wood and Clark (27). Thus the coarseness of the relaxation net used by Allen and Southwell is less likely to be a source of large errors. It is interesting to note that the plastic enclave predicted by them for the highest tensile load prior to general yield has a smooth boundary and also extends a considerable distance in the longitudinal direction just below the notch root. This is in general agreement with the results of Hendrickson et al. Hill (29) has called attention to the fact that the existence of an appropriate velocity field has not yet been demonstrated in those regions wherein slip lines connect two points on the elastic-plastic interface. And Shield (47) has suggested that a finite difference formulation of the differential equations may not be capable of predicting a wedge-shaped boundary since the finite difference approximations would automatically blunt the wedge tip and thus be unable to detect a "preference" for a sharp angle in the elastic-plastic interface. Thus it is possible that the discrepancy between the plastic enclave shape predicted by the analysis techniques of Allen and Southwell and the etch figures found for this thesis arises from inappropriate stress-strain analysis procedures. Other possible causes for this discrepancy will be discussed in the next sections.

8.3 Stress State Discontinuity at a Plastic-Elastic Interface

The tendency for the plastic-elastic interfaces to be parallel or nearly parallel to slip-line directions in the plastic regions is a striking feature of yielding in the mild steel tested in this investigation, as can be seen in Fig. 29, and of similar mild steels studied by others (18, 20, 30). The etch pattern in Fig. 40 shows narrow plastic spikes that extend in the direction of the maximum shear stress. The etch pattern shown in Fig. 40 was developed on the midsection (plane

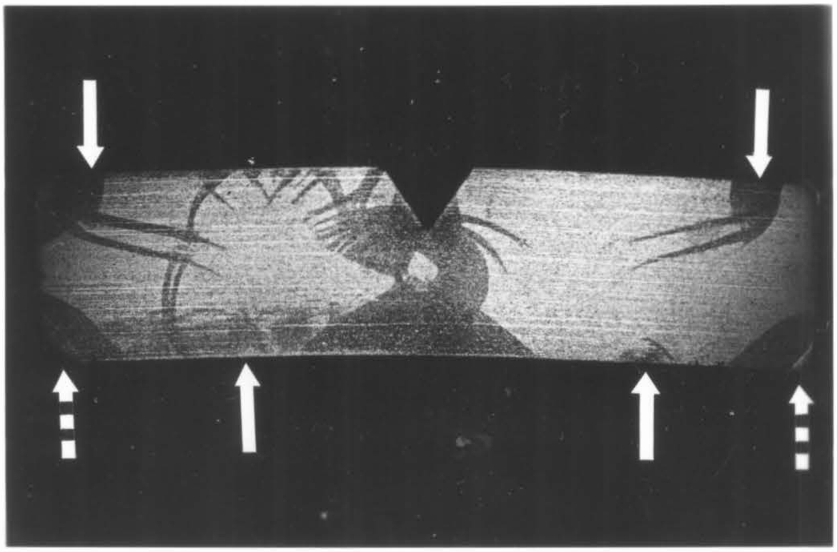

Fig. 40. Plastic spikes indicative of discontinuous yielding. The specimen was loaded quasi-statically in bending at the points indicated by the arrows. 4X.

strain) of a notched bar loaded slowly at room temperature in unsymmetrical four-point bending for use as a test piece to develop the nitriding and etching technique for revealing plastic material in this steel. The four solid arrows show the primary loading points. The two dashed arrows show where additional loading occurred when the ends of the bent specimen touched the supporting anvil. The blotchy stains along the left side of the bottom edge were probably caused by poor specimen handling procedures.

The plastic spikes shown in Fig. 40 have been idealized as shown in Fig. 41a for the purpose of studying the stress state discontinuity at the plastic-elastic interface. The slip lines in the plastic spike are assumed to make equal angles, $\pm\theta$, with the two sides of the spike. The plastic strain and the maximum shear stress are assumed to be constant throughout the plastic spike. If the plastic strain is viewed as being the result of the displacement of edge dislocations, as shown in the right-hand portion of the spike in Fig. 41a, then the condition of constant plastic shear strain implies that there is no net accumulation of edge dislocations of one sign in any volume element in the plastic spike. Thus the positive edge dislocations that have made a net displacement to the left must have accumulated at the plastic-elastic interface, as shown in Fig. 41a. (The dislocations must not have moved on across the interface, by definition of the elastic region there.)

An analysis of the stress discontinuity at the plastic-elastic interface is presented in Appendix IV. The analysis is based on the model described in the preceding paragraph and is applied to the case

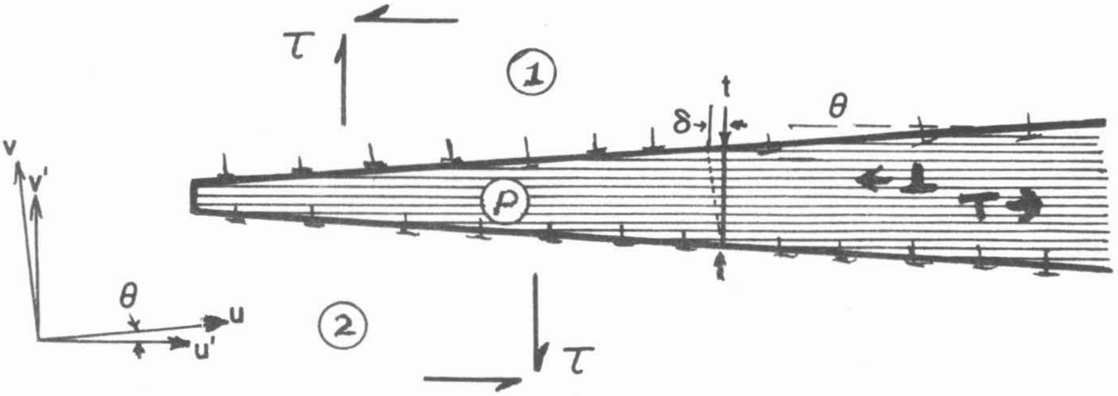

a. Schematic diagram of net dislocation distribution in plastic spike resulting from applied shear stress τ. Parallel lines represent slip lines in the plastic spike. The u axis is parallel to the plastic-elastic interface. The u' axis is parallel to the slip lines. Regions ① and ② are elastic.

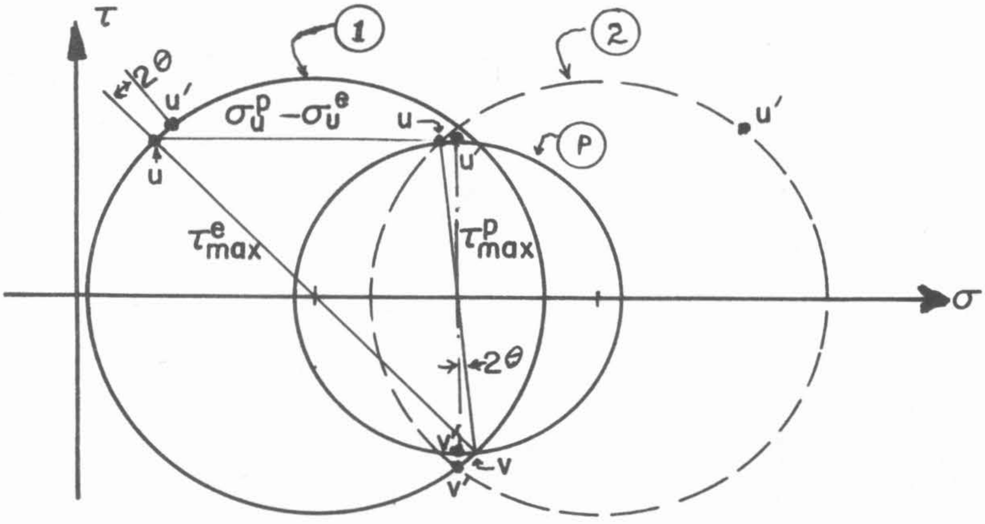

b. Mohr's circles for the stress states in the plastic spike, Ⓟ, and the two elastic regions, ① and ②, shown in part a. Points marked with u or v apply to the Ⓟ-① interface, only. Values of $\sigma_{v'}$ in the two elastic regions are nearly, but not exactly, equal for small values of 2θ.

Fig. 41. Stress state discontinuity at the plastic-elastic interface on the boundary of a plastic spike.

of plane strain where the elastic part of the strain component perpendicular to the plane of Fig. 41a is a constant and the plastic part of this strain component is zero. The accumulated dislocations at the interface result in a discontinuity in the normal stress component tangent to the interface of the amount

$$\sigma_u^e - \sigma_u^p = -\frac{G\gamma \sin 2\theta}{(1-\nu)} \qquad [8.1]$$

where the u-axis is parallel to the interface, σ_u^e and σ_u^p are the normal stress components tangent to the interface in the elastic and plastic regions, respectively, G is the shear modulus, ν is Poisson's ratio, γ is the plastic shear strain immediately adjacent to the interface and is equal to δ/t in Fig. 41a, and θ is the angle between the slip lines shown in Fig. 41a and the interface (θ is taken as positive for the interface between regions Ⓟ and ① in Fig. 41a).

The stress state on the elastic side of the interface can be calculated with the aid of Mohr's circles if the stress state in the plastic region and the discontinuity, $\sigma_u^e - \sigma_u^p$, are known. This construction is shown schematically in Fig. 41b. Assume that the stress components on the u and v faces of a volume element are known in the plastic region, Ⓟ . The stress components τ_{vu} and σ_v are equal on the two sides of the interface because of continuity of the normal stress component perpendicular to the interface and of the shear stress component tangent to the interface. The other end of the diameter of the Mohr's circle representing the stress state on the elastic side of the interface is located by adding ($\sigma_u^e - \sigma_u^p$) to

σ^p_u, τ^p_{uv} , as shown in Fig. 41b.

The value of the maximum shear stress on the elastic side of the plastic-elastic interface can be calculated easily by considering the geometry of the Mohr's circles in Fig. 41b:

$$(2\tau^e_{max})^2 = (\sigma^p_u - \sigma^e_u)^2 + (2\tau^p_{max})^2 + 2(\sigma^p_u - \sigma^e_u)(2\tau^p_{max})\sin 2\theta \qquad [8.2]$$

where τ^e_{max} and τ^p_{max} are the values of the maximum shear stress on the elastic and plastic sides of the interface. Alternatively, the magnitude of the plastic shear strain component causing a maximum shear stress intensification of $\tau^e_{max}/\tau^p_{max}$ across the interface is given by

$$\gamma = \pm \frac{(2\tau^p_{max})(1-\nu)}{G}\left\{\sqrt{1 + \frac{(\tau^e_{max}/\tau^p_{max})^2 - 1}{\sin^2 2\theta}} - 1\right\} \qquad [8.3]$$

The plastic shear strain, γ , involved in equations 8.1 and 8.3 is the algebraic sum of the shear strains caused by slip on the two orthogonal sets of slip planes, not just the one set of slip planes shown in Fig. 41a.

Equations 8.1 through 8.3 are still valid if the dislocations accumulate in a thin film of thickness t at the plastic-elastic interface, provided t is small compared to tangential distances over which γ , θ , t or ϕ change appreciably. These equations then predict the difference in the stress states on the two sides of the thin film. If the film is viewed as a region in which the yield stress, σ_{yd} , of the plastic material varies continuously between $2\tau^p_{max}$ and $2\tau^e_{max}$ at the plastic and elastic surfaces, respectively, then the direction of the slip line field in this region can be calculated from equations II-10 and

II-11 of Appendix II. This calculation is performed in Appendix IV. The calculation predicts that θ, the angle between the negative slip-line direction and the planes of constant yield stress in the boundary film, is related to the yield stress by

$$\sigma_{yd} \cos 2\theta = \text{constant} \qquad [8.4]$$

Inspection of the Mohr's circle used in the derivation of equation 8.2 shows that equation 8.4 is equally valid for finite discontinuities in the value of $2\tau_{max}$. In fact, $\frac{1}{2}\sigma_{yd} \cos 2\theta$ is just equal to the (constant) value of the shear stress component tangent to the plastic-elastic interface.

The stress state in the elastic material at the tip of the plastic spikes shown in Figs. 40 and 41a is not easily deduced through the analysis described above. The stress states on the two sides of the plastic spike, ① and ② in Fig. 41a, are different, as is shown by their Mohr's circles in Fig. 41b. Thus the stress states in regions ① and ② must change toward a common state at the plastic spike tip. If the plastic spike tip were infinitely sharp, a stress singularity could exist there. Actual observation of the specimen shown in Fig. 40 suggests that the plastic spike, when defined as consisting of material that has plastically strained a sufficient amount to be etched darker by Fry's reagent, has a tip diameter of about two or three grain diameters. This bluntness of the plastic spike would seem to preclude a stress singularity unless the very tip of the spike has plastic strains that are too small to be sensitive to Fry's reagent.

One model for a blunt tip for the plastic spike would be an approximately square end, as shown in Fig. 41a. The square end would be parallel to a set of slip lines (perpendicular to the set of slip lines depicted in Fig. 41a) so there would be no stress discontinuity across it, according to equation 8.1. This portion of the plastic-elastic interface would constitute a "tilt boundary" separating regions of material which have rotated with respect to each other.

The presence of a boundary layer through which the yield stress of the material is changing continuously may permit a continuous transition from stress state ① to stress state ② near the plastic spike tip.

These models of the material properties and plastic-elastic interface configuration at the plastic tip may be entirely inappropriate since they are based on continuum mechanics of a homogeneous material and smooth idealizations of the plastic-elastic interface. But the plastic-elastic interface is known to be bumpy enough to follow grain boundaries and the material is not homogeneous on the grain diameter scale.

An estimate of the magnitude of the stress discontinuity at the plastic-elastic interface is of interest. Suppose that the maximum shear stress on the plastic and elastic sides of the spike boundaries of Fig. 40 have the values $2\tau^{p}_{max} = \sigma_{LY} = 34,500$ lb/in.^{2} and $2\tau^{e}_{max} = \sigma_{UY} = 48,000$ lb/in.^{2}. These numerical values for the upper and lower yield stresses are taken from Table 3. (The Mohr's circles in Fig. 41 have been scaled to these values for $2\tau^{e}_{max}$ and $2\tau^{p}_{max}$.) The included angle, 2θ, of the plastic spikes has been measured on Fig. 40 as $\tan 2\theta \approx 0.1 \approx \sin 2\theta$. Using $G = 11.5 \times 10^6$ lb/in.^{2} and $\nu = 0.3$ in equation 8.3, the calculated value of the plastic shear strain is $\gamma \approx 0.02$. The Lüder's strain, ε_L, determined on an unnotched specimen of this material in tension, has a value $\varepsilon_L \approx 0.02$, or $\gamma_L = 2\varepsilon_L \approx 0.04$. Thus the calculated value of the plastic strain in the plastic spikes, $\gamma \approx 0.02$, is of the order of magnitude of, but somewhat smaller than, the value of the Lüder's strain. The upper yield stress is certainly an upper limit for the value of $2\tau^e_{max}$, so this calculation implies that the plastic strain in the spikes is smaller than the Lüder's strain and, therefore, that the maximum shear stress in the plastic spike is somewhat less than $\frac{1}{2}\sigma_{LY}$.

The fact that σ_{LY} and σ_{UY} can be associated with $2\tau^p_{max}$ and $2\tau^e_{max}$, and the resulting calculated value of the plastic shear strain in the spikes shown in Fig. 40 is just slightly less than the Lüder's strain value may be fortuitous. Actually, the maximum shear stress in the elastic regions must be less than $\frac{1}{2}\sigma_{UY}$; otherwise small "islands" of plastic material would form ahead of the plastic-elastic interface. However, the plastic-elastic interface is rather smooth, usually following grain boundaries, and occasionally passing through grains. The maximum shear stress in the elastic region is thought to lie in the range $\sigma_{LY} \lessapprox 2\tau^e_{max} < \sigma_{UY}$. The actual values of the stresses in the elastic region and in the plastic spikes will have to be deduced from calculations of the stress distribution in specimens whose loading is known and which have also been examined for plastic enclave sizes and shapes. Since the stress-strain behavior of the material is not actually known for the small plastic strains encountered in the plastic regions, specimens subjected to several load intensities would have to be examined for plastic enclave development and the stress calculations would have to be repeated for different assumed stress-strain relations until consistent values of the stress discontinuity across the plastic-elastic interface were obtained. This study has not been performed for this thesis.

The stress state discontinuity across the plastic-elastic interface near the tip of the plastic wedge shown in Fig. 29 can also be examined qualitatively with the analysis discussed earlier in this section. The slip-line field in the wedge tip has been idealized by straight lines, as shown in Fig. 42a. The dislocations shown in Fig. 42a near the intersection of the slip lines with the plastic-elastic interface show the sign of the dislocations which are expected to accumulate at the interface as a result of plastic straining in region Ⓟ. Slip on the two slip-line systems is seen to have an additive effect on the discontinuity in the normal stress component tangent to the plastic - elastic interface, σ_u. The dislocations accumulated at the interface also have a displacement component perpendicular to the interface that results in a tilt boundary, or a relative elastic rotation of volume elements on the two sides of the plastic-elastic interface. Slip on the two perpendicular slip-line systems partially cancel each other's contribution to the strength of the tilt boundary. However, slip along the slip lines which are more nearly perpendicular to the plastic-elastic interface make a larger contribution to the tilt boundary per unit of plastic shear strain. Conversely, rotation of volume elements in the elastic region is expected to be accommodated primarily by slip on the slip lines which are more

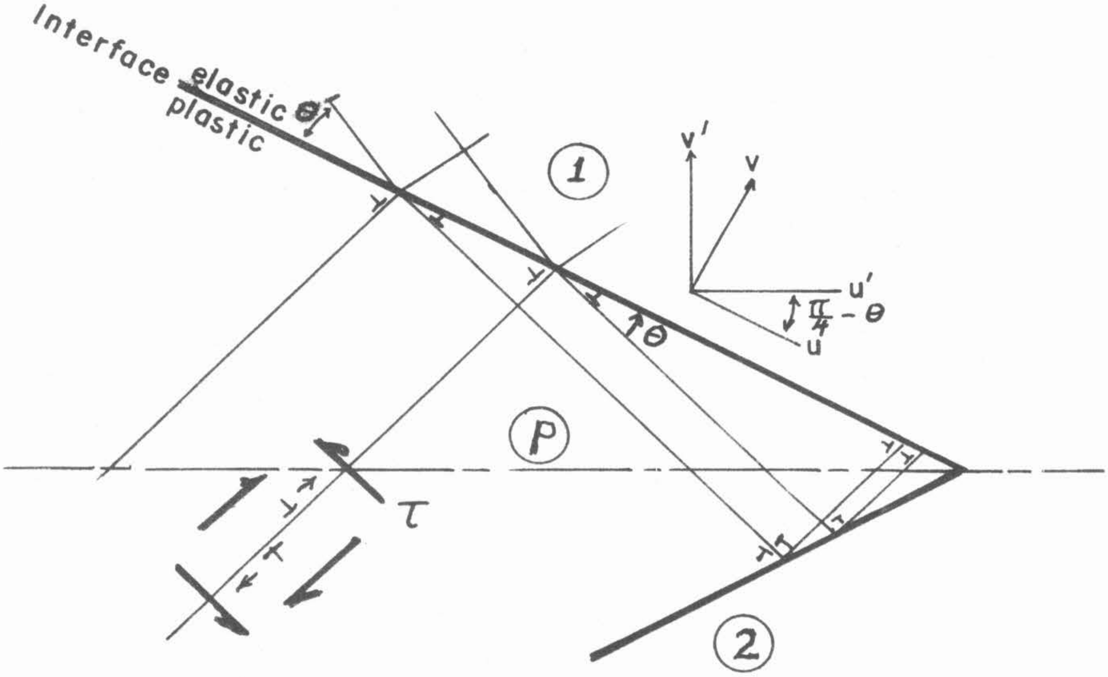

a. Schematic diagram of slip lines and plastic strain discontinuity at a plastic wedge tip boundary.

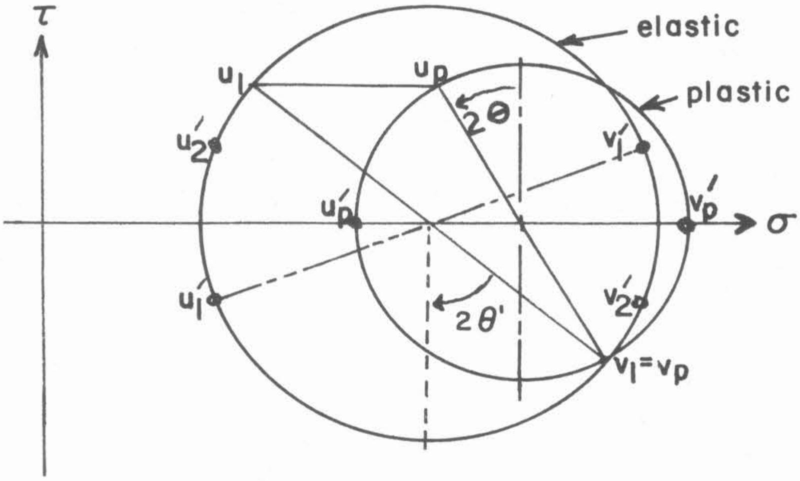

b. Mohr's circle representations of the stress states in the plastic wedge tip and the adjacent elastic material shown in part a.

Fig. 42. Stress state discontinuity near the tip of a wedge-shaped plastic enclave.

nearly perpendicular to the plastic-elastic interface.

When the assumption is made that $2\tau^{e}_{max} = \sigma_{UY}$ and $2\tau^{p}_{max} = \sigma_{LY}$ on the elastic and plastic sides of the interface, respectively, the stress states of regions ① and Ⓟ in Fig. 42a are represented by the large and small diameter Mohr's circles in Fig. 42b. The point labeled $v_1 = v_p$, at the intersection of the Mohr's circles, represents the stress components on an element of area parallel to the plastic-elastic interface, and the points labeled u_1 and u_p represent stress components on the elastic and plastic sides of the interface acting on elements of area that are perpendicular to the interface. These points were used in the construction of the Mohr's circle for the elastic region ①, assuming the Mohr's circle for the plastic region Ⓟ to be known from slip-line field theory.

The stress components in all three regions, ①, Ⓟ and ②, are also shown in Fig. 42b referred to the u' and v' axes. Again, the stress states in the elastic regions ① and ② on the two sides of the plastic wedge tip are found to be different from each other and the exact nature of the stress state at the very tip of the wedge is unknown. If the wedge tip is, indeed, sharp, a stress singularity could exist there mathematically. The photomicrograph of a plastic wedge in Fig. 26 suggests that the material near the wedge tip has responded less intensely to Fry's reagent than in regions closer to the notch surface. Thus the plastic strain, and the yield stress, of the material in the wedge tip may vary in such a way as the tip is approached that the stress states in regions ① and ② converge continuously to a common, finite state at the wedge tip.

The value of θ shown in Fig. 42a has been calculated from measurements of the wedge tip included angle in Fig. 26 and other 35X enlargements of the plastic enclaves shown in Fig. 24. The values of the wedge tip included angle, $90^\circ - 2\theta$, are given in Table 3. The average value of 2θ is about 17°. Assuming, again, that $2\tau^{e}_{max} = 48,000$ lb/in.^{2} and $2\tau^{p}_{max} = 34,500$ lb/in.^{2}, the value of the plastic strain in the wedge tip calculated by equation 8.3 is $\gamma \approx 0.002$. This value for γ is an order of magnitude smaller than the Lüder's strain for this material. Figure 29 shows that the slip lines actually curve and become more nearly parallel to the plastic-elastic interface at points farther from the wedge tip. The calculated value of γ would be larger than 0.002 as θ becomes smaller.

The applications of the stress discontinuity calculations at the plastic-elastic interfaces for the plastic spikes shown in Fig. 40 and the plastic wedges shown in Fig. 24 have led to estimated maximum values of the plastic shear strain in the plastic enclaves. The actual values of the plastic strain and, therefore, of the stress discontinuity across the plastic-elastic interface have not been determined, as was mentioned earlier. The important concept is that the magnitude of the plastic shear strain changes very rapidly at the plastic-elastic interface and that the value of the maximum shear stress on the two sides of the interface necessarily experiences a finite change in magnitude and direction, the amount of the change being dependent upon the magnitude of the plastic strain and upon the angle between the slip lines and the interface. Furthermore, when the plastic strain is of the appropriate sign to result in positive work done by the applied shear stress, the maximum shear stress on the elastic side of the plastic-elastic interface has a larger value than the maximum shear stress in the plastic region. It has also been shown that the presence of a thin boundary layer through which the yield stress of the material changes continuously does not alter the difference in stress states on the two sides of the boundary layer from what the stress states would have been if the boundary layer had had zero thickness.

Therefore, in regions where the boundary layer at a plastic-elastic interface is thin compared to tangential distances over which γ, θ, t or ϕ change appreciably, continuum mechanics methods may be used to calculate the stress distributions in the elastic and plastic regions. The boundary conditions on the stresses at the plastic-elastic interface must consist only of continuity of the normal stress component perpendicular to the interface and of the shear stress components tangent to the interface. The other stress components are not in general continuous across the plastic-elastic interface in mild steel. The maximum shear stress criterion for elastic material becoming plastic will have a value $\tau_{max} = \frac{1}{2}\sigma_{UY}$ (Tresca yield criterion) in a volume element which is completely surrounded by elastic (perhaps microstrained) material and a lower value, $\frac{1}{2}\sigma_{LY} \lessapprox \tau_{max} < \frac{1}{2}\sigma_{UY}$, in a volume element which is bounded on some sides by plastically strained material. The value of τ_{max} may be a function of θ and of the solid angle over which the elastic volume element is bounded by plastically strained material. One difficulty that must be overcome before a plastic-elastic stress analysis can be performed is in establishing a criterion and a computational means for determining the slip-line field in those regions of a plastic enclave where both sets of slip lines do not intersect a free-displacement surface, as in region Ⓟ of Fig. 42a. The plastic-elastic interface will be very dependent upon the slip-line field through θ and equation 8.1. This fact will impose a certain smoothness to the plastic enclave boundaries.

8.4 Factors Affecting the Shape of Plastic Enclaves

The stress discontinuity at the plastic-elastic interface in mild steel may be a prime cause for the discrepancy between the plastic enclave shapes determined experimentally for this thesis and the shape predicted theoretically by Hendrickson, Wood and Clark (27). Then the discrepancy between the experimental and theoretical enclave shapes could be attributed in part to inadequate knowledge and incorporation of the properties of the material in the stress analysis, above and beyond any other deficiencies in the analysis technique.

The experimentally determined and the theoretically predicted (Hendrickson et al. (27)) plastic enclave shapes have been compared schematically in Fig. 27. The boundary of the experimentally determined wedge shaped plastic enclave is shown in Fig. 29, as being nearly parallel to the slip-line field. Thus the plastic enclave lobes that are predicted theoretically to extend in the axial direction of the specimen must have an interface with the elastic region that makes a large angle with the slip lines in some places and is tangent to the slip lines at some point, such as is shown by points ② and ① in

Fig. 43. The solid plastic-elastic interface in Fig. 43 represents the experimentally determined plastic enclave boundary and the dashed interface represents the boundary shape if a plastic lobe were to begin to develop in the direction predicted by Hendrickson et al.

The actual formation of the plastic lobe extension in Fig. 43 is <u>not</u> favorable in this mild steel in which stress discontinuities can exist across a plastic-elastic interface. Equation 8.1 (or 8.3) predicts that only a very small plastic strain can exist in the neighborhood of region ② in Fig. 43 because of the large angle, θ , between the interface and the slip lines. Expressed as an inequality, equation 8.3 predicts that

$$|\gamma| \leqslant \left| \frac{2(1-\nu)}{G} \; \frac{\tau^{e}_{max}}{\sin 2\theta} \right| \qquad [8.5]$$

or $|\gamma| < 0.003$ for $2\tau^{e}_{max} = 48,000 \text{ lb/in.}^2$ and $2\theta = \pi/2$. The displacement field which results in such a small value of the plastic strain at point ② in Fig. 43 is not likely to accommodate much larger strains at point ① . Since the plastic-elastic interface at point ① is parallel to the slip lines, equations 8.1 and 8.2 predict that $\tau^{e}_{max} = \tau^{p}_{max}$. The value of the yield stress of material that has plastically strained by an amount $|\gamma| < 0.003$ is probably appreciably less than the value of the lower yield stress, so $2\tau^{e}_{max} = 2\tau^{p}_{max} < \sigma_{LY}$. This small value of the maximum shear stress on the elastic side of the plastic-elastic interface is apparently too small to cause plastic deformation, so the virtual plastic lobe depicted in Fig. 43 will not develop in such a way that any part of the plastic-elastic interface is parallel to a slip-line direction. (However, a plastic-elastic interface <u>might</u>

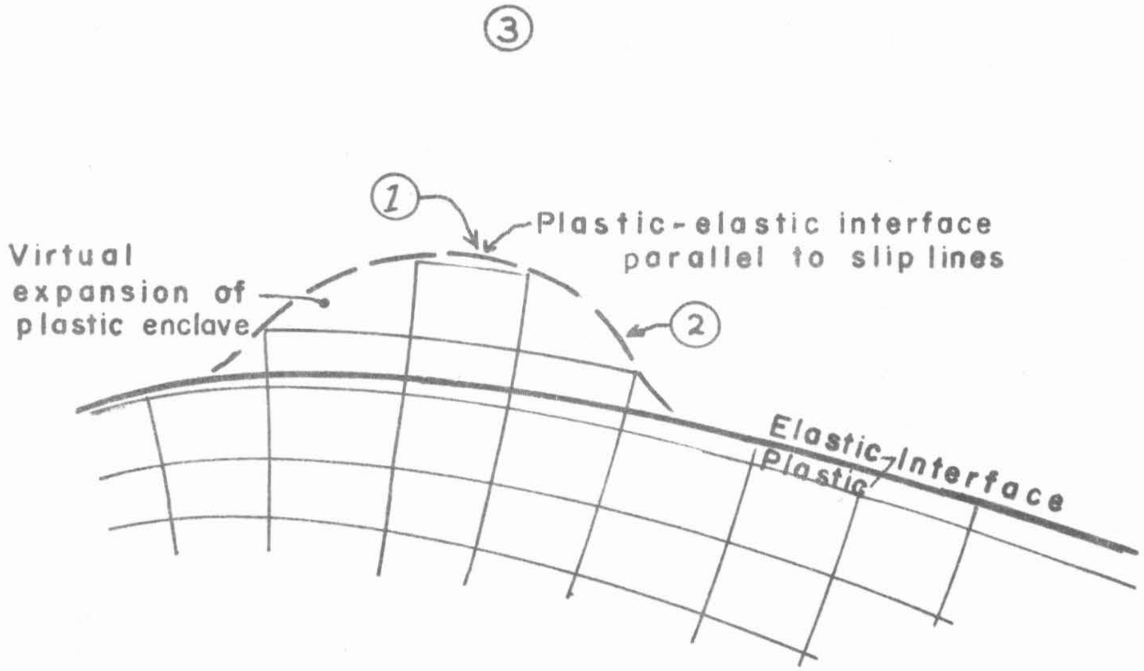

Fig. 43. Relation between plastic enclave boundary and the slip-line field.

be able to be parallel to a slip line when the plastic strain has approximately the value of the Lüder's strain.)

This restriction on the growth of the plastic enclave permits a large region of elastic material in the neighborhood of feature ③ of Fig. 43 to experience a very large shear stress. Figure 24c shows that the maximum shear stress in this region may become so large that plastic spikes (cones, in axial symmetry) similar to those seen in Fig. 40 grow out from the plastic wedge in such a manner that the only plastic-elastic interface parallel to a slip line is located at the spike tip, where the stress state may be quite complex.

The plastic wedge tip is also apparently a manifestation of the necessity for preventing a plastic-elastic interface from becoming parallel to slip lines, especially in a region where the plastic strain is small.

The sharpness of the wedge tip must be determined by displacements at the plastic-elastic interface (dictated by strains and rotations in the elastic material), plastic strains, and strain hardening effects and also θ, equations 8.1 and 8.2, and the yield criterion on the elastic side of the interface. It is anticipated that the plastic wedge shape would be markedly affected by a reduction in the magnitude of the yield point instability. Thus, the plastic enclaves in a mild steel with a sufficiently large grain size that an upper yield stress cannot be detected might not contain sharp boundary discontinuities such as the wedge and spike tips.

The onset of general yield also appears to be sensitive to the upper and lower yield stress instability. The large grain size specimen of Fig. 25-b shows more extensive general yield patterns than the small grain size specimen of Fig. 24-c. Note that σ_{nom}/σ_{LY} is smaller for the large grain size specimen, but that σ_{nom}/σ_{UY} is larger.

These observations strongly suggest that at least part of the failure of plastic enclaves predicted by theoretical analyses to have the same general shape as the enclaves determined experimentally in mild steel is that the instability associated with the upper and lower yield stresses has not been adequately described as a property of the material and subsequently employed in the stress analyses. Care must be taken that the stress analysis technique does not require all stress components to be continuous across the plastic-elastic interface. The appropriate description of the yield instability would be used in the stress analysis as a criterion for locating the plastic-elastic interface.

8.5 Conjectures on the Yield Behavior of a Mild Steel

A description of the yielding process at and near the plastic-elastic interface in terms of the crystallographic microstructure of the material will be attempted in this section. The importance to the yield instability of such mechanisms as dislocation multiplication and the stress dependence of dislocation velocity, as discussed by Johnston and Gilman (49) and applied to mild steel by Hahn (50), will not be considered explicitly here, even though they may play a dominant role in yielding in some grain size ranges, as has been suggested by Worthington (51) for yield in 3 percent silicon iron.

Zener (13) has proposed that the blockage of micro-slip bands by grain boundaries results in large stress concentrations at the tip of the slip band such that slip in the next grain, or a microcrack near the grain boundary, could be nucleated by the high stress fields. Zener envisioned the crack nucleus as resulting from the coalescence of edge dislocations gliding in the micro-slip band and piling up against the grain boundary. The stress intensification near the slip band tip is of the order of $(L/\ell)^{1/2}$, where L is the length of the dislocation pile-up (the half-length of a symmetrical micro-slip band) and ℓ is the distance from the tip of the slip band to the point where the stress is being calculated. Petch (24) and Cottrell (16) have explicitly identified the length of the dislocation pile-up with the semi-diameter of a grain to "explain" the relation

$$\sigma_y = \sigma_i + k\, d^{-1/2} \qquad [8.6]$$

where σ_y was taken to be the lower yield stress and d is the grain diameter, in terms of the "friction stress," σ_i, and k, an index of the stress intensity at a characteristic distance from the tip of the micro-slip band.

Russell, Wood, and Clark (52) have observed that the relation given by equation 8.6 applies to both upper and lower yield stress data for mild steel, but with a very much smaller value of σ_i and a 1.8 times larger value of k for their upper yield stress data. Upper and lower yield stress measurements on Armco iron by Sylwestrowicz and Hall (53) may be fitted to equation 8.6, resulting in a ratio $k_{(UY)}/k_{(LY)} = 1.5$. These upper and lower yield stress data (52, 53) are plotted against the inverse of the square root of the average grain diameter in Fig. 44 to illustrate the relation expressed by equation 8.6.

If k is actually associated with a shear stress intensity in the vicinity of the micro-slip band tip, it should be reasonable to presume that the value of k should be the same for both the upper and the lower yield stress data if d is proportional to the length of the dislocation pile-up. The k's can be made equal by associating a larger distance than the grain diameter with d, the length of the micro-slip band, at the lower yield point and/or a stress concentration such that the stress level in the vicinity of the propagating Lüder's band front is larger than the average stress on the cross section of the specimen. A factor of $\sqrt{2} \approx 1.4$ difference in the values of for the upper and lower yield stresses would be expected if the dislocation pile-up length were equal to the semi-diameter of the grains for the upper yield stress and the <u>entire</u> grain diameter for the lower yield stress.

A difference in the lengths of the dislocation pile-ups might be expected if grain boundaries act as barriers to micro-slip bands prior to the upper yield stress, while boundaries between two grains in the plastic region have lost their strength.

Russell, Wood, and Clark (52) have proposed a model for the initiation of gross yielding at the upper yield stress that characterizes micro-slip band break-through at a grain boundary by local displacement of the boundary from the low energy position saturated with interstitial solute atoms to an adjacent site free from the cloud of solute atoms. This displaced section of grain boundary could then act

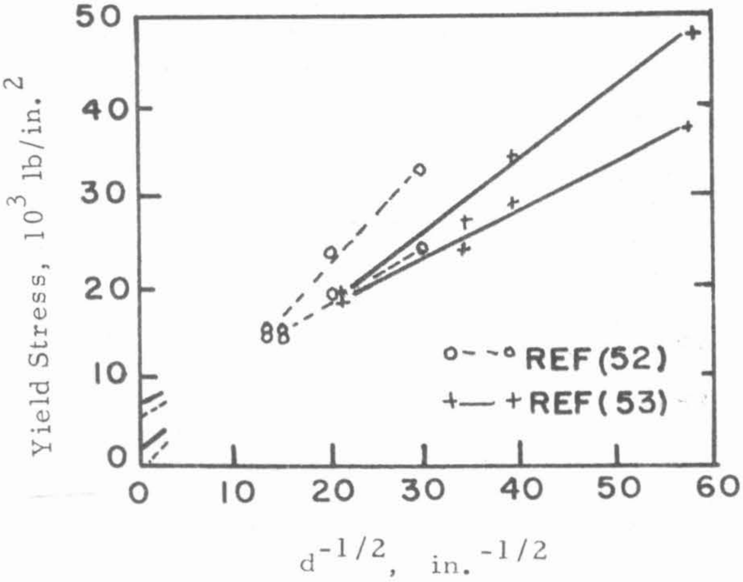

Fig. 44. Upper and lower yield stresses vs. inverse square root of average grain diameter. Data from Russell, Wood and Clark (52) and Sylwestrowicz and Hall (53).

as a source of unpinned dislocations that could be induced to slip in the next grain. Dingley and McLean (54) have observed that the flow stress of low-carbon iron is a function of the dislocation density and is otherwise independent of the grain size. They concluded that grain boundaries have no direct strengthening effect after the upper yield stress has been passed. However, there is an indirect strengthening effect of grain boundaries since the dislocation density at a given plastic strain is higher for smaller grain sizes.

Activity on micro-slip bands near the plastic-elastic interface at the lower yield stress is depicted schematically in Fig. 45. Grains Ⓐ and Ⓑ are in the plastic region and the boundary between grains Ⓑ and Ⓒ is part of the plastic-elastic interface. It is presumed that a large number of slip systems ① are active in grain Ⓐ as a result of strain continuity requirements at each of the interfaces which grain Ⓐ shares with about fourteen adjacent grains. It is also assumed that most of the plastic strain in grain Ⓑ is caused by dislocation activity on slip system ②, although some slip may be occurring on slip plane ③ to satisfy strain continuity conditions at the boundary between grains Ⓐ and Ⓑ. Note that dislocations distributed along slip system ③ could act as a "forest" impeding slip on system ②, thereby causing a larger friction stress to be associated with stress intensifying effects from dislocation pile-ups at the tip of micro-slip band ②. A dislocation array on slip system ② can be piled up against the strong boundary between grains Ⓑ and Ⓒ but not against the weak boundary between grains Ⓐ and Ⓑ. Thus, the

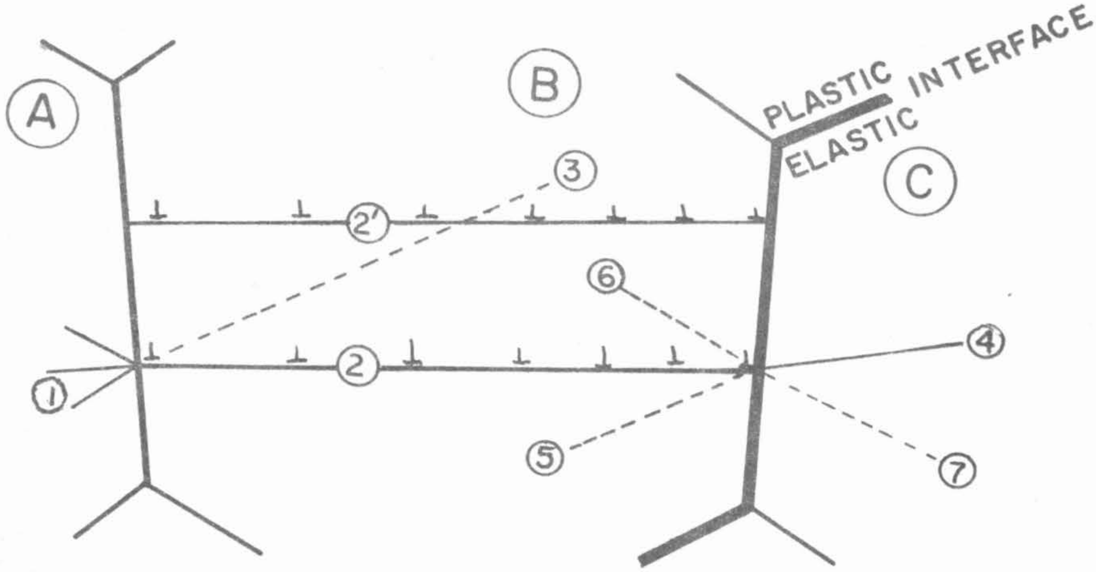

Fig. 45. Schematic representation of micro slip band activity in grains near a plastic-elastic interface.

dislocation pile-up length should be associated with approximately a full grain diameter at the lower yield stress rather than the semi-diameter, as at the upper yield stress.

The "other end" of the micro-slip band associated with slip system ② in grain Ⓑ probably dies off gradually into grains even farther from the plastic-elastic interface than grain Ⓐ as the flow stress of successive grains farther into the plastic region increases because of strain hardening. In fact, the dislocations of the opposite sign from those piled up on ② against the boundary between Ⓑ and Ⓒ must ultimately be effectively piled up at the other end of the slip line against another plastic-elastic interface or be swept out at a displacement-free surface. The dislocation pile-up strength on slip system ② will be affected by the ease with which the dislocations of the opposite sign have been swept back into the plastic region. Therefore, stress requirements for the propagation of yielding after the upper yield stress has been passed are expected to be dependent upon the number of grains penetrated by the slip lines intersecting the plastic-elastic interface. A slip line may need to penetrate about three or four grains into the plastic region before dislocation pile-ups on the slip line at the plastic-elastic interface could behave in a manner similar to the behavior of dislocation pile-ups at the lower yield stress.

The stress-strain state of geometrically similar notched specimens of mild steel subjected to identical surface stresses is expected to be dependent on the scale size of the specimens after the formation of local plastic enclaves because of the importance of the effective micro-slip band length, as discussed above. The ratio of the micro-slip band length to the grain diameter or to the grain diameter at which the upper and lower yield stresses are just equal may be important parameters in the stress-strain state in plastic regions.

The slip band activity has been greatly simplified in the above discussion. Grain Ⓑ is not expected to have just a single slip band ②, but a set of parallel ones depicted by (2'), as has been observed at higher plastic strain levels by Ewing and Rosenhain (55). A single slip band ② would result in plastic displacements near a grain boundary that would be so non-uniform that slip on glide planes of randomly oriented adjacent grains could not possibly match the plastic displacements along the entire boundary. By distributing the plastic displacements over a large number of parallel bands, the concept of a uniform plastic strain becomes more realistic. This fairly uniform plastic strain can then be accommodated by sufficiently homogeneous slip on an appropriate number of other slip systems on both sides of the boundary.

The presence of many parallel micro-slip bands does not prevent stress intensifications from occurring at the edges of the slip bands, although the strength of the stress intensifications is likely to be affected by the spacing of the slip bands relative to the effective length of the dislocation pile-ups. The stress intensifying effect of parallel slip bands should be somewhat analogous to that of shallow notches, as considered by Neuber (28).

Although slip on five independent slip systems is necessary in general to produce an arbitrary plastic strain, local continuity of all five plastic strain components at grain boundaries, edges or corners requires slip on just $(5N-4)$ independent slip systems to accommodate the strain caused by slip on any one of the slip systems in the N adjacent grains. (Independent slip systems in this context implies that the plastic strain resulting from homogeneous slip on any one of the slip systems cannot be matched by slip on fewer than five slip systems in each of the grains, separately.) Thus, the strain produced in grain Ⓑ of Fig. 45 by a slip system on slip plane ② could be accommodated at the boundary between grains Ⓑ and Ⓒ by an appropriate amount of slip on a total of five independent slip systems among the two grains. This need involve only three slip planes whose normals are non-coplanar, such as ④, ⑤, and ⑦, or even ④, ⑦, and ② where a new slip direction is activated on slip plane ②. Furthermore, some of these strains may be small enough to be accommodated elastically at low plastic strain levels. Strain hardening in grains farther into the plastic material from the plastic-elastic interface is expected to result from both an increase in the density of interacting dislocations and from an increase in the number of intersecting active slip systems as the total plastic strain becomes larger and more macroscopically uniform.

Finally, the average stress levels acting on the micro-slip bands must be related to the macroscopic features of the plastic strain, the angle that the slip lines make with the average plastic-elastic interface surface, and the maximum shear stress increase on the elastic side of the interface, as discussed in Section 8.3. Just what role the high level of the maximum shear stress plays on the elastic side of the plastic-elastic interface is not clear, although its importance has been argued in Section 8.4. Does this imply that stress intensifications at the tips of micro-slip bands on the elastic side of the plastic-elastic interface are important in helping to overcome the pre-yield strength of a grain boundary? Regardless of the details of the operative mechanisms for plastic flow, it seems to be evident that geometrical similitude of stress-strain states cannot be retained in mild steel once local plastic enclaves have developed because of the dependence of micro-slip band lengths on the grain size of the material.

IX. SUMMARY AND CONCLUSIONS

It was found to be possible to deduce some characteristics of the yield behavior of a silicon semi-killed mild steel in small plastic enclaves after a surface nitriding treatment was developed which rendered the plastic material sensitive to Fry's reagent. The shape of the plastic enclaves revealed by this new etch technique differed from the shape predicted by existing plastic-elastic stress analyses; the boundaries of the plastic enclaves tended to be parallel to the slip-line field and sharp reentrant angles in the elastic regions were observed.

An analysis of the stresses and strains on both sides of the plastic-elastic interface strongly suggests that plastic strains, γ_p, as large as the Lüder's strain can exist in the plastic region immediately adjacent to the plastic-elastic interface. This plastic strain discontinuity at the interface causes the value of the maximum shear stress, τ_{max}, to be <u>larger</u> on the <u>elastic</u> side of the interface. The ratio of $\tau^e_{max}/\tau^p_{max}$ increases with increasing values of γ_p and $\sin 2\theta$, where θ is the angle between the plastic-elastic interface and a slip line.

The discontinuous yield nature of steel requires that a stress analysis technique not impose unwarranted constraints on the continuity of stresses across a plastic-elastic interface. In particular, continuity of all of the stress components is an unsuitable condition at the interface.

The major cause of the discrepancy between the shapes of the plastic enclaves observed experimentally and those predicted theoretically is the failure to employ an appropriate criterion for locating the plastic-elastic interface in the stress analysis. Such a criterion is expected to consist of a relationship between θ and γ_p at the plastic enclave boundary. This relation between θ and γ_p would be a property of the material.

A suggestion is advanced that the quantity denoted by "d" in the Hall-Petch equation for the dependence of the yield stress on the grain size, $\sigma_{yd} = \sigma_i + k\, d^{-1/2}$, is probably related to the semi-grain-diameter for upper yield stress data and to a characteristic length approximately equal to the full grain diameter at the lower yield stress.

An approximate stress analysis employing slip-line theory in the plastic region (Tresca yield criterion; plane strain, constant flow stress approximation) and using Neuber's solution for infinitely deep notches in elastic media for an estimate of the stresses in the central core has been developed for the notched specimens tested in this investigation.

Values of the flow stress in the plastic enclaves of the notched specimens have been correlated with lower yield stress data obtained from unnotched specimens for the dynamic tests by considering the velocity of the plastic-elastic interface.

A transition to higher fracture load values at lower loading rates occurred at the onset of general yield in the notched specimens of ASTM grain size No. 8 1/4.

The maximum tensile stress in those specimens which fractured before the onset of general yield was calculated with the aid of the approximate stress analysis developed in this investigation. The values of σ_{maxf} ranged from 122, 000 lb/in.^{2} at the tip of large plastic enclaves to 157, 000 lb/in.^{2} at the tip of the next to the smallest plastic enclave. This calculated value of σ_{maxf} = 122, 000 lb/in.^{2} is considerably smaller than the value of 210, 000 lb/in.^{2} previously reported by Hendrickson, Wood and Clark (27). The difference between these calculated values for σ_{maxf} is a result of the use of a different stress analysis in this investigation.

The maximum normal stress component at a point 11.1 x 10^{-3} in. from the tip of the wedge-shaped plastic enclave, toward the notch root, had a constant value of 118, 000 ± 4, 000 lb/in.^{2} for ten of the eleven small grain size notched specimens that fractured prior to general yield. <u>If</u> this is the point of fracture initiation, then the present data do not show a "size effect" upon the local fracture stress.

It is suggested that the true fracture criterion may be expressed as a locus of stress and plastic strain values. Part of an apparent geometrical scale "size effect" on a fracture stress may be caused by size effects on the plastic stress-strain relationships in small enclaves where micro-slip bands are restricted to lengths several times as long as the average grain diameter.

The occurrence of voids in the depth interval from 0.003 to 0.016 in. below the notch root in a static tensile test indicates that fracture nucleation by a fibrous mode may occur in a region of large plastic strain and moderately high tensile stress- not necessarily the region of maximum plastic strain at the notch root, where the tensile stress has a lower value.

Highly accurate calculations for the stress state in and near small plastic enclaves in a mild steel will have to await a quantitative description of the stress state discontinuity at the plastic-elastic boundary. Until such time when proper account can be taken of this property of the material, proposed brittle fracture initiation criteria are likely to be as strongly influenced by the stress analysis techniques as by any actual property of the material.

APPENDICES

I. TECHNIQUE FOR OBTAINING PHOTOMICROGRAPH OF CYLINDRICAL SURFACE

Photomicrographs of cylindrical surfaces were obtained with a Bausch and Lomb Metallograph with an inverted stage. Bright field illumination was employed. The cylindrical specimen was rolled at a constant rate along a track secured in the plane of focus of the objective. Light emanating from the objective was specularly reflected from the cylindrical surface in such a manner that the light striking those portions of the cylindrical surface which were nearly tangent to the track, and therefore, in focus, was reflected back into the objective to eventually form an image on the film. Those light rays which struck surfaces at a greater distance from the plane of focus, and, therefore, less nearly normal to the optical axis of the objective, were reflected to the side of the objective and did not expose the film. However, some dark field illumination occurs with this method, decreasing the contrast.

II. SLIP-LINE FIELD THEORY APPLIED TO NOTCHED SPECIMENS

The slip-line field theory presented by Hill (29) is directly applicable to a Tresca material in plane strain which plastically deforms when the maximum shear stress reaches a critical, constant value. The effects of axial symmetry and a non-constant yield stress upon the stress calculations will also be discussed in the following review and application of the slip-line field theory.

The coordinate systems to be used here are shown in Fig. 28. Cartesian coordinates, x, y, and z, will be used for plane strain, while cylindrical coordinates, r , θ , and z , will be used where axial symmetry is present. The z axis is in the direction of the applied tensile load in both systems.

The equilibrium equations in plane strain, in the absence of body forces, are:

$$\frac{\partial \sigma_y}{\partial y} + \frac{\partial \tau_{yz}}{\partial z} = 0 \qquad [\mathrm{II}\text{-}1]$$

$$\frac{\partial \sigma_z}{\partial z} + \frac{\partial \tau_{zy}}{\partial y} = 0 \qquad [\mathrm{II}\text{-}2]$$

For axial symmetry the equations become, in cylindrical coordinates,

$$\frac{\partial \sigma_r}{\partial r} + \frac{\partial \tau_{rz}}{\partial z} + \frac{(\sigma_r - \sigma_\theta)}{r} = 0 \qquad [\mathrm{II}\text{-}3]$$

$$\frac{\partial \sigma_z}{\partial z} + \frac{\partial \tau_{rz}}{\partial r} + \frac{\tau_{rz}}{r} = 0 \qquad [\mathrm{II}\text{-}4]$$

The yield criterion is

$$\tfrac{1}{4}(\sigma_z - \sigma_r)^2 + \tau_{rz}^2 = k^2 \qquad [\text{II-5}]$$

where $k = \frac{1}{2}\sigma_{yd}$ in simple tension for a Tresca material.

The three stresses in the meridian planes, σ_r , σ_z , and τ_{rz} , can be expressed in terms of three other quantities, k , p , and ϕ , with the aid of Mohr's circle. Consider a Mohr's circle of radius k (given by equation II-5), center at $-p$ (where $-p = \frac{1}{2}(\sigma_r + \sigma_z)$) and of an orientation such that the counter-clockwise angle between the z axis and the α direction is ϕ . The α and β lines,which are the directions of maximum shear stress, form a right-hand orthogonal pair (α to β) and contain the direction of the maximum tensile stress in the $+\alpha$, $+\beta$ quadrant. The relation among the r and z axes , ϕ , and the α and β lines is shown in Fig. 28. Then σ_r , σ_z , and τ_{rz} are related to k , p , and ϕ in the following way:

$$\begin{aligned} \sigma_r &= -p + k \sin 2\phi \\ \sigma_z &= -p - k \sin 2\phi \qquad [\text{II-6}] \\ \tau_{rz} &= k \cos 2\phi \end{aligned}$$

Substitution of equations II-6 into the first two terms of equations II-3 and II-4 gives

$$\frac{\partial(-p + k \sin 2\phi)}{\partial r} + \frac{\partial k \cos 2\phi}{\partial z} + \frac{(\sigma_r - \sigma_\theta)}{r} = 0 \qquad [\text{II-7}]$$

$$\frac{\partial(-p - k \sin 2\phi)}{\partial z} + \frac{\partial k \cos 2\phi}{\partial r} + \frac{\tau_{rz}}{r} = 0 \qquad [\text{II-8}]$$

If both σ_θ and k are known functions of r and z, equations II-7 and II-8 can be solved numerically. Both $\sigma_\theta(r,z)$ and $k(r,z)$ depend upon the strains in both the plastic and the elastic portions of the specimen depicted in Fig. 28. In particular, σ_θ will be affected by $\varepsilon_\theta = u_r/r$, where u_r, the radial displacement of a volume element, is equal to the integral of the radial strain over the distance from the z axis (in the elastic region) to the volume element (in the plastic region). And $k(r,z)$, when strain hardening is considered, is a function of the plastic strains (and strain rates) in the plastic enclave; the plastic strains are a function of the boundary displacements at the plastic-elastic boundary; and these displacements are a function of the strains in the elastic core. The calculations of σ_θ and k are both formidable at this time, but for the purposes of argument they will be assumed to be known functions of r and z. If, by coincidence, the assumed values of σ_θ and k were the "correct" ones throughout the entire plastic enclave, the solutions of equations II-7 and II-8 for the stresses σ_r, σ_z, and τ_{rz} would be correct. Otherwise, σ_θ and k could, in principle, still be made sufficiently self-consistent with the remaining stress solution by iteration.

Equations II-7 and II-8 are hyperbolic, under the assumption that σ_θ and k are known functions of r and z. (The equations are still hyperbolic if σ_θ is treated as a function of r, z, σ_r, and σ_z.) The characteristic directions of equations II-7 and II-8 are $dr/dz = \tan\phi$ or $-\cot\phi$, which are just the equations for the α and β lines. These equilibrium equations may be referred to the slip lines by substituting

$$\frac{\partial}{\partial r} = \sin\phi \frac{\partial}{\partial s_\alpha} + \cos\phi \frac{\partial}{\partial s_\beta} \qquad [\text{II}-9]$$

$$\frac{\partial}{\partial z} = \cos\phi \frac{\partial}{\partial s_\alpha} - \sin\phi \frac{\partial}{\partial s_\beta}$$

into equations II-7 and II-8. The symbols $\partial/\partial s_\alpha$ and $\partial/\partial s_\beta$ represent partial differentiation along the α and β lines, respectively. A little further manipulation results in the following equations:

$$-\frac{\partial \rho}{\partial s_\alpha} - 2k\frac{\partial \phi}{\partial s_\alpha} + \frac{\partial k}{\partial s_\beta} + \frac{(\sigma_r - \sigma_\theta)}{r}\sin\phi + \frac{\tau_{rz}}{r}\cos\phi = 0 \qquad [\text{II}-10]$$

$$-\frac{\partial \rho}{\partial s_\beta} + 2k\frac{\partial \phi}{\partial s_\beta} + \frac{\partial k}{\partial s_\alpha} + \frac{(\sigma_r - \sigma_\theta)}{r}\cos\phi - \frac{\tau_{rz}}{r}\sin\phi = 0 \qquad [\text{II}-11]$$

where ϕ is measured in radians.

The first two terms in equations II-10 and II-11 are the only non-zero terms for the case of plane strain and a constant yield stress. The third term is non-zero if the yield stress is not a constant. The last two terms in each equation are present for an axially symmetric stress field. The solution to the present problem will be obtained for the case where equations II-10 and II-11 are simplified by considering a material with a constant yield stress in plane strain:

$$-\frac{\partial \rho}{\partial s_\alpha} - 2k\frac{\partial \phi}{\partial s_\alpha} = 0 \qquad [\text{II}-12]$$

$$-\frac{\partial \rho}{\partial s_\beta} + 2k\frac{\partial \phi}{\partial s_\beta} = 0 \qquad [\text{II}-13]$$

The effects of the additional terms in equations II-10 and II-11 on the slip-line field solution obtained by using equations II-12 and II-13 have been estimated. For this purpose, σ_θ was assumed to be equal to the minimum principal stress in the meridian plane and $\frac{\partial k}{\partial s}$ was assumed to lie in the range $0 \leq \left|\frac{\partial k}{\partial s}\right| \lessapprox 0.5 \frac{k_{LY}}{a}$. The slip-line field geometry was found to be insignificantly affected by either the strain hardening or the axial symmetry terms. Axial symmetry terms cause the 2° by 4° curvilinear quadrangle marked by an "x" in Fig. 29 to flare out an amount of 0.015° in the negative β direction, and the strain hardening term causes a flare of about 0.035°. These corrections are nominally smaller than the accuracy of the drafting machine used in the construction of the original field and their cumulative total along a β line must be less than one half of a degree, which changes the location of the intersection of a β line with the r axis by about 0.003 a. The cumulative effect of the flare of β lines nearer to the notch root should cause the β line intersection with the r axis at $r = 0.73$ a to be in error by about 0.01 a. Equation II-11 was expressed in finite difference form and the change in $(-p)$ was calculated along the β line which bounds the bottom side of the curvilinear quadrangle marked by the "x" in Fig. 29. The axial symmetry terms increased the calculated value of $(-p)$ on the r axis by about 6 percent, while the strain hardening term decreased this value by about 7 percent. Thus, the neglect of the strain hardening terms, which cannot be accurately calculated at this time, may result in compensating errors of the same order of magnitude as those which arise because of the neglect of axial symmetry. For this reason, the solution to the simplified equations in plane strain was obtained and regarded as a reasonable approximation of the stress state in the plastic enclaves of the axially symmetric notched specimens.

For k = constant, equations II-12 and II-13 may be integrated immediately to give:

$$p + 2k\phi = \text{constant along an } \alpha \text{ line} \qquad [\text{II}-14]$$

and

$$p - 2k\phi = \text{constant along a } \beta \text{ line} . \qquad [\text{II}-15]$$

Equations II-14 and II-15 permit the construction of the geometry of the slip-line field, that is, the determination of the directions of the α and β lines, throughout a region in which both the α and β lines intersect a curve along which the boundary conditions (the values of p and ϕ) are known. Consider the curvilinear quadrangle bounded by the α and β lines in Fig. 46a. Let the hydrostatic pressure at point A be p_A . Then the value of the hydrostatic pressure at point D can be determined with the aid of equations II-14 and II-15 by calculation along the path ABD or along the path ACD. The requirement that p_D have the same value from both of these calculations results in the relation

$$\phi_D - \phi_C = \phi_B - \phi_A \qquad [\text{II}-16]$$

Thus, ϕ_D can be calculated when ϕ_A, ϕ_B, and ϕ_C are known. The position of point D is determined graphically by approximating the α line through points C and D with a straight line whose slope is $\frac{1}{2}(\phi_C + \phi_D) = \phi_C + \frac{1}{2}(\phi_B - \phi_A)$, the average of the slopes of

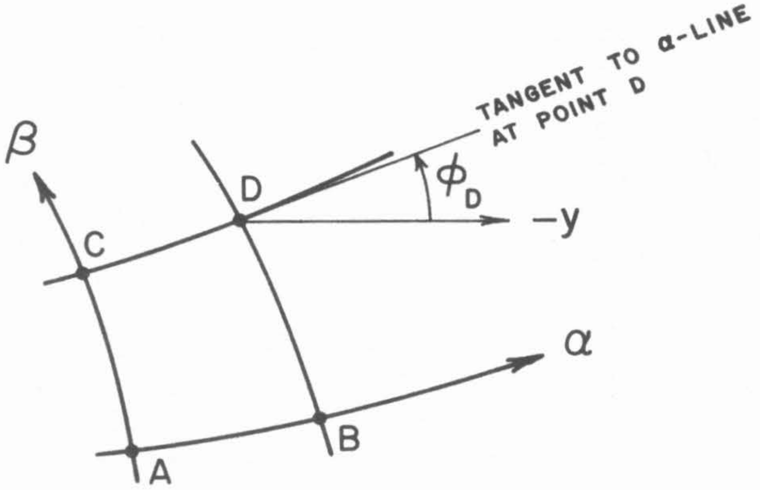

a. Curvilinear quadrangle bounded by slip lines.

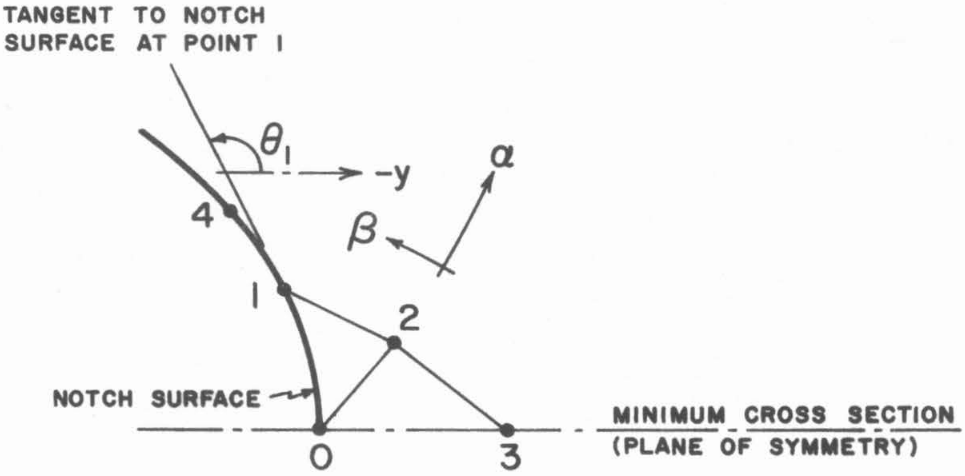

b. Construction to satisfy the boundary conditions.

Fig. 46. Geometry of the slip-line field.

the α line at points C and D, and by approximating the β line through point B with a straight line of slope $\left\{\frac{\pi}{2} + \phi_B + \frac{1}{2}(\phi_C - \phi_A)\right\}$. The intersection of these two straight lines determines point D. The position of point D determined in this way is quite accurate provided $\Delta\phi = \phi_D - \phi_C$ is small, of the order of 5° [Hill (29)].

Graphical construction of the slip-line field is started at the corner of the y axis (or r axis), which lies in a plane of symmetry, and the notch surface, along which p is a constant equal to $-k$ (in the plastically deformed region) and the value of ϕ is known. This region is sketched in Fig. 46 b . If ϕ is measured counter-clockwise from the negative y direction (the choice of the direction for $\phi = 0$ is arbitrary in plane strain since only changes in ϕ appear in the equations), the value of ϕ_0 in Fig. 46 b is $\pi/4$ and the value of ϕ_1 is $\theta - \pi/4$. Since $p_1 = p_0$, and p_2 must have the same value whether calculated along the α line from 0 to 2 or along the β line from 1 to 2, $(\phi_2 - \phi_0)$ must equal $-(\phi_2 - \phi_1)$. Thus, $\phi_2 = \frac{1}{2}(\phi_0 + \phi_1)$. The point 2 is located by the intersection of a line through point 0 with slope $\frac{1}{2}(\phi_0 + \phi_2)$ and a line through point 1 with slope $\frac{1}{2}(\phi_2 + \phi_1) + \pi/2$. Then a straight line through point 2 with slope $\frac{1}{2}(\phi_2 + \phi_3) + \pi/2$, where $\phi_3 = \pi/4$ because of symmetry, locates point 3 on the y axis. This procedure is repeated starting with points 1 and 4 on the notch surface and the β line through point 4 is constructed point-by-point to its intersection with the y axis.

The slip-line field for the hyperbola-shaped notch with an asymptotic half-angle of $14\frac{1}{2}°$ and minimum section half-thickness

$y = a$ (see Fig. 28) has been constructed graphically by the method described above and is shown in Fig. 29. Some of the slip lines used in the construction of the field have been omitted from Fig. 29 for clarity. The actual drafting work was performed at a scale about 2.6 times that of Fig. 28. The maximum value of $\phi_1 - \phi_0$, $\phi_4 - \phi_1$, etc. (see Fig. 46 b) in the full-scale graphical construction was 8° and values as small as 2° were used for the interval between the β lines far from the notch root.

The value of p may now be calculated anywhere in the known slip-line field by the use of equation II-15 (or II-14). If p_y and ϕ_y, and p_B and ϕ_B are the values of p and ϕ on the y axis and the notch boundary, respectively, along a connecting β line, then

$$p_y - p_B = 2k(\phi_y - \phi_B) \qquad [\text{II-17}]$$

Recalling that σ_z is the maximum tensile stress on the y axis and is therefore equal to $-p_y + k$, that $-p_B = k$, and that the yield stress in tension, σ_{yd}, is equal to $2k$, the following expression is obtained for $\sigma_z(y)$:

$$\sigma_z(y) = [1 + (\phi_B - \phi_y)]\,\sigma_{yd} \qquad [\text{II-18}]$$

Values of σ_z / σ_{yd} which have been calculated from equation II-18 are shown along the y axis in Fig. 29. The first two columns of Table 4 show the position y/a (equal to r/a) on the y axis at which a β line from the notch boundary has experienced a slope change $\Delta\phi = \phi_B - \phi_{y/a}$. The points on the y axis corresponding to $\Delta\phi$ = 62°, 65°, 66°, and 67° were calculated by parabolic interpolation from the values of y/a corresponding to $\Delta\phi$ = 60°,

64°, and 68°, i.e.,

$$\frac{y}{a} = \frac{(64-\Delta\phi)(68-\Delta\phi)}{(64-60)(68-60)} \times 0.7325 + \frac{(\Delta\phi-60)(68-\Delta\phi)}{(64-60)(68-64)} \times 0.6374$$

$$+ \frac{(\Delta\phi-60)(\Delta\phi-64)}{(68-60)(68-64)} \times 0.4655 \qquad [II\text{-}19]$$

The third column lists the values of σ_z / σ_{yd} calculated by equation II-18. The maximum value of σ_z / σ_{yd} is limited by the asymptotic angle of the hyperbola to the value $\{1+[(180^\circ-14.5^\circ)-45^\circ] \div 57.3^\circ\} \approx 2.3$. The other columns in Table 4 list quantities calculated in subsequent parts of this stress analysis.

The portion of the tensile load transmitted across the minimum section of an axially symmetric specimen by a plastic enclave that extends from $y=a$ to $y=b$ is given by

$$T_p = \int_b^a \sigma_z \, 2\pi r \, dr$$

$$= \sigma_{yd} \pi a^2 \, 2\int_{b/a}^{1} \left(\frac{\sigma_z}{\sigma_{yd}}\right)\left(\frac{r}{a}\right) d\left(\frac{r}{a}\right) \qquad [II\text{-}20]$$

Values of the integrand in equation II-20 have been calculated at the various points where the β lines of the graphical construction of the slip-line field intersect the y axis. These values of the integrand are listed in the fourth column of Table 4. An approximate value of the integral in equation II-20 was obtained step-wise by expressing $\left(\frac{\sigma_z}{\sigma_{yd}}\right)\left(\frac{r}{a}\right)$ as a quadratic function of $\left(\frac{r}{a}\right)$ over a range of three successive values of $\left(\frac{r}{a}\right)_i$ and integrating over this range. For expedience in the mathematical manipulations, a new variable $s = \left(\frac{r}{a}\right)_1 - \left(\frac{r}{a}\right)$ and $s_i = \left(\frac{r}{a}\right)_1 - \left(\frac{r}{a}\right)_i$ was introduced,

TABLE 4. Numerical Values Involved in the Elastic-Plastic Stress Analysis.

	1	2	3	4	5	6	7	8	9 1st approx.	10 1st approx.	11 2nd approx.	12 2nd approx.
	r/a	$\Delta\phi$	σ_z/σ_{yd}	$(\sigma_z/\sigma_{yd})(r/a) \equiv \sigma^*$	indices, i, for $(r/a)_i$	$(r/a)_1 - (r/a)_i \equiv \rho_i$	$\int_{\rho_1}^{\rho_i} \sigma^* \, d\rho$	$T_p/(\sigma_{yd}\pi a^2)$	$T_e/(\sigma_{yd}\pi a^2)$	σ_{nom}/σ_{yd}	$T_e/(\sigma_{yd}\pi a^2)$	σ_{nom}/σ_{yd}
a	1.0000	0°	1.0000	1.0000	①	0.0000		0.000	0.248	0.248	0.248	0.248
b	0.9896	8°	1.1396	1.1277	②	0.0104	0.0111	0.022	0.340	0.362		
c	0.9775	16°	1.2793	1.2505	① ③	0.0225	0.0255	0.051	0.441	0.492	0.429	0.480
d	0.9622	24°	1.4190	1.3654	②	0.0153	0.0200					
e	0.9407	32°	1.5587	1.4663	① ③	0.0368	0.0506	0.152	0.675	0.827	0.614	0.766
f	0.9201	38°	1.6638	1.5309	②	0.0206						
g	0.8929	44°	1.7672	1.5779	① ③	0.0478	0.0733	0.299	0.846	1.145	0.731	1.030
h	0.8680	48°	1.8382	1.5956	②	0.0249						
i	0.8370	52°	1.9077	1.5967	① ③	0.0559	0.0891	0.477	0.924	1.401	0.771	1.248
j	0.7939	56°	1.9776	1.5700	②	0.0431	0.0683	0.614	0.925	1.539		
k	0.7325	60°	2.0475	1.4998	① ③	0.1045	0.1627	0.802	0.878	1.680	0.712	1.514
l	0.6946*	62°	2.0825	1.4465	②	0.0379	0.0559	0.914	0.832	1.746		
m	0.6374	64°	2.1175	1.3497	① ③	0.0951	0.1359	1.074	0.743	1.817	0.595	1.669
n	0.6016*	65°	2.1349	1.2844	②	0.0358			0.682			
o	0.5610*	66°	2.1522	1.2074	① ③	0.0764	0.0978	1.270	0.609	1.879		
p	0.5157*	67°	2.1696	1.1189	②	0.0453	0.0527	1.375	0.530	1.905		
q	0.4655	68°	2.1870	1.0180	③	0.0955	0.1064	1.483	0.443	1.926	0.352	1.835

---

* These values of r/a have been calculated by parabolic interpolation between points k, m, and q.

where the indices refer to the successive points at which $\left(\frac{\sigma_z}{\sigma_{yd}}\right)\left(\frac{r}{a}\right)$ has been calculated. The groupings of the indices are shown in column 5 in Table 4 and the values of S_i are shown in column 6. Notice that $S_1 = 0$ in each of the groupings. Letting $\sigma^* \equiv \left(\frac{\sigma_z}{\sigma_{yd}}\right)\left(\frac{r}{a}\right)$, σ^* is approximated in the interval S_1 to S_3 by

$$\sigma^* = \frac{(S_2-S)(S_3-S)}{(S_2-S_1)(S_3-S_1)}\sigma_1^* + \frac{(S-S_1)(S_3-S)}{(S_2-S_1)(S_3-S_2)}\sigma_2^* + \frac{(S-S_1)(S-S_2)}{(S_3-S_1)(S_3-S_2)}\sigma_3^*. \qquad [\text{II-21}]$$

The tensile force transmitted by σ^* as given in equation II-21 across the circular ring between S_1 and S_2 is

$$\int_{S_1=0}^{S_2}\sigma^* ds = \frac{S_2}{S_3(S_3-S_2)}\left\{S_2^2\frac{(\sigma_1^*-\sigma_3^*)}{6} - S_2S_3\frac{(2\sigma_1^*+\sigma_2^*)}{3} + S_3^2\frac{(\sigma_1^*+\sigma_2^*)}{2}\right\}, \quad [\text{II-22}]$$

and between S_1 and S_3 is

$$\int_{S_1=0}^{S_3}\sigma^* ds = \frac{S_3}{S_2(S_3-S_2)}\left\{S_3^2\frac{(\sigma_2^*-\sigma_1^*)}{6} + S_3S_2\frac{(2\sigma_1^*+\sigma_3^*)}{3} - S_2^2\frac{(\sigma_1^*+\sigma_3^*)}{2}\right\}. \quad [\text{II-23}]$$

Equation II-23 must be evaluated for each group of three points in order that equation II-20 may be evaluated in the interval $r=a$ to $r=b$, far under the notch surface. The values obtained from equation II-22 may be regarded as an interpolation between the values obtained from the use of equation II-23. All of the values obtained from the use of equation II-23 and a few values obtained from II-22 are listed in column 7 of Table 4. Twice the cumulative values calculated from equation II-23 represent the total tensile load, in units of $\pi a^2 \sigma_{yd}$, supported by the plastic region between $r=a$ and $r=b$. These values are listed in the eighth column.

III. APPROXIMATE STRESS CALCULATIONS IN THE ELASTIC CORE OF THE NOTCHED SPECIMENS

Neuber (28) has obtained solutions for the stress distribution in an axially symmetric elastic solid that contains a deep notch in the shape of a hyperboloid of revolution of one sheet and is loaded in axial tension. His solutions are expressed in terms of an orthogonal curvilinear coordinate system whose coordinates u, v, and w are "natural" to the hyperboloidal notch.

The relations between the Cartesian coordinates x, y, and z of Fig. 28 and the oblate spheroidal coordinates u, v, and w used by Neuber are

$$\begin{aligned} x &= \cosh u \sin v \sin w \\ y &= \cosh u \sin v \cos w \\ z &= \sinh u \cos v \end{aligned} \qquad [\text{III-1}]$$

The relations between the cylindrical coordinates of Figs. 27, 29, and 30 and u, v, and w are

$$\begin{aligned} r &= \cosh u \sin v \\ \theta &= w \\ z &= \sinh u \cos v \end{aligned} \qquad [\text{III-2}]$$

The surfaces u = constant are oblate spheroids, the surfaces v = constant are hyperboloids of revolution of one sheet that asymptotically approach the surfaces of cones whose elements make an angle equal to v (and $\pi - v$) with the z axis, and the surfaces w = constant are meridian planes which contain the z axis.

The stresses derived by Neuber for a deep hyperboloidal notch loaded in axial tension are

$$\sigma_u = \frac{1}{h^2}\left\{ A\tanh^2 u + \frac{B\cos v}{\cosh^2 u} + C\left[-2-\alpha+\frac{1}{\cosh^2 u}\right]\cos v \right\}$$

$$+ \frac{\cos v}{h^4}\left\{ -A + B + C\cos^2 v \right\}$$

$$\sigma_v = \frac{1}{h^2}\left\{ -\frac{A\cos v}{1+\cos v} + (\alpha-1)C\cos v \right\} + \frac{\cos v}{h^4}\left\{ A - B - C\cos^2 v \right\}$$

$$\sigma_w = \frac{1}{h^2}\left\{ A\left(-\tanh^2 u + \frac{\cos v}{1+\cos v}\right) - \frac{B\cos v}{\cosh^2 u} + C\left[\alpha-1-\frac{1}{\cosh^2 u}\right]\cos v \right\}$$

$$\tau_{uv} = \frac{\tanh u \sin v}{h^2}\left\{ \frac{-A}{1+\cos v} + (\alpha-1)C + \frac{1}{h^2}\left[-A+B+C\cos^2 v\right] \right\}$$

$$\tau_{vw} = 0 \quad , \quad \tau_{uw} = 0 \qquad [\text{III}-3]$$

where $\alpha = 2(1-\nu)$, ν = Poisson's ratio

$h^2 = \sinh^2 u + \cos^2 v$

$A = (\alpha-1)(1+\cos v_0)C$

$B = A - C\cos^2 v_0$

$$C = -\frac{\sigma_{nom}(1+\cos v_0)}{2\left[1+(2-\alpha)\cos v_0 + \cos^2 v_0\right]}$$

σ_{nom} = the tensile load divided by πa^2, the area of the minimun section

$v = v_0$ represents the notch surface, so

$\frac{r}{a} = \frac{\sin v}{\sin v_0} \cosh u$ where a is the radius to the notch root.

On the minimum section $(z=0)$: $u=0, \sigma_z = \sigma_u$, $\sigma_r = \sigma_v$, and $\sigma_\theta \equiv \sigma_w$. The expression for the stresses given in equations III-3 become

$$\sigma_z\Big|_{z=0} = \sigma_u\Big|_{u=0} = \frac{1}{\cos v}\left\{B - \alpha C - C\frac{\cos^2 v_0}{\cos^2 v}\right\} = g\left(\frac{r}{a}\right)\sigma_{nom} \qquad [\text{III-4}]$$

$$\sigma_r\Big|_{z=0} = \sigma_v\Big|_{u=0} = \frac{1}{\cos v}\left\{(\alpha-2)C - \frac{A}{1+\cos v} + C\frac{\cos^2 v_0}{\cos^2 v}\right\} = h\left(\frac{r}{a}\right)\sigma_{nom} \qquad [\text{III-5}]$$

$$\sigma_\theta\Big|_{z=0} \equiv \sigma_w\Big|_{u=0} = \frac{1}{\cos v}\left\{(\alpha-2)C - B + \frac{A}{1+\cos v}\right\} \qquad [\text{III-6}]$$

$$\tau_{uv} = 0 \qquad [\text{III-7}]$$

The tensile load, T_e , supported by the elastic core, $b \geq r \geq 0$, , is obtained by integrating the axial stress over ring shaped elements of area, as follows

$$T_e(b) = \int_{r=0}^{r=b} \sigma_z(r)\, 2\pi r\, dr \qquad [\text{III-8}]$$

The expression for σ_z in equation III-4 is given in terms of v , and the integration in equation III-8 is easily performed by changing to the variable v , where $r = a\frac{\sin v}{\sin v_0}$, and $dr = a\frac{\cos v}{\sin v_0}dv$. Then

$$T_e\left(\frac{b}{a}\right) = \frac{2\pi a^2}{\sin^2 v_0}\int_0^{v'}\left(B-\alpha C - C\frac{\cos^2 v_0}{\cos^2 v}\right)\sin v\, dv$$

$$= \frac{2\pi a^2}{\sin^2 v_0}\left\{(A-\alpha C)-(B-\alpha C)\cos v' - C\frac{\cos^2 v_0}{\cos v'}\right\} \qquad [\text{III}-9]$$

where $\sin v' = \frac{b}{a}\sin v_0$.

The tensile load transmitted across the elastic core of the notched specimens according to the first approximation for the stress distribution discussed in Chapter 5 is calculated in the following manner.

Select a value of $r/a = b'/a$ which is given in Table 4. The axial tensile stress in the plastic region at this point is given in column 3 of Table 4 in the form $\sigma_z/\sigma_{yd} = f(\frac{r}{a})$. If this point is on the plastic-elastic boundary, then the axial stress given in equation III-4 is set equal to the value given in column 3 of Table 4.

$$\sigma_z' = g\left(\frac{b'}{a}\right)\sigma_{nom}' = \sigma_z^p = f\left(\frac{b'}{a}\right)\sigma_{yd} \qquad [\text{III}-10]$$

Equation III-10 permits the nominal stress $\sigma_{nom}' = \frac{f(b'/a)}{g(b'/a)}\sigma_{yd}$ to be determined. This value for σ_{nom}' is substituted into equation III-9 and the ratio $T_e(b'/a)/\pi a^2\sigma_{yd}$ is calculated. These values of $T_e(b'/a)/\pi a^2\sigma_{yd}$ are listed in column 9 of Table 4.

The tensile load transmitted across the elastic core between $r=0$ and $r=b$ in Fig. 32 is calculated for the second approximation to the stress distribution in this region as follows.

The radial stress in the plastic region is equal to $\sigma_z^p - \sigma_{yd}$. Thus the value of $\sigma_r^p(r/a)/\sigma_{yd}$ is one less than the value of $\sigma_z^p(r/a)/\sigma_{yd}$ given in column 3 of Table 4 and can be written $\sigma_r^p(r/a)/\sigma_{yd} = f(r/a)-1$.

The requirement of continuity of radial stress at $r=b$ fixes the nominal stress, σ'_{nom} , of Neuber's equations according to the following equation:

$$\sigma_r'(b/a) = h(b/a)\sigma'_{nom} = \sigma_r^p(b/a) = [f(b/a)-1]\sigma_{yd} \qquad [\text{III}-11]$$

The value of σ'_{nom} obtained from equation III-11, $\sigma'_{nom} = \dfrac{[f(b/a)-1]\sigma_{yd}}{h(b/a)}$, is inserted into equation III-9, giving the tensile load, T_e' , supported by this portion of the axial elastic stress, and into equation III-4, giving the value of $\sigma_z'(b/a)$ which is associated with this value of the nominal stress σ'_{nom} .

The axial stress is also assumed to be continuous at $r=b$, so that $\sigma_z''(b/a) = \sigma_z^p(b/a) - \sigma_z'(\frac{b}{a})$ must be contributed by an additional stress distribution whose radial component is $\sigma_r''(b/a) = 0$. This supplemental stress distribution on the elastic core has been assumed to be given by equations III-4, 5, 6, and 7 when the radial scale factor has been changed so that $(\sin v/\sin v_o) = r/b$. The tensile load supported by this supplemental stress distribution is calculated directly from equation III-4 with $\cos v$ set equal to $\cos v_o$. Equation III-4 gives $\sigma_z'' = g(b/b)\sigma''_{nom}$, so

$$T_e''(r=b) = \pi b^2 \sigma''_{nom} = \pi a^2\left(\frac{b^2}{a^2}\sigma''_{nom}\right).$$

The total tensile load supported by the two superimposed stress distributions on the elastic core, $T_e = T_e' + T_e''$, is recorded in column 11 of Table 4 in units of $T_e / \pi a^2 \sigma_{yd}$.

IV. STRESS DISCONTINUITY AT A PLASTIC-ELASTIC INTERFACE

A. Plastic Strain Constant Throughout Plastic Region

The stress state is discontinuous across an interface between an elastic region and a plastic region in which the plastic strain has a finite value adjacent to the interface. The value of the plastic strain will be assumed to be constant throughout the plastic region for the purpose of calculating the magnitude of the stress discontinuity at the interface.

Figure 47 is a schematic representation of the plastic strain state in the vicinity of the plastic-elastic interface. The case of plain strain will be considered wherein the total strain component perpendicular to the u-v plane, ε_w is a constant, not necessarily equal to zero, and the plastic part of this strain component, $\varepsilon_{w(plastic)}$, is equal to zero. The plastic strain, γ, in the plastic region results from slip on planes parallel to $\overline{BC}$ and is equal to $\delta/\overline{AC}$, where δ is is the displacement of point A relative to point C. If this strain were produced by dislocations gliding on slip plane $\overline{BC}$, the dislocations would form a wall along $\overline{AB}$, as shown in Fig. 47. The displacement δ at A results in a dilatational plastic strain component referred to the u axis of the amount

$$\varepsilon^{p}_{u(plastic)} = -\frac{\delta \cos\theta}{L} = -\delta \cos\theta \frac{\sin\theta}{\overline{AC}}$$

$$= -\frac{1}{2}\gamma \sin 2\theta \qquad [IV-1]$$

The total dilatational strain components parallel to the plastic-elastic interface, $\varepsilon_{u(total)}$ and $\varepsilon_{w(total)}$, are continuous across the interface. That is,

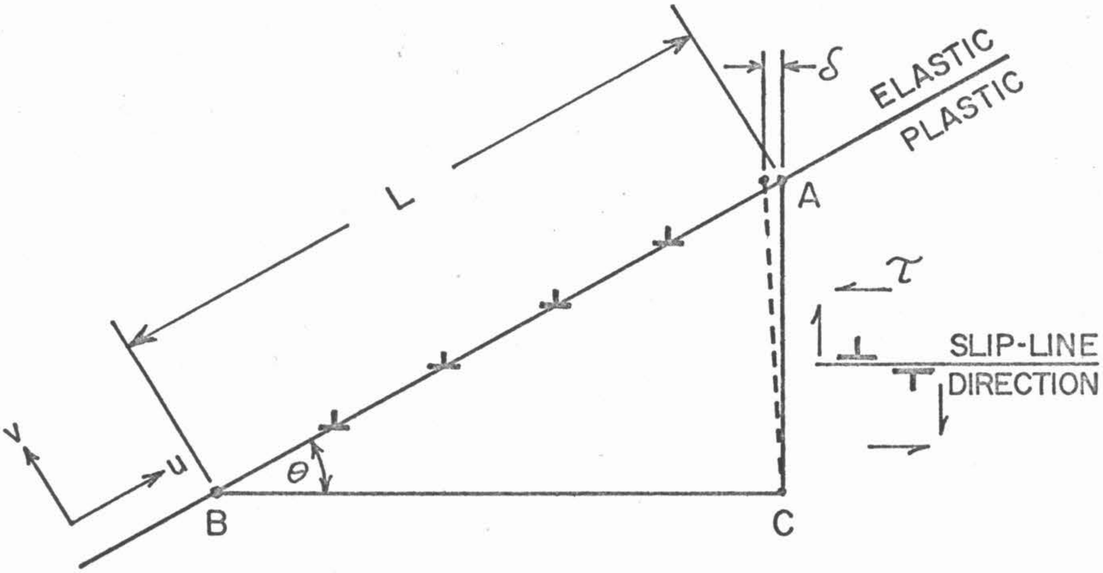

Fig. 47. Geometry of slip lines and plastic strain discontinuity at the plastic-elastic interface.

$$\varepsilon^{e}_{u(\text{total})} = \varepsilon^{p}_{u(\text{total})} = \varepsilon^{p}_{u(\text{elastic})} + \varepsilon^{p}_{u(\text{plastic})} \qquad [\text{IV-2}]$$

and $$\varepsilon^{e}_{w} = \varepsilon^{p}_{w} \qquad [\text{IV-3}]$$

where the superscripts refer to the elastic and the plastic regions. The elastic strain component in the w direction is related to the stresses by Hooke's law,

$$E\,\varepsilon_{w(\text{elastic})} = \sigma_w - \nu(\sigma_u + \sigma_v), \qquad [\text{IV-4}]$$

where E is Young's modulus, and the elastic strain component in the u direction is given by

$$\begin{aligned} E\,\varepsilon_{u(\text{elastic})} &= \sigma_u - \nu(\sigma_v + \sigma_w) \\ &= (1-\nu^2)\sigma_u - \nu(1+\nu)\sigma_v - \nu E\,\varepsilon_{w(\text{elastic})}, \end{aligned} \qquad [\text{IV-5}]$$

where σ_w has been substituted by the value given by equation IV-4.

Now the plastic strain in the plastic region can be related to the stresses through equations IV-2 and 5 giving

$$\begin{aligned} E\,\varepsilon^{p}_{u(\text{plastic})} &= E\,\varepsilon^{e}_{u(\text{elastic})} - E\,\varepsilon^{p}_{u(\text{elastic})} \\ &= (1-\nu^2)(\sigma_u^{e} - \sigma_u^{p}) - \nu(1+\nu)(\sigma_v^{e} - \sigma_v^{p}) - \nu E(\varepsilon^{e}_{w} - \varepsilon^{p}_{w})_{(\text{elastic})} \end{aligned} \qquad [\text{IV-6}]$$

Equilibrium requires that the normal stress component perpendicular to the interface, σ_v, be continuous across the interface. And equation IV-3 requires $(\varepsilon^{e}_{w} - \varepsilon^{p}_{w})_{(\text{elastic})}$ to be equal to zero when there is no plastic contribution to this strain component. The non-zero terms of equation IV-6 may be written as

$$(\sigma_u^{e} - \sigma_u^{p}) = \frac{E\,\varepsilon^{p}_{u(\text{plastic})}}{1-\nu^2} \qquad [\text{IV-7}]$$

or $$(\sigma_u^{e} - \sigma_u^{p}) = -\frac{G\,\gamma\,\sin 2\theta}{1-\nu} \qquad [\text{IV-8}]$$

where the value of $\varepsilon^{p}_{u(\text{plastic})}$ given in equation IV-1 and the relation

$E = 2(1+\nu) G$, G being the shear modulus, have been substituted into equation IV-7.

Equation IV-8 relates the discontinuity in the normal stress component tangent to the plastic-elastic interface, $(\sigma_u^e - \sigma_u^p)$, to the plastic strain referred to the slip-line directions, γ , and the angle, θ, between the interface and a slip line. The sign of equation IV-8 depends on the manner in which the positive value for the shear strain, γ, is defined. The value of γ involved in equation IV-8 is the algebraic sum of the values of γ produced by slip on the two orthogonal slip systems.

B. Thin Boundary Film With Continuously Varying Flow Stress

The stress state in a boundary film, or layer, is considered in which the shear flow stress, k, of the material changes continuously from the value of the maximum shear stress in the elastic region, τ_{max}^e, at the plastic-elastic interface to a value τ_{max}^p at a distance t into the plastic region. The model of this boundary film is shown in Fig. 48. The assumption is made that the stress state in the boundary film is a function only of s, a coordinate perpendicular to the interface.

The field equations which are applicable to the plastic boundary film are equations II-10 and 11 of Appendix II when the terms for axial symmetry are neglected:

$$-\frac{\partial p}{\partial s_\alpha} - 2k\frac{\partial \phi}{\partial s_\alpha} + \frac{\partial k}{\partial s_\beta} = 0 \qquad [IV-9]$$

$$-\frac{\partial p}{\partial s_\beta} + 2k\frac{\partial \phi}{\partial s_\beta} + \frac{\partial k}{\partial s_\alpha} = 0 \qquad [IV-10]$$

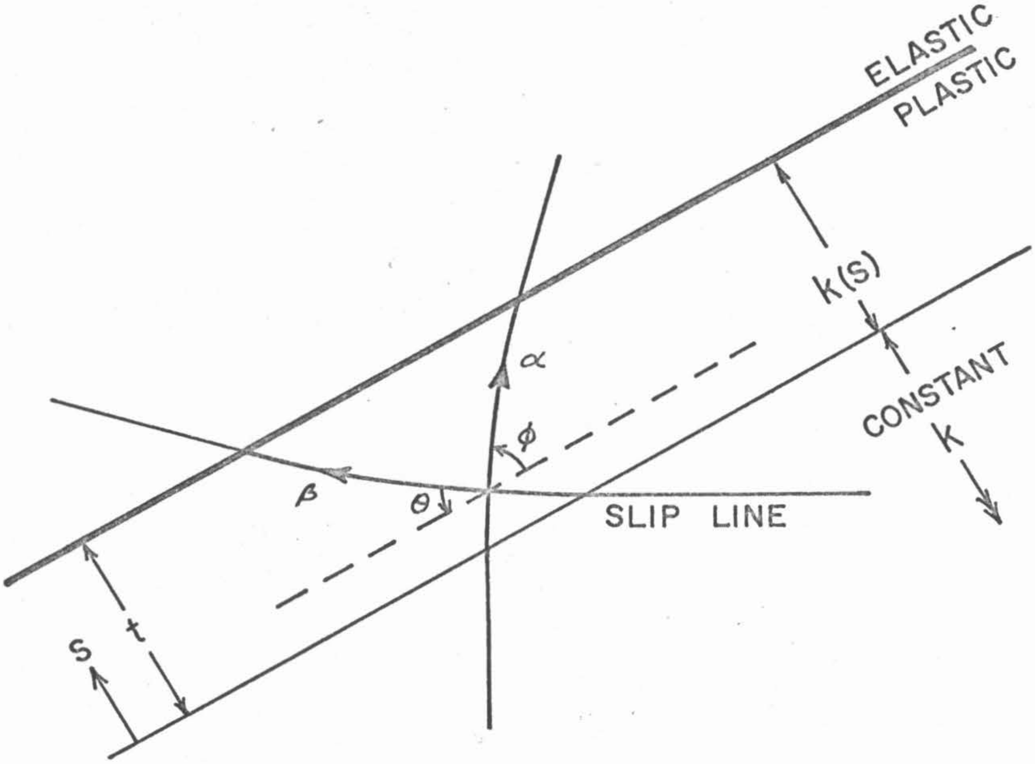

Fig. 48. Geometry of slip-line field in boundary film where k, $k = \tau_{yd}$, varies continuously between the values of τ_{max} in the plastic and the elastic regions.

where ρ, k, and ϕ have the meanings given on p. 166. Note that $\phi = 90^\circ - \theta$. Since ρ, k, and ϕ are assumed to be functions only of s, as defined in Fig. 48, equations IV-9 and 10 can be written in terms of total differentials when the substitutions

$$\frac{\partial}{\partial s_\alpha} = \sin\phi \frac{\partial}{\partial s} \qquad \frac{\partial}{\partial s_\beta} = \cos\phi \frac{\partial}{\partial s} \qquad [IV-11]$$

are made. The resulting equations are

$$-\frac{d\rho}{ds}\sin\phi - 2k\frac{d\phi}{ds}\sin\phi + \frac{dk}{ds}\cos\phi = 0 \qquad [IV-12]$$

$$-\frac{d\rho}{ds}\cos\phi + 2k\frac{d\phi}{ds}\cos\phi + \frac{dk}{ds}\sin\phi = 0 \qquad [IV-13]$$

Solving equations IV-12 and 13 simultaneously to eliminate the terms with $d\rho$ and multiplying through by the differential ds results in

$$k \sin 2\phi \; d2\phi - \cos 2\phi \; dk = 0 \qquad [IV-14]$$

Integration of equation IV-14 gives

$$\int \tan 2\phi \; d2\phi = \int \frac{dk}{k}$$

$$= -\ln|\cos 2\phi| = \ln k + C \qquad [IV-15]$$

A little manipulation of equation IV-15 gives

$$k \cos 2\phi = \text{constant}$$

or

$$\sigma_{yd} \cos 2\theta = \text{constant} \qquad [IV-16]$$

Equation IV-15 relates the direction of the slip-line field to the value of the flow stress in the thin boundary film.

REFERENCES

1. M. E. Shank, "A Critical Survey of Brittle Failure in Carbon Plate Steel Structures other than Ships," Symposium on Effect of Temperature on the Brittle Behavior of Metals with Particular Reference to Low Temperatures, ASTM Special Technical Publication No. 158 (1954), Baltimore, Md., pp. 45-108.

2. M. Gensamer, "Fundamentals of Fractures in Metals," Symposium on Effect of Temperature on the Brittle Behavior of Metals with Particular Reference to Low Temperatures, ASTM Special Technical Publication No. 158 (1954), pp. 164-173.

3. "The Selection of Steel for Notch Toughness," Metals Handbook, 8th Edition, Vol. 1, 'Properties and Selection of Metals,' American Society for Metals, Novelty, Ohio (1961), pp. 225-243.

4. E. M. Lape and J. D. Lubahn, "On the Relations Between Various Laboratory Fracture Tests," Trans. ASME, Vol. 78 (1956), pp. 823-835.

5. T. E. Stanton and R. G. C. Batson, "On the Characteristics of Notched-Bar Impact Tests," Min. of Proc., Inst. of Civil. Eng. (London), Vol. 211 (1921), Part 1 (30 Nov. 1920), pp. 67-100.

6. J. D. Lubahn and S. Yukawa, "Size Effects in Slow Notch-Bend Tests of a Nickel-Molybdenum-Vanadium Steel," ASTM Proc., Vol. 58 (1958), pp. 661-676.

7. C. J. McMahon, Jr., and Morris Cohen, "Initiation of Cleavage in Polycrystalline Iron," Acta Met., Vol. 13 (June 1965), pp. 591-604.

8. A. A. Griffith, "The Phenomena of Rupture and Flow in Solids," Phil. Trans. Roy. Soc. (London), Vol. A221 (1921), pp. 163-198.

9. E. Orowan, "Energy Criteria of Fracture," Weld. J., Research Supplement, Vol. 34, No. 3 (March 1955), pp. 157-s - 160-s.

10. G. Irwin, "Fracture Dynamics," Fracturing of Metals, Am. Soc. Metals, Cleveland, Ohio (1948), reprinted 1952, pp. 147-166.

11. D. K. Felbeck and E. Orowan, "Experiments on Brittle Fracture of Steel Plates," Weld. J., Res. Suppl., Vol. 34, No. 11 (Nov. 1955), pp. 570-s - 575-s.

12. W. S. Pellini, "Evaluation of the Significance of Charpy Tests," Symposium on Effect of Temperature on the Brittle Behavior of Metals with Particular Reference to Low Temperatures, ASTM Special Technical Publication No. 158 (1954), pp. 226.

13. C. Zener, "The Micro-Mechanism of Fracture," Fracturing of Metals, Am. Soc. for Metals, Cleveland, Ohio (1948), reprinted 1952, pp. 3-31.

14. J. R. Low, Jr., "The Relation of Microstructure to Brittle Fracture," Relation of Properties to Microstructure, Am. Soc. for Metals, Cleveland, Ohio (1954), pp. 163-179.

15. G. T. Hahn, B. L. Averbach, W. S. Owen, and Morris Cohen, "Initiation of Cleavage Microcracks in Polycrystalline Iron and Steel," Fracture (Proceedings of an International Conference on the Atomic Mechanisms of Fracture, held in Swampscott, Massachusetts, April 12-16, 1959), John Wiley and Sons, Inc., New York (1959), pp. 91-114.

16. A. H. Cottrell, "Theory of Brittle Fracture in Steel and Similar Metals," Trans. AIME, Vol. 212 (April 1958), pp. 192-203.

17. N. J. Petch, "The Ductile-Cleavage Transition in Alpha-Iron," Fracture (Proceedings of an International Conference on the Atomic Mechanisms of Fracture, held in Swampscott, Mass., April 12-16, 1959), John Wiley and Sons, Inc., New York (1959), pp. 54-64.

18. C. Crussard, R. Borione, J. Plateau, Y. Morillon, and F. Maratray, "A Study of Impact Tests and the Mechanism of Brittle Fracture," Jnl. of Iron and Steel Inst., Vol. 183, (June 1956), pp. 146-177.

19. J. F. Knott and A. H. Cottrell, "Notch Brittleness in Mild Steel," Jnl. of Iron and Steel Inst., Vol. 201 (March 1963), pp. 249-260.

20. A. P. Green and B. B. Hundy, "Initial Plastic Yielding in Notch Bend Tests," J. Mech. Phys. Solids, Vol. 4 (1956), pp. 128-144.

21. B. A. Bilby, A. H. Cottrell, and K. H. Swinden, "The Spread of Plastic Yield from a Notch," Proc. Roy. Soc. (London), Vol. A272 (19 Mar. 1963), pp. 304-314.

22. A. H. Cottrell, "Mechanics of Fracture in Large Structures," Proc. Roy. Soc. London, Vol. A285 (5 April 1965), pp. 10-21.

23. D. P. Clausing, "The Tensile Fracture of Mild Steel," Ph. D. Thesis, Calif. Inst. of Tech., Pasadena, Calif. (1966).

24. N. J. Petch, "The Cleavage Strength of Polycrystals," Jnl. of Iron and Steel Inst., Vol. 174, No. 1 (May 1953), pp. 25-28.

25. A. S. Eldin and S. C. Collins, "Fracture and Yield Stress of 1020 Steel at Low Temperatures," J. Appl. Phys. Vol. 22 (1951), pp. 1296-1297.

26. M. Gensamer, "The Effect of Grain Boundaries on Mechanical Properties," Relation of Properties to Microstructure, Am. Soc. for Metals, Cleveland, Ohio (1954), pp. 16-29.

27. J. A. Hendrickson, D. S. Wood, and D. S. Clark, "The Initiation of Brittle Fracture in Mild Steel," Trans. ASM, Vol. 50 (1958) pp. 656-676.

28. H. Neuber, Theory of Notch Stresses, Principles for Exact Stress Calculations, Translated from the German for the David Taylor Model Basin, U. S. Navy, by F. A. Raven; J. W. Edwards, Ann Arbor, Mich. (1946). (German edition published by J. Springer, Berlin, 1937.) Elastic solution for hyperbolic notch, pp. 84-89 ; plastic deformation at crack tip, pp. 155-164.

29. R. Hill, The Mathematical Theory of Plasticity, Oxford University Press, London (1950), reprinted with corrections, 1956. Slip-line theory, pp. 128-149; stresses at plastic-elastic interface, p. 240; discussion of ref. (31), pp. 245-248.

30. T. R. Wilshaw and P. L. Pratt, "On the Deformation of Charpy Specimens Prior to General Yield," J. Mech. Phys. Solids, Vol. 14 (1966), pp. 7-19.

31. D. N. de G. Allen and R. Southwell, "Relaxation Methods Applied to Engineering Problems. XIV. Plastic Straining in Two-Dimensional Stress-Systems," Phil. Trans. Roy. Soc. (London), Vol. A242 (1949-1950), pp. 379-414.

32. F. W. Barton and W. J. Hall, "A Study of Brittle Fracture Initiation in Mild Steel," Serial No. SSC-147, Technical Report on Project SR-155 to the Ship Structure Committee (U. S. Dept. of Commerce, Office of Technical Services, Washington, D. C.) (July 15, 1963).

33. G. T. Hahn and A. R. Rosenfield, "Experimental Determination of Plastic Constraint Ahead of a Sharp Crack Under Plane-Strain Conditions," Trans. ASM, Vol. 59, No. 4 (Dec. 1966), pp. 909-919.

34. N. Davidenkov, E. Shevandin, and F. Wittmann, "The Influence of Size on the Brittle Strength of Steel," J. Appl. Mech, Vol. 14, No. 1 (March 1947), pp. A-63 - A-67.

35. W. F. Brown, Jr., J. D. Lubahn, and L. J. Ebert, "Effects of Section Size on the Static Notch Bar Tensile Properties of Mild Steel Plate," Weld. J., Res. Suppl., Vol. 26, No. 10 (Oct. 1947), pp. 554-s - 559-s.

36. G. R. Irwin, "The Effect of Size Upon Fracturing," Symposium on Effect of Temperature on the Brittle Behavior of Metals with Particular Reference to Low Temperatures, ASTM Special Technical Publication No. 158 (1954), pp. 176-188.

37. J. C. Fisher and J. H. Hollomon, "A Statistical Theory of Fracture," AIMME, Technical Publication No. 2218, Metals Technology, Vol. 14, No. 5 (Aug. 1947), pp. 1-16.

38. E. R. Parker, "The Effect of Section Size on the Fracture Strength of Mild Steel," Fracturing of Metals, Am. Soc. for Metals, Cleveland, Ohio (1948), reprinted 1952, pp. 82-89.

39. J. L. M. Morrison, "The Yield of Mild Steel with Particular Reference to the Effect of Size of Specimen," Inst. Mech. Engr. (London), Proceedings, Vol. 142 (July-Dec. 1939), pp. 193-223.

40. J. R. Griffiths and A. H. Cottrell, "Elastic Failure at Notches in Silicon-Steel," J. Mech. Phys. Solids, Vol. 13 (1965), pp. 135-140.

41. J. A. Hendrickson, "The Initiation of Yielding and Brittle Fracture in Annealed Mild Steel," Ph. D. Thesis, California Institute of Technology, Pasadena, California (1957), 133 pages.

42. D. S. Clark and D. S. Wood, "The Time Delay for the Initiation of Plastic Deformation at Rapidly Applied Constant Stress," ASTM Proc., Vol. 49 (1949), pp. 717-735.

43. A. R. Rosenfield and G. T. Hahn, "Numerical Descriptions of the Ambient Low-Temperature, and High-Strain Rate Flow and Fracture Behavior of Plain Carbon Steel," Trans. ASM, Vol. 59 (1956), pp. 962-980.

44. F. de Kazinczy, W. A. Backofen, and B. Kapadia, "Discussion" to paper by N. J. Petch given in reference (17); also, author's reply, pp. 65-67.

45. D. S. Wood and D. S. Clark, "Delayed Yielding in Annealed Mild Steel with Special Reference to Yielding at Low Temperatures," Fourth Technical Report under Office of Naval Research Contract N6onr-24418, Project Designation NR 031-285. California Institute of Technology, Pasadena, Calif. (Dec. 1951).

46. Comment by D. S. Wood as discussed by C. S. Barrett in the summary of the session on cleavage fracture, Fracture (Proceedings of an International Conference on the Atomic Mechanisms of Fracture, held in Swampscott, Massachusetts, April 12-16, 1959), John Wiley and Sons, New York (1959), p. 8.

47. R. T. Shield, private communication.

48. P. M. Morse and H. Feshbach, Methods of Theoretical Physics, McGraw-Hill Book Co., Inc., New York (1953) pp. 703-705.

49. W. G. Johnston and J. J. Gilman, "Dislocation Velocities, Dislocation Densities, and Plastic Flow in Lithium Fluoride Crystals," J. Appl. Phys., Vol. 30, No. 2 (Feb. 1959), pp. 129-144.

50. G. T. Hahn, "A Model for Yielding with Special Reference to the Yield-Point Phenomena of Iron and Related B. C. C. Metals," Acta Met., Vol. 8 (Aug. 1962), pp. 727-738.

51. P. J. Worthington, "The Upper Yield Stress of Polycrystalline 3°/o Silicon Iron," Acta Met., Vol. 15 (Dec. 1967), pp. 1795-1798.

52. T. L. Russell, D. S. Wood, and D. S. Clark, "The Influence of Grain Size on the Yield Phenomenon in Steel," Acta Met., Vol. 9 (Dec. 1961), pp. 1054-1063.

53. W. Sylwestrowicz and E. O. Hall, "The Deformation and Aging of Mild Steel," Proc. Phys. Soc. of London, Vol. 64B (1951), pp. 495-502.

54. D. J. Dingley and D. McLean, "Components of the Flow Stress of Iron," Acta Met., Vol. 15 (May 1967), pp. 885-901.

55. J. A. Ewing and W. Rosenhain, "Experiments in Micro Metallurgy - Effects of Strain. Preliminary Notice," Proc. Roy. Soc. London, Vol. 65 (1899), pp. 85-90.

56. G. T. Hahn, "Dislocation Etch-Pitting of Iron and Mild Steel," Trans. AIME, Vol. 224 (April 1962), pp. 395-397.